

SOLUBILITY AND PHASE TRANSITIONS IN BATCH
AND LAMINAR-FLOW TUBULAR CRYSTALLIZERS

A Thesis
Presented to
The Academic Faculty

By

José R. Méndez del Río

In Partial Fulfillment
of the Requirements for the Degree
Master of Science in Chemical Engineering

Georgia Institute of Technology

November, 2004

SOLUBILITY AND PHASE TRANSITIONS IN BATCH
AND LAMINAR-FLOW TUBULAR CRYSTALLIZERS

Approved by:

Dr. Ronald W. Rousseau, Chairman
School of Chemical & Biomolecular Engineering
Georgia Institute of Technology

Dr. William J. Koros
School of Chemical & Biomolecular Engineering
Georgia Institute of Technology

Dr. Angus P. Wilkinson
School of Chemistry & Biochemistry
Georgia Institute of Technology

Dr. David J. am Ende
Pfizer, Inc.

Date Approved: November 2004

A mis padres y abuelos...

ACKNOWLEDGEMENTS

I would like to first acknowledge my advisor, Dr. Ronald W. Rousseau, for his continuous support and feedback throughout the progress of this work. Thanks to our discussions and his criticism this thesis is a better work. Special thanks also go to Dr. David J. am Ende from Pfizer Inc. His work and the work of his group motivated the present research on the laminar flow tubular crystallizer. It was also thanks to him that funding from Pfizer was possible. I am also grateful to the other members of my thesis committee, Dr. William J. Koros and Dr. Angus P. Wilkinson, for their time and interest in this project.

This work could not have been possible without the ideas, motivation and support of the past and present group members of our lab: Karsten Bartling, Young-soo Kim, Jennifer Luk, Izumi Kurosawa, Jennifer Sherard, Daniel Euhus, Stephanie Barthe, Cosmas Bayuadri, Holly Paskow and Moussa Dicko. In some way or another all of these people have helped me succeed in these past two years, whether it was in lab work or in free summer tennis lessons.

I would also like to thank Steven J. Brenek from Pfizer Inc. and James Ward from Lasentec for their ideas and input in this project. Dr. Sankar Nair is also acknowledged for allowing me the use of his powder x-ray diffractometer and his purified water system. Albermale Corp. is acknowledged for providing naproxen sodium. I appreciate the help of the staff of the School of Chemical & Biomolecular Engineering at Georgia Tech, especially Brenda Mattox and Megan Wolfel. Financial support from the GEM Consortium and Pfizer Inc. is greatly appreciated.

There are a certain number of people to which I owe deep gratitude; they made Atlanta a more enjoyable place. Among them are: Luis Aguilar, Carlos Quant, Ernesto Angueira, Mayra Colombani, Charlene Rincón, Eduardo Vázquez, José “Kinsi” Rodríguez, Neil Mukherjee, Donald Taylor III, and Jun Sato. I know that in years to come, every time I remember Atlanta, I will remember all of you guys. My deepest appreciation also goes to Kimberly P. Deckant; without her these past few months would not have been the same.

To my family away from home, my brother Jorge L. Méndez, Jr., my sister-in-law Stephanie Broxton, and my niece Caitlin M. Méndez, thanks for being here for me. You have helped me here from day one.

I would also like to thank the professors and friends at University of Puerto Rico, Mayagüez, who motivated me to attend graduate school. At times it was tougher than I had anticipated, yet I do not regret a moment of it.

And thanks to the people back home whom I care about and love so much. My sister Tamyra and my grandparents, Josefa Avilés, and the late José del Río and Felicita Méndez. Thanks to my uncle Joaquín del Río and my aunt Elbia del Río who have been great sources of knowledge ever since I was a child. And especially to my parents, Myrta del Río and Jorge L. Méndez, I am here thanks to you.

TABLE OF CONTENTS

ACKNOWLEDGEMENTS.....	iv
LIST OF TABLES.....	viii
LIST OF FIGURES.....	ix
NOMENCLATURE.....	xiii
SUMMARY.....	xvii
CHAPTER 1: INTRODUCTION.....	1
CHAPTER 2: BACKGROUND.....	3
2.1 Crystallization.....	3
2.2 Metastable Zone.....	4
2.3 Polymorphism.....	7
2.4 Lasentec® Focused Beam Reflectance Measurement.....	13
2.5 Cooling Crystallizers.....	15
CHAPTER 3: DETERMINATION OF NAPROXEN SODIUM SOLUBILITY AND RELATED PROPERTIES IN WATER USING A LASENTEC FBRM.....	17
3.1 Introduction.....	17
3.1.1 Naproxen Sodium Solubility.....	17
3.1.2 Methodology.....	19
3.2 Experimental.....	23
3.2.1 Equipment.....	23
3.2.2 Procedure.....	24
3.3 Results and Discussion.....	26
3.4 Conclusions.....	35
CHAPTER 4: PROCESS MONITORING AND CHARACTERIZATION OF PARACETAMOL AND D-MANNITOL CRYSTALLIZATIONS: BATCH AND LAMINAR FLOW TUBULAR CRYSTALLIZERS.....	36
4.1 Introduction.....	37
4.1.1 Background.....	37
4.1.2 Laminar Flow Tubular Crystallizer.....	38
4.1.3 Polymorphism.....	43
4.1.4 Materials used.....	44
4.1.4.1 Paracetamol.....	44
4.1.4.2 D-mannitol.....	45
4.1.5 Process monitoring.....	46
4.2 Materials.....	49

4.3	Experimental.....	49
4.3.1	Batch Crystallization.....	49
4.3.1.1	Equipment.....	49
4.3.1.2	Procedure.....	50
4.3.2	Laminar Flow Tubular Crystallizer System.....	51
4.3.2.1	Equipment.....	51
4.3.2.2	Procedure.....	52
4.4	Results and Discussion.....	53
4.4.1	Paracetamol.....	54
4.4.1.1	Batch Crystallization.....	55
4.4.1.2	Laminar Flow Tubular Crystallizer System.....	65
4.4.1.3	Paracetamol Polymorphism.....	69
4.4.2	D-mannitol.....	73
4.4.2.1	Batch Crystallization.....	74
4.4.2.2	Laminar Flow Tubular Crystallizer System.....	80
4.5	Conclusions.....	85
APPENDIX A: EXPERIMENTAL SOLUBILITY DATA FOR NAPROXEN SODIUM IN WATER.....		87
APPENDIX B: OTHER SYSTEMS STUDIED IN BATCH AND LAMINAR FLOW TUBULAR CRYSTALLIZERS.....		88
APPENDIX C: TEMPERATURE AND SUPERSATURATION PROGRESSIONS IN THE LAMINAR FLOW TUBULAR CRYSTALLIZER.....		92
C.1	Introduction.....	92
C.2	Number of Transfer Units (NTU) method for heat and outlet temperature determination.....	93
C.3	NTU method for temperature progression along the inner tube with given inlet and outlet temperatures.....	95
C.4	Finite differences analysis for temperature progression.....	96
C.5	Overall heat transfer coefficient.....	102
C.6	Supersaturation progression in the LFTC.....	103
C.7	Closing remarks.....	106
APPENDIX D: TABULATED DATA AND RESULTS FOR THE CRYSTALLIZATION OF PARACETAMOL AND D-MANNITOL IN BATCH AND LAMINAR FLOW TUBULAR CRYSTALLIZERS.....		107
D.1	Paracetamol data.....	107
D.2	D-mannitol data.....	109
REFERENCES.....		113

LIST OF TABLES

Table 3-1. Coefficients found for naproxen sodium through regression analysis....	33
Table 4-1. Reynolds numbers for the LFTC based on solvents.	53
Table 4-2. Summary of averaged data of nucleation temperature, metastable zone width and relative supersaturation at nucleation for paracetamol, 34.02 g / 100 g ethanol and 55.66 g / 100 g methanol, for the studied batch cooling rates.....	62
Table 4-3. Average time for paracetamol solutions to crystallize and reach equilibrium in the slurry.....	69
Table 4-4. Nucleation rates for batch crystallization of D-mannitol solutions (25.2 g / 100 g water) at different cooling rates.....	76
Table 4-5. Average values of nucleation temperature, metastable zone width and relative supersaturation at nucleation according to cooling rate for the cooling batch crystallization of D-mannitol from aqueous solutions (47.3 g / 100 g water)...	77
Table 4-6. Approximate relative supersaturation at the outlet of the LFTC and nucleation rates in the receiving vessel according to average cooling temperature for D-mannitol solutions (47.3 g / 100 g water).....	83
Table 4-7. Average time for D-mannitol solutions (47.3 g / 100 g water) to crystallize and reach equilibrium in the slurry.....	84
Table C-1. Data and calculated values for heat transfer on the LFTC by NTU method with constant wall temperature.....	95
Table C-2. Equivalent cooling rates for the LFTC on a basis of 0.02 m characteristic lengths.....	102
Table C-3 Overall heat transfer coefficients for the LFTC.....	102
Table C-4. Length to reach supersaturation for D-mannitol solutions in the LFTC..	105

LIST OF FIGURES

Figure 2-1. Solubility and metastable limit diagram.....	5
Figure 2-2. Constant supersaturation profile on batch crystallization.....	5
Figure 2-3. Solubility diagram for monotropic polymorphism.....	10
Figure 2-4. Solubility diagram for enantiotropic polymorphism.....	10
Figure 2-5. (a) Schematic of FBRM probe and (b) possible chord lengths of a particle.....	14
Figure 3-1. FBRM data and temperature progression for the naproxen sodium / water system in a batch experiment.....	21
Figure 3-2. Determination of saturation temperature through y-intercept of linear section from data of temperature of disappearance vs. heating rate.....	22
Figure 3-3. Naproxen sodium solubility.....	27
Figure 3-4. Solubility and metastable zone limits for dihydrate naproxen sodium...	27
Figure 3-5. Metastable zone widths for dihydrate naproxen sodium according to cooling rate and saturation temperature.....	28
Figure 3-6. Relative supersaturation necessary to induce nucleation for solutions of naproxen sodium in water in cooling batch crystallization.....	28
Figure 3-7. Van't Hoff plot for naproxen sodium solubility data.....	29
Figure 3-8. PXRD patterns for ANS, MNS and DNS by Kim and for the experiment performed at a concentration of 333.7 g ANS / kg solution ($T_{\text{sat}} = 36.9^{\circ}\text{C}$).....	30
Figure 3-9. Solubility data for the naproxen sodium species and their curves as derived from multiple regression analysis.....	33
Figure 3-10. Solubility and metastable zones of naproxen sodium.....	34
Figure 4-1. Velocity profiles for different flowrates in the LFTC.....	40
Figure 4-2. Residence time distribution for different flowrates through the LFTC...	42

Figure 4-3. Cumulative residence time distribution for different flowrates through the LFTC.....	42
Figure 4-4. Zeroth moment analysis for determination of nucleation rate.....	48
Figure 4-5. Laminar Flow Tubular Crystallizer System.....	52
Figure 4-6. Solubility data for paracetamol in ethanol and methanol.....	54
Figure 4-7. Paracetamol crystals obtained from batch crystallization of paracetamol from an ethanol solution cooled at 0.15 °C/min.....	55
Figure 4-8. Median (no weight) values (at equilibrium) for the CLD of paracetamol crystallized from ethanol and methanol solutions.....	56
Figure 4-9. Mean (no weight) values (at equilibrium) for the CLD of paracetamol crystallized from ethanol and methanol solutions.....	57
Figure 4-10. Chord length distributions at equilibrium for paracetamol crystallized from ethanol solutions at different batch cooling rates.....	57
Figure 4-11. Nucleation rates determined by zeroth moment analysis for paracetamol crystallized from ethanol and methanol solutions.....	58
Figure 4-12. Average nucleation temperatures for paracetamol crystallized from ethanol and methanol solutions.....	60
Figure 4-13. Solubility and metastable limits at different cooling rates for paracetamol crystallized from ethanol and methanol solutions.....	61
Figure 4-14. Relative supersaturation at nucleation for the crystallization of paracetamol from ethanol and methanol solutions.....	62
Figure 4-15. Relative supersaturation as a function of time and cooling rate for paracetamol in ethanol and methanol solutions.....	63
Figure 4-16. Relative supersaturation as a function of time and cooling rate for paracetamol in ethanol and methanol solutions starting at the same supersaturation..	64
Figure 4-17. Chord length distributions at equilibrium for paracetamol crystallized from ethanol solutions at different batch cooling rates and through the LFTC.....	66
Figure 4-18. Chord length distributions at equilibrium for paracetamol crystallized from methanol solutions at different batch cooling rates and through the LFTC.....	67
Figure 4-19. Comparison of nucleation rates for batch and LFTC system with	

paracetamol in ethanol and methanol solutions.....	68
Figure 4-20. Paracetamol crystals obtained from a methanol solution through the LFTC at a 30.4 mL/min flow rate with 11.5 °C cooling temperature.....	70
Figure 4-21. PXRD pattern of paracetamol crystallized from a methanol solution via LFTC at 30.4 mL/min and a cooling temperature of 11.5 °C.....	70
Figure 4-22. Paracetamol crystals obtained from a methanol solution through the LFTC at a 30.4 mL/min flow rate with a cooling temperature of 3 °C, before reaching equilibrium.....	72
Figure 4-23. Paracetamol crystals obtained from a methanol solution through the LFTC at a 30.4 mL/min flow rate with a cooling temperature of 3 °C, 15 minutes after reaching equilibrium.....	72
Figure 4-24. Solubility data for D-mannitol in water.....	74
Figure 4-25. D-mannitol crystals obtained from aqueous solution (47.3 g / 100 g water) through batch cooling crystallization at 0.20 °C/min.....	75
Figure 4-26. Average nucleation temperatures for D-mannitol crystallized from aqueous solutions (47.3 g / 100 g water) in batch operation.....	77
Figure 4-27. Relative supersaturation at nucleation for the crystallization of D-mannitol from aqueous solutions (47.3 g / 100 g water).....	78
Figure 4-28. Relative supersaturation as a function of time and cooling rate for D-mannitol aqueous solutions (47.3 g / 100 g water).....	79
Figure 4-29. Nucleation rates determined by zeroth moment analysis for D-mannitol crystallized from aqueous solutions (47.3 g / 100 g water).....	80
Figure 4-30. Nucleation rates as determined by zeroth moment analysis for crystallization of D-mannitol from aqueous solutions (47.3 g / 100 g water) at different temperatures on the LFTC.....	83
Figure 4-31. PXRD pattern of D-mannitol crystallized from an aqueous solution via LFTC.....	84
Figure C-1. Temperature progression of the solution along the length of the LFTC assuming constant wall temperature for different temperature setpoints.....	96
Figure C-2. Temperature progression for solution and cooling fluid in counterflow using finite differences method for 10 °C temperature setpoint.....	100

Figure C-3. Temperature progression for solution and cooling fluid in counterflow using finite differences method for 20 °C temperature setpoint.....	100
Figure C-4. Temperature progression for solution and cooling fluid in counterflow using finite differences method for 30 °C temperature setpoint.....	101
Figure C-5. Temperature progression for solution and cooling fluid in counterflow using finite differences method for 40°C temperature setpoint.....	101
Figure C-6. Relative supersaturation progression for D-mannitol solution in the LFTC for 10°C setpoint.....	103
Figure C-7. Relative supersaturation progression for D-mannitol solution in the LFTC for 20°C setpoint.....	104
Figure C-8. Relative supersaturation progression for D-mannitol solution in the LFTC for 30°C setpoint.....	104
Figure C-9. Relative supersaturation progression for D-mannitol solution in the LFTC for 40°C setpoint.....	105

NOMENCLATURE

A_i	Inner cross-sectional area
A_o	Outer cross-sectional area
A_s	Surface area
ΔA_j	Incremental area
ANS	Anhydrous naproxen sodium
b	Effective width of area scanned by the laser beam
$c(l)$	Chord-count density function
C_i	Solute concentration
C_i^*	Concentration at equilibrium
C_p	Heat capacity
$\Delta C(l)$	Number of chord counts
ΔC_p	Change in heat capacity
CLD	Chord Length Distribution
CSTR	Continuous stirred tank reactor
D	Diameter
D_e	Equivalent diameter
DNS	Dihydrate naproxen sodium
$E(t)$	Age function of residence time distribution
f	Fanning friction factor
$F(t)$	Cumulative residence time distribution
FBRM	Focused Beam Reflectance Measurement

FDA	United States Food and Drug Administration
h	Heat transfer coefficient
h_i	Heat transfer coefficient for fluid inside
h_o	Heat transfer coefficient for fluid outside
ΔH_{soln}	Enthalpy of solution
J_0	Nucleation rate
k	Conductivity
$L, l, \Delta l$	Length
LFTC	Laminar Flow Tubular Crystallizer
\dot{m}	Mass flow rate
\bar{m}_0	Zeroth moment
MNS	Monohydrate naproxen sodium
MSMPR	Mixed suspension, mixed product removal crystallizer
N_{total}	Number of particles per unit volume
NTU	Number of Transfer Units
NTU_x	Local number of transfer units
Nu_D	Diameter-based Nusselt number
PAT	Process Analytical Technologies
Pe	Péclet number
Pr	Prandtl number
PSD	Particle Size Distribution
PXRD	Powder X-ray Diffraction
q	Heat

Δq_j	Incremental heat
r	Radius
R	Radius of the tube
R	Ideal gas constant
r_h	Hydraulic radius
Re	Reynolds number
Re _D	Diameter-based Reynolds number
RTD	Residence time distribution
S	Supersaturation
$t, \Delta t$	Time
t_m	Mean residence time
T	Temperature
T_{bulk}	Bulk temperature
T_{in}, T_i	Inlet temperature
T_m	Melting temperature
T_{out}, T_o	Outlet temperature
U_i	Overall heat transfer coefficient for fluid inside
\dot{v}_S	FBRM scan speed
v_z	Velocity
\bar{v}_z	Average velocity
$v_{z,max}$	Maximum velocity
\bar{V}_S	Effective volume scanned by the FBRM

x	mole fraction
z	Length
ε	Efficiency
λ	Depth that the FBRM laser beam penetrates
μ	Viscosity
ρ	Density
σ	Relative supersaturation

SUMMARY

The research addressed in this thesis focuses on monitoring and characterization of pharmaceutical compounds by laser backscattering. In particular, this study covers two topics: (1) the determination of naproxen sodium solubility in water, and its phase transition; and (2) comparisons of batch and laminar flow tubular crystallizers for the production of paracetamol (acetaminophen) and D-mannitol.

Using a Lasentec® Focused Beam Reflectance Measurement (FBRM) device, the solubility of naproxen sodium in aqueous solutions was determined over a temperature range from 15.2 to 39.7 °C. With the determination of the solubilities of two pseudopolymorphs, anhydrous and dihydrated naproxen sodium, the phase transition point between these two forms of the pharmaceutical compound was determined to occur at 30.3 °C. Enthalpy of solution and metastable zone widths were also determined for the experimental conditions.

Crystallizations of paracetamol and D-mannitol were performed in a batch crystallizer and in a laminar flow tubular crystallizer (LFTC) system. In the latter system, supersaturation was generated rapidly in the solution being transported through a temperature-controlled tube and recovered in a batch vessel where product crystals were grown to equilibration. Because of the rapid rate at which supersaturation was generated in the LFTC, the resulting crystals were of smaller mean size than those obtained from batch crystallizations. The total time required for crystallization was significantly less with the LFTC than with the batch unit. Additionally, the rapid cooling in the LFTC led to the formation of two different polymorphs of paracetamol, Forms I and II.

CHAPTER 1

INTRODUCTION

The advent of novel technologies has facilitated online process monitoring in many areas of chemical process engineering. One of these technologies, the Lasentec® Focused Beam Reflectance Measurement (FBRM) device, utilizes laser backscattering to monitor chord length distributions of particles in fluid systems. This instrument allows *in situ* monitoring of characteristics of crystal or particle size, without sampling, in an immediate and reliable fashion. Such advantages prove useful in the field of crystallization where the understanding of process dynamics is essential. Two separate projects are described in this thesis. In both of them the FBRM was an indispensable tool.

Motivated by the work of Kim^{1, 2} on the crystallization and characterization of naproxen sodium, the current work presents the solubility diagram of this material in aqueous solutions for a temperature range of 15.2 to 39.7 °C. The use of the FBRM did not only help in accomplishing this, but also in detecting the transition temperature between the dihydrate and the anhydrous form of this material.

Also, a laminar-flow tubular crystallizer (LFTC) is presented as an alternative to common batch crystallizers. Work by Brenek et al.³ with a similar crystallizer served as a motivation for this study. In their work, the researchers found that crystals of a specific, but unidentified, pharmaceutical compound obtained from such a system differed substantially in size and morphology from those obtained from batch crystallization.

In the present project, the FBRM was used to analyze the product crystals from the LFTC. It was found that this system is capable of producing crystals of smaller mean size than in typical batch processes, and under the right conditions, the run times are significantly reduced. It was also found that the LFTC simultaneously produced varying amounts of Forms I and II of paracetamol. The FBRM also proved useful in the estimation of nucleation rates for the studied systems.

The outline of this thesis is as follows: Chapter 2 provides essential background related to the projects. Topics such as crystallization, metastable zones, polymorphism, FBRM, and cooling crystallizer design are discussed. Chapters 3 and 4 provide the key aspects of the research conducted in this study; specifically, Chapter 3 is *Determination of Naproxen Sodium Solubility and Related Properties in Water using a Lasentec FBRM*, and Chapter 4 is *Process Monitoring and Characterization of Paracetamol and D-mannitol Crystallizations: Batch and Laminar-Flow Tubular Crystallizers*. Experimental data and supporting information are provided in four appendixes.

CHAPTER 2

BACKGROUND

Background information about crystallization, metastable zones and polymorphism considered relevant for this project are discussed in this chapter. A brief introduction to the Lasentec® FBRM equipment, use throughout this research, is included. A section concerning cooling crystallizers is also presented.

2.1 Crystallization

Crystallization processes are common in a wide variety of industries. These industries rely on crystallization for the production, separation and/or purification of chemicals. The driving force behind this process is the supersaturation, S , which relates the solute concentration of the system, C_i , to the concentration at equilibrium, C_i^* ,

$$S = \frac{C_i}{C_i^*} \quad (2.1)$$

Sometimes this driving force is expressed in terms of relative supersaturation σ , or

$$\sigma = \frac{C_i - C_i^*}{C_i^*} = S - 1 \quad (2.2)$$

Following or accompanying supersaturation is the nucleation and growth of crystals. Nucleation phenomena can occur from a clear solution (primary nucleation), or be induced by the presence of other crystals (secondary nucleation). Furthermore, primary nucleation can be classified as homogeneous (occurring spontaneously), or as heterogeneous, where nucleation is induced by foreign particles.⁴ The interesting subjects of supersaturation, nucleation and growth have been discussed in much detail in

textbooks, such as those by Nývlt, et al.⁵ and Kashchiev⁶, practically devoted in their entirety to these phenomena.

Although different types of crystallization mechanisms exist, such as cooling and evaporation, and crystallization from melts, vapors or solutions, the following discussion will focus mainly on cooling crystallization from solutions, as it is directly applicable to this research.

2.2 Metastable Zone

Attaining supersaturation in a system would lead to its metastability, and not necessarily to the immediate nucleation of crystals. Figure 2-1 shows a schematic of solubility and metastable zone. In cooling crystallization, when a homogeneous solution in point *a* passes the solubility curve to point *b*, it is considered to be supersaturated and within the metastable zone. If the solution is kept at this temperature, eventually, nucleation and growth will occur. The closer the solution is to the metastable limit, the faster crystallization takes place. Now, if upon very fast cooling, the solution at point *a* is taken to point *c*, past its metastable limit, an uncontrolled crystallization would occur, promoting the formation of fines.⁷ In many cases fines are undesired in the final product,^{8, 9} as they might present filtration problems,⁸ and affect dissolution and encapsulation properties in the case of pharmaceuticals. Usually a constant supersaturation that would allow a narrower size distribution is desired (Fig. 2-2); often helped by seeding.⁷

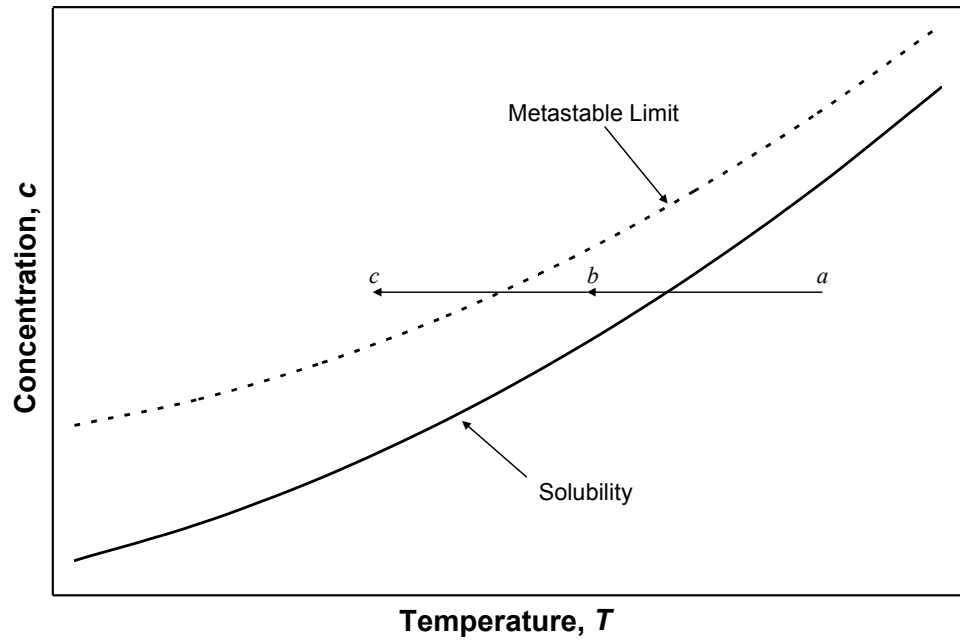


Figure 2-1. Solubility and metastable limit diagram. At a the solute is fully dissolved in solution; at b the solution is supersaturated; at c the solution has overcome its metastable limit.

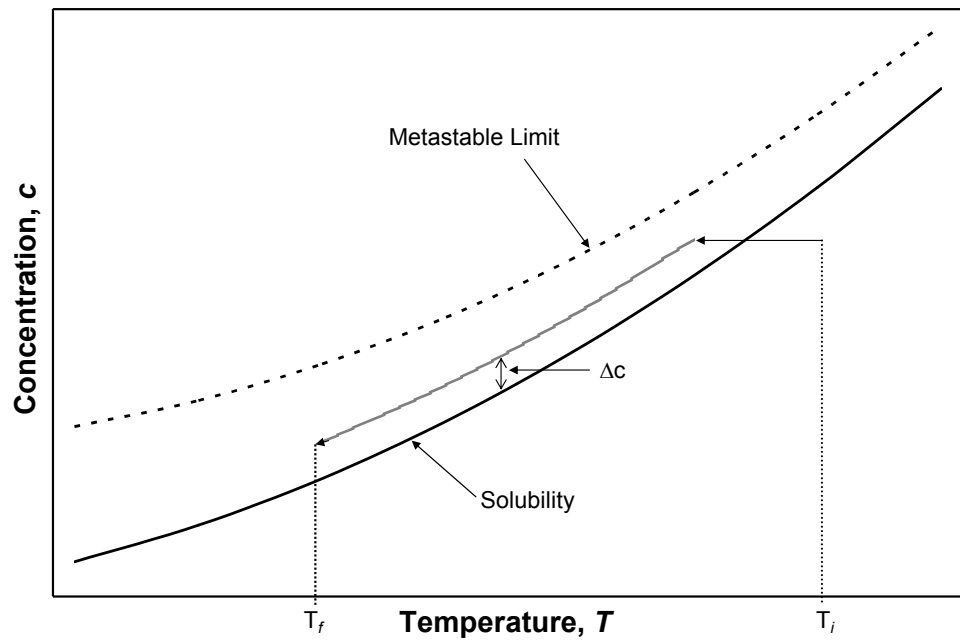


Figure 2-2. Constant supersaturation profile on batch crystallization. Adapted from Davey & Garside.⁷

Metastable limits can be found experimentally by identifying the temperature at which nucleation starts for a solution of known concentration cooled at a constant rate. Nývlt et al.⁵ also describe an isothermal method for measuring metastable zone width based on induction period. The width of the metastable zone, or the maximum allowable undercooling, would be the difference between the saturation and nucleation temperatures. The saturation temperatures forming the solubility curve for the system can be determined by analytic or synthetic methods.¹⁰ Examples of these methods can be found in the literature.^{4, 5, 10} The use of on-line measurement tools has benefited the process of determining both the metastable zone width and solubility by providing reliable and easy-to-use methods for these purposes.¹¹⁻¹⁴

It is important to notice, as it will be shown in chapter 3 and 4, that generally the metastable zone is widened with increasing cooling rates and lowering concentrations. Many researchers have shown experimental data proving this behavior. In general, the critical supersaturation ratio is proportional to the exponential of $T^{-3/2}$. Which means that with increasing temperatures, the critical supersaturation required for nucleation is reduced, henceforth reducing the metastable limit. A well developed model of this is found in Kashchiev's monograph.⁶

The rate at which supersaturation is generated also affects the width of the metastable zone; henceforth the cooling rate affects the metastable limit. In general, the cooling rate is proportional to the metastable zone width to the power of the nucleation order. It follows then that for a constant nucleation order, the increasing cooling rates will render greater metastable zone widths. A summary of relations regarding the

dependence of the metastable zone width on cooling rates can be found in Nývlt et al.⁵ along with other elements that also affect the metastable limit.

2.3 Polymorphism

Many chemical compounds exhibit polymorphism; their molecules are able to exist in different lattice arrangements. A polymorph of a particular compound would have different characteristics than another polymorph. This affects properties such as solubility and morphology, and in the case of pharmaceuticals it would affect compression and filtration properties, dissolution rate and bioavailability. A similar phenomenon that could also affect these properties is pseudopolymorphism. In this case, crystals of the same chemical composition incorporate solvent molecules within their lattice sites with a defined stoichiometry.¹⁵ These crystals are known as solvates, and when the solvent is water they are known as hydrates. McCrone¹⁶ also mentions other examples of pseudopolymorphism; yet the utilization of the term for these cases has fallen into disuse.¹⁷

Morris¹⁸ points out the differences and similarities between polymorphs and hydrates, with a more detailed approach in characterizing the structural aspects of hydrates. He adjudges the differences between polymorphs and hydrates on the basis of crystal structure; a hydrate's structure is a function of the water vapor pressure above the solid, while for a polymorph its structure is only affected by changes in water vapor pressure if water sorption allows molecular motion, which would permit a solution mediated transformation.

In polymorphism (and pseudopolymorphism) we can identify metastable and stable forms, also known as kinetically stable and thermodynamically stable modifications, respectively. For a given temperature range, the stable form will be the one with lower solubility. Metastable forms are not necessarily restricted to one; in fact there could be multiple metastable forms of a crystal molecule, with varying metastability according to the temperature range. As we will see, a stable form can be metastable at a different section of its phase diagram.

Polymorphic systems can be considered monotropic or enantiotropic. In a monotropic system (Fig. 2-3) the stable polymorph will retain its lower solubility throughout the phase diagram when compared to the metastable form. Monotropic transformations of polymorphs are considered irreversible.⁴ Enantiotropic systems (Fig. 2-4) though, exhibit transition points at which the considered metastable form at lower temperatures would become stable at higher temperatures, rendering the previous stable form into a metastable one. Because of the presence of a transition temperature between forms, enantiotropic transformations are considered reversible.⁴ Caution is advised were in doubt of the behavior of the system under study. While one would believe that a system exhibits monotropic behavior, it could in fact be an enantiotropic system at a different temperature range.

Morris¹⁸ indicates that it is often desired to use the thermodynamically stable form for formulation development of pharmaceutical drugs, mainly due to the lower risk of phase transition. In some instances though, a metastable form is desired due to performance or regulatory issues, or in cases in which the stable form is not obtained directly. Guillory¹⁹ states that the metastable form may be preferred when absorption of

the drug is dependent of the dissolution rate, and that it is often this form the one used in capsules or tablets. On the other hand, since the stable form is less prone to transformation, it may be the only form considered for suspensions.

Researchers have developed different techniques in order to produce a desired polymorph. In some cases fast cooling will produce the kinetically stable polymorph, while slow cooling would produce the thermodynamically stable one; this follows the discussion of metastable zones, at slower cooling rates, the metastable limit will be closer to the solubility of the system, particularly to the most stable one. In other cases, like with glycine²⁰, sulfamerazine²¹, and D-mannitol²², crystallization with different solvents enables the formation of different forms. Seeding a supersaturated solution with the desired form is also a normal practice.²³ In certain cases inhibiting agents are added to solutions to avoid the growth of an undesired form.²⁴ It has been reported for the case of glycine that polarized light affects the formation of polymorphs.²⁵ Novel crystallizer design is also an alternative to control polymorphism.^{3,26,27}

It is important, especially for pharmaceuticals, to consider carefully the choice of polymorph for the final product. A metastable form can be acquired and retained in dosage form, yet it could “relax” to a more stable phase, altering its properties. Furthermore, the transformation from metastable to a more thermodynamically stable form can occur in any downstream process, such as aqueous granulation, milling, film coating or tablet compression.¹⁸ Brittain and Fiese²⁸ also mention that the substantial amount of energy used in milling processes can also incur in the transformation of the compound to an amorphous form, which is also highly undesirable.

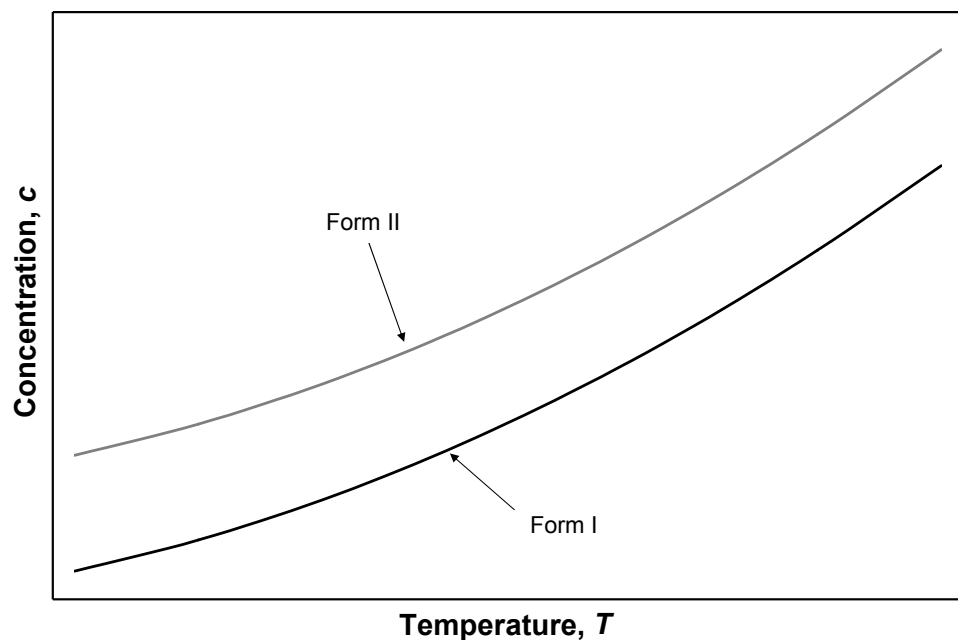


Figure 2-3. Solubility diagram for monotropic polymorphism. Form I is considered the thermodynamically stable polymorph, while Form II is the kinetically stable (metastable) polymorph.

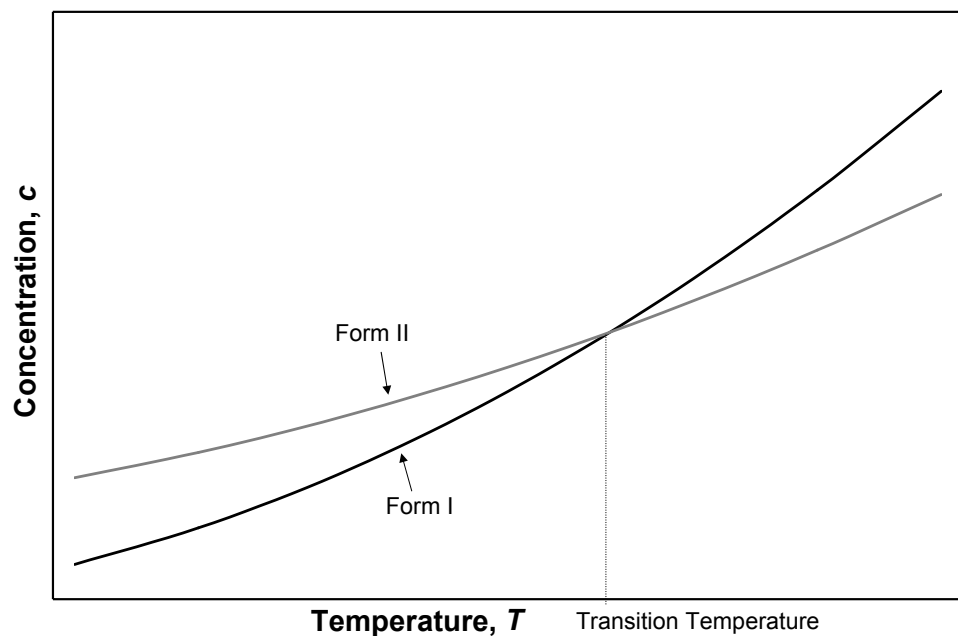


Figure 2-4. Solubility diagram for enantiotropic polymorphism. Form I is the stable form below the transition temperature, while Form II is the metastable one. Above the transition point, Form I becomes metastable, while Form II becomes stable.

From this discussion it is obvious that knowledge of the polymorphic forms and properties of the material under production is highly advisable for those who manufacture the product. Chemburkar et al.²⁹ narrate the story of ritonavir, a protease inhibitor developed by Abbott Laboratories, whose thermodynamically stable polymorph was not readily discovered. Two years after production of the drug started, some lots failed dissolution specifications. A less soluble, more stable polymorph was discovered in these lots. Shortly after, many lots in different lines were experiencing the same problems. Abbott was put into “a market crisis”, with rapidly depleting supplies. The whole production process had to be redesigned to acquire the original, kinetically stable form.

Glaxo experienced its share of polymorphism issues with its drug Zantac (ranitidine hydrochloride).^{30, 31} Two years after the original form was patented, a new more stable one was found, which later became the active ingredient in Zantac. When the patent for the first form expired, generic companies wanted to produce it. But the question was raised, whether the generic companies were able to produce it without concomitantly producing the second form. This and other cases that underwent litigation due to polymorphism and patent protection are summarized elsewhere.³¹

Due to cases like these is probably why Bernstein³² indicates that “most examples of polymorphism are still discovered through serendipity”. Or also the reason why many authors^{17, 30, 32, 33} quote McCrone’s¹⁶ statement that in his opinion “every compound has different polymorphic forms and that, in general, the number of forms known for a given compound is proportional to the time and money spent in research on that compound”.

The current level of computer simulations cannot predict accurately the right polymorphs that are going to form for a particular material, henceforth, to selectively produce a specific polymorph is not a straightforward task.³⁴

The Ostwald rule of stages³⁵ is often mentioned to explain the polymorphism phenomena in crystallization. It is used to show how a crystallized compound can change from a metastable form to a more stable one, especially through solvent mediated transformation. In this process, metastable crystals redissolve into solution while then more stable crystals nucleate. In essence, the system crystallizes losing the minimum amount of free energy possible, from one phase to the next. Nonetheless, the rule has numerous exceptions.

The most appropriate way to explain polymorphism behavior in crystallization processes is to carefully analyze phase diagrams with metastable limits data. Enantiotropic systems also show a better variety of instructional possibilities according to the supersaturation / crystallization path chosen. For this, the reader is directed to the article by Threlfall³³ where the crystallization of polymorphs with enantiotropic diagrams is discussed in much detail. In this article, Threlfall tries to dismiss oversimplifications or misjudgments often committed while analyzing the crystallization of polymorphs.

In general, it is a good advice to know firsthand how far apart are the polymorphic forms in the phase diagram if one wishes to crystallize the metastable form.⁹ Furthermore, the crystallization techniques get to be more “complicated” if not only a specific polymorph is desired, but also a particular crystal size distribution.¹⁵ For this

reason the control of polymorphism and crystal size can be considered paradigms of crystallization.

2.4 Lasentec® Focused Beam Reflectance Measurement

On-line techniques have been used in the laboratories for years to facilitate the analysis of experiments. These process analytical technologies (PAT's) have also penetrated industry. In some, like in pharmaceuticals where there is a strict regulatory environment, these tools have slowly moved into the manufacturing sector. Recognizing this, the U.S. Food and Drug Administration (FDA) announced in August 2002 a revision of the current Good Manufacturing Practices (cGMP's).³⁶ In 2003, the FDA published its *Guidance for Industry: PAT – A Framework for Innovative Pharmaceutical Manufacturing and Quality Assurance*,³⁷ as a first step in improving the incursion of PAT's in these areas.

One example of a PAT is the Lasentec® Focused Beam Reflectance Measurement (FBRM®) instrument, which was used extensively during the present work. The FBRM provides the on-line and *in-situ* ability of measuring the chord length distribution (CLD) of a particulate system through laser backscattering. A highly focused laser beam in the probe (Fig. 2-5a), rotating at a fixed velocity, scans the particles in a small region in front of the probe's sapphire window. When the beam hits a particle, the optical sensors in the probe pick up the backscattering, and the data is analyzed by the system. The chord length (Fig. 2-5b), or the distance between two edges in a particle, is then calculated as the product of the beam speed and the time of the corresponding backscattering signal. The thousands of chord lengths per second that can be acquired by the instrument are

organized in channels and expressed as distributions. The statistical data can be observed on-line and/or saved for later analysis. A more detailed description of the FBRM can be found elsewhere.^{38, 39}

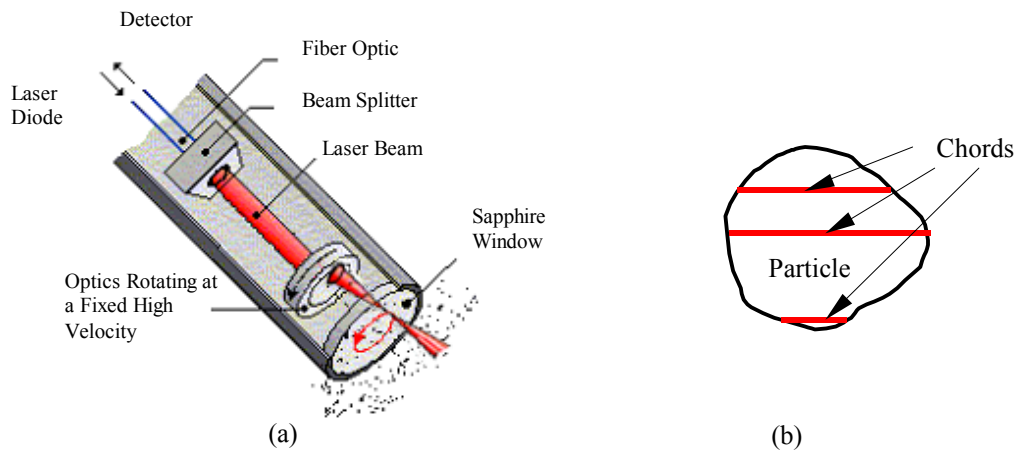


Figure 2-5. (a) Schematic of FBRM probe and (b) possible chord lengths of a particle.

It is important to notice that by no means CLD is the same as particle size distribution (PSD). Taking into account the statistical meaning of CLD researchers have developed models⁴⁰⁻⁴³ to convert and relate CLD's to PSD's.

The importance of acquiring a desired PSD relies on different factors, like product dissolution rate or packaging reasons. In the case of pharmaceuticals a narrow PSD is desired usually to allow a more uniform dissolution rate of the drug. When a smaller mean size is desired, downstream processes, such as milling, are used to reduce it. This not only adds to the inconvenience of time and money spent on the process, but also on further complications like the phase conversion of the solid material in some cases.

2.5 Cooling Crystallizers

Although a simple search in crystallization textbooks shows a great variety of cooling crystallizers, such as agitated tank, cooling disc, rotary, scraped-surface,⁴ twin, Wulff-Bock, Swenson-Walker,^{4, 10} Oslo,^{4, 10, 44} direct contact,^{4, 44} and spray crystallizers⁴⁴ among others, much of the attention is focused on batch and mixed suspension, mixed product removal (MSMPR) crystallizers.

Batch crystallizers are widely used in industry. These crystallizers are flexible, simple, require less capital investment and generally less process development than continuous units.^{7, 45} Their versatility allows them to be used as reactors, crystallizers, mixers and blenders; thus the emphasis in design tends more on the mode of operation.⁷ Their relative simplicity allows for non-stringent qualification of personnel.¹⁰ The use of batch crystallizers in the crystallization field is not limited to cooling crystallization, but they are also used in evaporative, drowning out and reaction crystallization. Supersaturation control is essential to the operation of batch crystallizers. This control depends on the operating policy based on batch time, rate at which supersaturation is generated, possible addition of seed crystals, and agitation.⁷ Because batch crystallizers do not operate under steady state conditions, the modeling of crystal size distribution is more complex than that of continuous crystallizers, due to its dependency on both crystal size and time.⁴⁶ The developed models based on population balances can be found elsewhere,^{5, 45-47} and is mainly attributed to the work of Randolph and Larson⁴⁶. Semi-batch crystallizers are probably not as often mentioned in literature as batch crystallizers, but like batch crystallizers, they also offer a relative operational simplicity. A discussion of semi-batch crystallizers can be found in Tavare's monograph⁴⁵.

MSMPR crystallizers are often discussed in terms of their simplicity of modeling, rather than operation. MSMPR's are the crystallizer equivalent of continuous stirred tank reactors (CSTR's). The analysis for particle population assumes among other things that the crystallizer operates continuously and under steady state conditions.⁷ Detailed analysis for crystal size distribution modeling can be found in the literature.^{5, 45-47}

Another type of crystallizer that is not as often described in literature is the tubular crystallizer. Crystal size distribution analyses capitalize on plug-flow conditions for narrow distributions. Population balance models can be found in the literature.^{46, 48} Examples of tubular crystallizers can be found in the sugar industry⁴⁸ where tower crystallizers are used. But a general search on tubular crystallizers would point to foreign publications⁴⁹⁻⁵⁴ for more fundamental knowledge about their operation as well as foreign patents⁵⁵⁻⁵⁹ that propose different applications. Most of these foreign works are not readily available to the scientific community.

A laminar-flow tubular crystallizer with countercurrent cooling fluid was used in the present work. Its design is based on that of Brenek et al.³ Fundamental knowledge was pursued by comparison of its operation to a batch crystallizer. Heat transfer analysis of the tubular crystallizer was also performed.

CHAPTER 3

DETERMINATION OF NAPROXEN SODIUM SOLUBILITY AND RELATED PROPERTIES IN WATER USING A LASENTEC FBRM

Using a Lasentec FBRM, the solubility of naproxen sodium in water was determined over a temperature range from 15.2 to 39.7 °C. Van't Hoff plots of the data showed a transition temperature between the enantiotropic pseudopolymorphs at 29.8 °C. A multiple regression analysis of the same data estimated the transition point to be 30.3 °C. Powder X-ray diffraction showed that the anhydrous form of naproxen sodium is stable above the transition point, while below it, the dihydrate is the stable form. Enthalpy of solution as a linear function of temperature was estimated from the multiple regression analysis for both forms. Metastable zone widths and relative supersaturation at nucleation were determined for four different cooling rates (0.15, 0.20, 0.30 and 0.40 °C/min).

3.1 Introduction

3.1.1 Naproxen Sodium Solubility

Naproxen sodium is a non-steroidal anti-inflammatory agent commonly found as the active ingredient in over-the-counter drugs. Although many characterization studies have been published, for example in drug absorption⁶⁰⁻⁶² and crystal structure^{1, 63, 64}, the only solubility data located in the literature and showing the effect of temperature is that of di Martino et al.⁶⁵ Di Martino et al. correctly assert that naproxen sodium exists

enantiotropically with its solvates; that is, the solubility curve of one form intersects at a transition point with the solubility curve of another form.

Nevertheless, the work of di Martino et al.⁶⁵ show some inconsistencies that need to be noted. The data and their interpretation describe anhydrous naproxen sodium (ANS) as the thermodynamically stable pseudopolymorph at temperatures below 10.69°C, meaning that below this point the hydrates would have a higher solubility than the anhydrate form. Nonetheless, when describing the materials used, the manuscript states that the dihydrate crystals were obtained by cooling an aqueous solution to 4°C, which is well below their claimed transition point.

The experimental procedure presented by di Martino et al.⁶⁵ is sound. They measured the solubility of dihydrate naproxen sodium in water through an isothermal method with solute concentration determined by UV spectrophotometry. The estimation of the anhydrate solubility was performed by intrinsic dissolution studies, as described by Khankari and Grant⁶⁶, but the data show extremely low solubility values, in addition to other inconsistencies in the text.*

* Tabulated values show the slope of cumulative drug release vs. time with $\mu\text{g}/\text{min}$ units, when in reality it should be $\mu\text{g}/\text{min}\cdot\text{mL}$. From the slope values, the intrinsic dissolution rates are then calculated. The dimension error is still carried, and the slope is divided by the surface area for this purpose. The reported intrinsic dissolution rates hence are shown with $\text{mol}/\text{min}/\text{mm}^2$ units, while the values represent $\text{mol}/\text{min}\cdot\text{mL}\cdot\text{mm}^2$. The surface area used for these calculations was 132.73 mm^2 . This value is that of the tablets' surface area, according to the authors. They also explain that only one face of the tablets was exposed to the dissolution medium. If the tablets were disk shaped, then the surface area used for the calculations must have been half of the value used. It is unclear if the authors refer to the 132.73 mm^2 as the surface area of *one* face of the tablet. This would only affect the value of the intrinsic dissolution rates. Since the surface area is the same regardless of the tablets, the step for calculating the solubility of the anhydrate would cancel the value anyway. Although these inconsistencies have been found, these should not affect the final outcome of solubility determination.

It is believed that the most probable reason for the low solubility values reported, as well as the behavior shown for the rotating disk experiment for the dissolution studies was due to errors in determination through UV spectrophotometry. The results of their dissolution study affect directly their conclusion of a transition point at 10.69°C; this because their results show a closer dissolution rate between the anhydrate and dihydrate at lower temperatures.

An unpublished study by Kim⁶⁷ utilized a synthetic polythermal method^{4, 10} based on visual inspection and HPLC concentration measurements to determine the solubility of naproxen sodium in water over a temperature range from 9.1 to 27.2°C. For this temperature range, dihydrate naproxen sodium (DNS) was found to be the thermodynamically stable pseudopolymorph; contradicting the results of di Martino, et al.⁶⁵ Although Kim was unable to determine the transition temperature between thermodynamically stable pseudopolymorphs, he concluded that it should be located above 27.2°C, the highest solubility limit in his study.

The work of di Martino et al.⁶⁵ show data points for the solubility of naproxen sodium at 21 °C, 26 °C, 31 °C and 37 °C. Should the transition point be somewhere among their studied range, the authors most probably would have missed it, because of their small number of data points.

3.1.2 Methodology

Barrett, et al.^{13, 14} presented a method in which a Lasentec Focused Beam Reflectance Measurement (FBRM) probe was used to determine the solubility and metastable zone widths of potash alum crystals in aqueous solutions. (Principles of the FBRM were discussed in section 2.4). A clear advantage of the method is that it provides reliable and reproducible measurements of the instants of nucleation and dissolution. Visual inspection of crystal formation and disappearance by dissolution, while widely used, does not have the same precision. The FBRM method also facilitates estimation of the saturation conditions in a solution without using invasive sampling procedures to measure concentration. This aspect also facilitates automation of the process.

The following discussion illustrates how the procedure works by describing a run from the present work. Figure 3-1 shows the progression of a single run. After the clear solution has been kept at a temperature above saturation for a predetermined time, the temperature is lowered at a constant rate to induce nucleation, an event resulting in the formation of numerous small crystals. The crystals formed are observed by the FBRM probe and their chord lengths are measured and counted. Chord lengths from 1 to 20 μm were defined to indicate the nucleation event. Assuming that the formation of the observed crystals did not significantly alter the solution concentration, the relative supersaturation at the point of nucleation can be estimated from the solubility and measured temperatures. This information provides an estimate of the metastable limit at the specific cooling rate and conditions. Fujiwara et al. have shown the accuracy of the FBRM method for determination of the metastable limit by comparing it to visual and ATR-FTIR methods for aqueous solutions of paracetamol, reporting only small differences between methods.¹¹

After observing nucleation the solution is heated at a constant rate, and as shown in Figure 3-1, the conditions at which crystals disappear can also be determined. In the present work, coarse counts (50 – 250 μm) were used to indicate the disappearance of crystals. Smaller crystals, having a greater surface area to volume ratio, will dissolve faster than bigger ones. Hence their disappearance into solution would not be a good indicator of full dissolution. Coarse counts, also represent most of the crystal mass in the system.

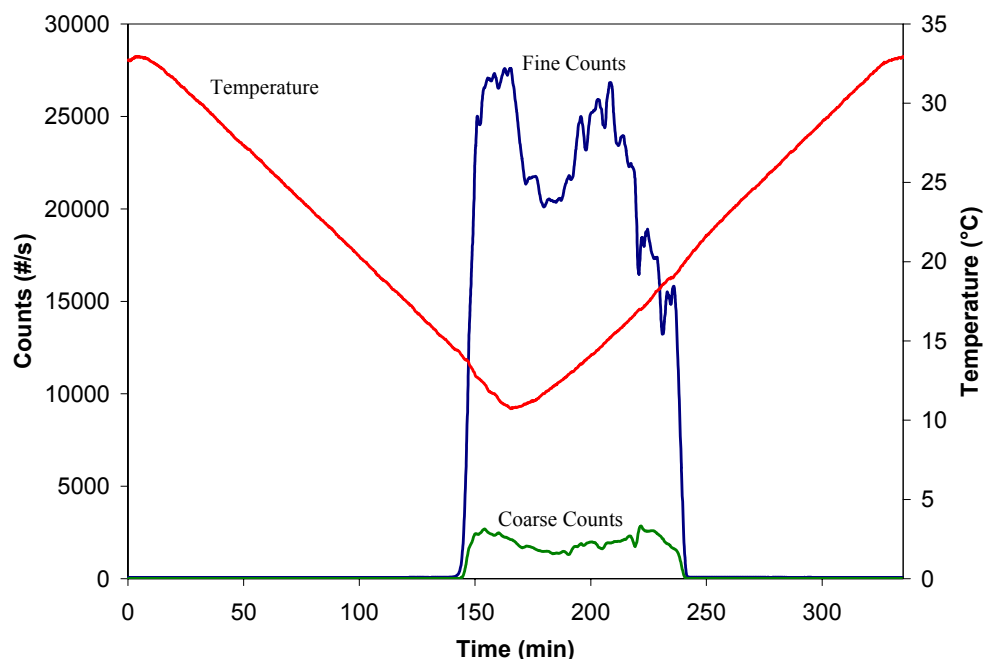


Figure 3-1. FBRM data and temperature progression for the naproxen sodium / water system in a batch experiment. Cooling and heating rates for this specific run were set at $0.15^{\circ}\text{C}/\text{min}$. Concentration of the solution was $145.5 \text{ g ANS} / \text{kg solution}$. The fine counts corresponding to chord lengths from 1 to $20 \mu\text{m}$ were used to determine the point at which nucleation occurred. The coarse counts corresponding to chord lengths between 50 and $250 \mu\text{m}$ were used to determine dissolution of most of the crystal mass. The behavior shown is typical of runs at other concentrations and cooling/heating rates.

Barrett, et al.^{13, 14} showed a non-linear behavior for a solution of potash alum when temperature of disappearance data was plotted against increasing heating rates. As the heating rate increased, the dissolution of crystals separated further from the solubility. For low heating rates (below $0.3^{\circ}\text{C}/\text{min}$) the data conformed to a linear behavior with a positive slope. As shown in Figure 3.2, similar behavior was observed in the present work. If an infinitesimal heating rate could be applied to the system, the instant of full crystal dissolution would occur at the exact saturation point of the system. This infinitesimal heating rate would allow for thermodynamic equilibrium, as the system experiences very slow changes in time, rather than a kinetically driven approach, where the system is “forced” to dissolve. Based on this, when a linear regression is obtained for

these low heating rates, the saturation point can be estimated by the y-intercept of the trendline. Following this method Barrett et al.^{13, 14} found their determined solubility for potash alum to be in very close agreement with previously published data.⁶⁸ A comparison of the original data with the non-linear regression correlation shown by Barrett et al. shows for given saturation temperatures, differences in concentration ranging from 7 to 19%.

Making use of an FBRM D600 probe, the present work focused on the determination of the solubility of naproxen sodium in water over a wider temperature range than had been studied by others.^{65, 67}

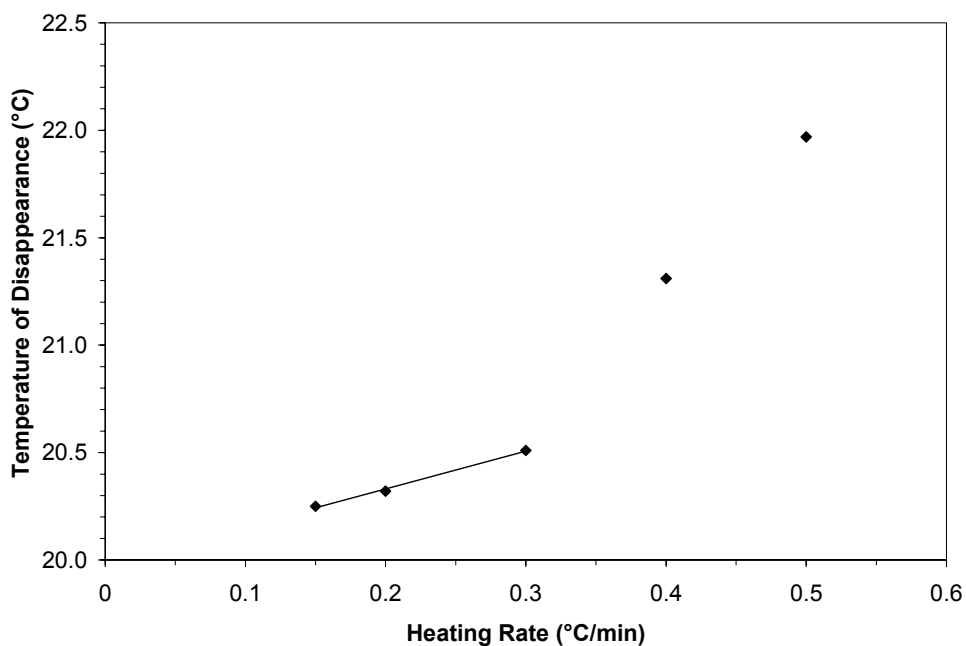


Figure 3-2. Determination of saturation temperature through y-intercept of linear section from data of temperature of disappearance vs. heating rate. The data shown is for a concentration of 145.5 g ANS / kg of solution.

3.2 Experimental

3.2.1 Equipment

A jacketed 500-mL glass vessel (9.68 cm ID) with curved bottom was used to carry out the crystallization of naproxen sodium. A four-port head allowed insertion of a stirrer, FBRM probe, thermocouple and condenser. The solution was stirred by a four-blade 5.1 cm diameter stainless steel propeller with 35° pitch rectangular blades that pumped the contents upward for better contact with the FBRM probe. Stirrer speed was maintained at 400 rpm; this provided good mixing with Reynolds numbers ranging from 11,600 to over 26,000, while avoiding excessive splashing. Three 0.635 cm diameter stainless steel baffles were also used to promote mixing and minimize vortex formation. An FBRM D600 was used to observe nucleation and dissolution of crystals. The scanning rate was set to 2 m/s, with 10-second measurement duration and a moving average set to 10 measurements. The probe also served as a baffle. A condenser with a cooling fluid at about 10°C was attached to the vessel to return any solvent that evaporated. A thermocouple was submerged in the solution to record temperature, which was acquired through an Omega OMB-DAQ-56 connected to a computer. The desired cooling and heating rates were programmed on a VWR 1157P circulator, which provided the temperature control to the vessel. The upper part of the vessel, between the jacketed area and the condenser, was wrapped with a heating cloth maintained at about 50°C (higher than the highest solution temperature) to avoid condensation of the solvent against the walls and top of the vessel. The equipment was maintained inside a dark fume hood with tinted windows to minimize the possibility of photodegradation of naproxen^{69, 70}.

3.2.2 Procedure

Anhydrous naproxen sodium, provided by Albermale Corp., was used without further processing or purification. Water (HPLC grade, purchased from Fisher Scientific) was used as the solvent. To start a set of trials, enough material was included in the vessel so that the FBRM probe tip was submerged in the solution. The first campaign run was based on data from Kim⁶⁷ for saturation conditions at 27.2°C; i.e. at a concentration of 240.24 g ANS / kg solution. Each subsequent run was performed after water had been added to dilute the solution. This was repeated until the solution level reached the top of the jacketed area in the vessel. Following this, the vessel contents were discarded and a new campaign was begun at higher saturation temperatures. Subsequent trial solutions were also diluted, and after the solution reached the top of the jacketed area, some of it was removed through a lower valve in the vessel. The mass of solution removed was measured so that with the known concentration, the mass of both solute and solvent remaining in the vessel was calculated. More dilutions were then performed for the following runs.

Before any campaign started, the solution was heated until full dissolution was achieved. It was then cooled to initiate crystallization, and subsequently warmed to about 12 to 15°C above its saturation temperature. At this temperature the campaign would begin. Every subsequent run would maintain this high temperature for 15 minutes, cool at a specific rate to 1 to 3°C below the point of nucleation and immediately heat at the same rate to the high temperature, where another run would start at a different cooling rate after the 15-minute period at a constant high temperature. At least three different cooling/heating rates (0.15, 0.20 and 0.30 °C/min) were used for each concentration and

each of them was repeated three times. These rates were alternated between runs with no specific pattern.

Barrett and Glennon¹⁴ kept their system at the high temperature for 1.5 hours between cycles, following a protocol for potash alum developed by other researchers. This was done to ensure full dissolution of the solute. Since the FBRM clearly showed full dissolution of the naproxen sodium while temperature was being increased, time between runs at a constant high temperature was limited to 15 minutes.

It has been known that the thermal history of the solution might affect the width of the metastable zone.^{4,5} For example Nývlt et al. show the effect of solution history on the metastable zone width of aqueous KH_2PO_4 solutions.⁵ On the other hand, Barrett and Glennon¹⁴ mention that solution history does not affect the point of nucleation of aqueous potash alum solutions, as proven by experimental results. Solution history effects were not studied on this work, henceforth we can only say that the metastable width data provided is true for the studied conditions, as with most other published metastable data for any system. The reader is reminded also that besides thermal history of the solution, other factors can affect nucleation, such as purity, mechanical action, and dissolved admixtures among others. For a detailed discussion of all these effects the reader is pointed to the monograph by Nývlt et al.⁵ Since the coarse crystals in the solution are in equilibrium with the liquid, their disappearance into solution due to the heating process is independent of the crystallization conditions; hence the thermal history of the solution will not affect at all the determination of solubility through this method.

3.3 Results and Discussion

The solubility of naproxen sodium in water was determined for a range of temperatures from 15.2 °C to 39.7 °C using the procedure described in the previous section. The results are plotted in Figure 3-3. The data compare favorably to those of Kim⁶⁷ for dihydrate naproxen sodium over the range from 15.2 °C to 28.3 °C. Over this common temperature range the differences between solubilities at specific temperatures range between 3 to 10%. The complete data are given in tabular form in Appendix A. The standard errors of the determined saturation temperatures show the high precision of the experimental method, ranging from ± 0.11 to ± 0.33 °C.[†]

Figure 3-4 shows the solubility curve for DNS along with metastable limit curves for different cooling rates. It can be seen, as explained in Chapter 2, that the metastable zone is widened at higher cooling rates. Figure 3-5 shows the metastable zone widths as a function of saturation temperature, reflecting the tendency of the metastable zone to widen with lower temperatures. For example, the difference between the metastable zone width of 0.15 and 0.40 °C/min at a saturation temperature of 27.9 °C is 0.7 °C, while at a saturation temperature of 17.3 °C it is 2.4 °C. Similarly Figure 3-6 shows how a higher relative supersaturation is required to induce nucleation at lower concentrations. In essence, is “easier” to crystallize a material at a higher concentration than at a lower one. For faster cooling rates, and lower concentrations, the relative supersaturation at nucleation of dihydrate naproxen sodium can easily exceed a value of 1.

[†] Standard errors were calculated for the y-intercepts (estimated saturation temperatures) based on the line formed by three data points (experiments) per heating rate, namely 0.15, 0.20 and 0.30 °C/min.

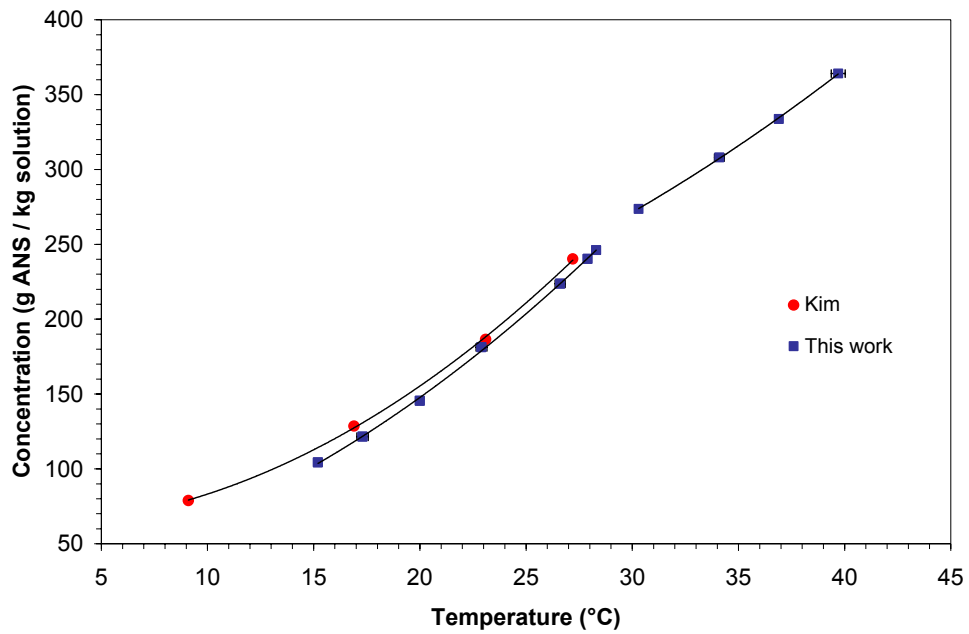


Figure 3-3. Naproxen sodium solubility.

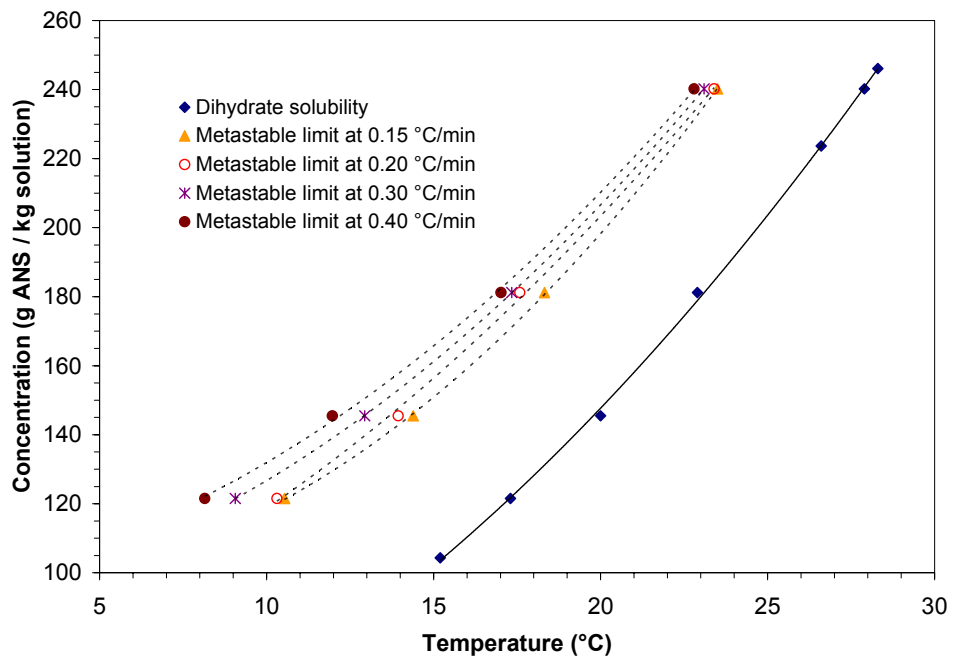


Figure 3-4. Solubility and metastable zone limits for dihydrate naproxen sodium.

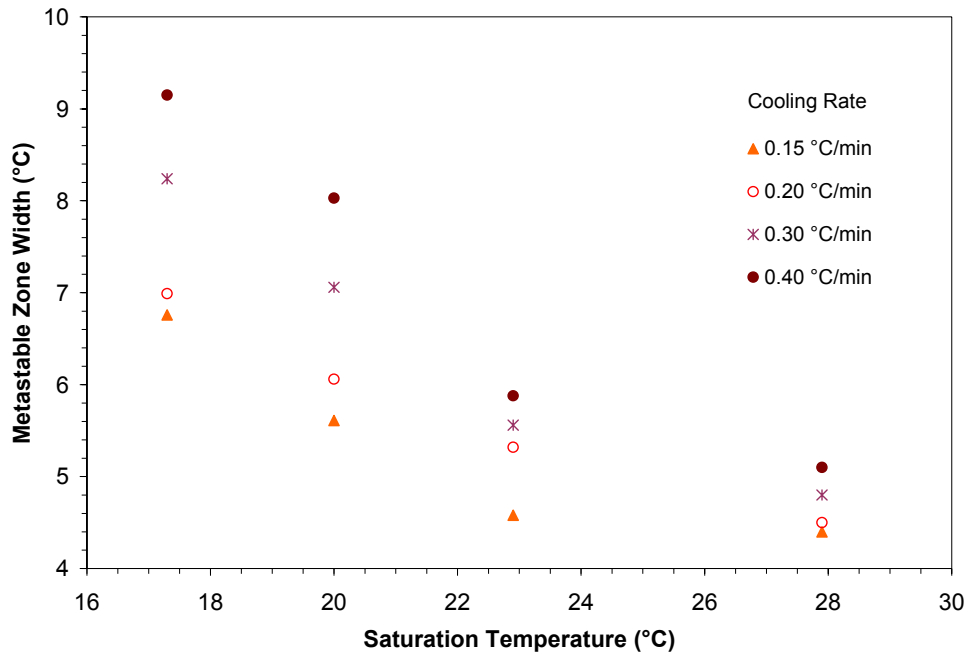


Figure 3-5. Metastable zone widths for dihydrate naproxen sodium according to cooling rate and saturation temperature.

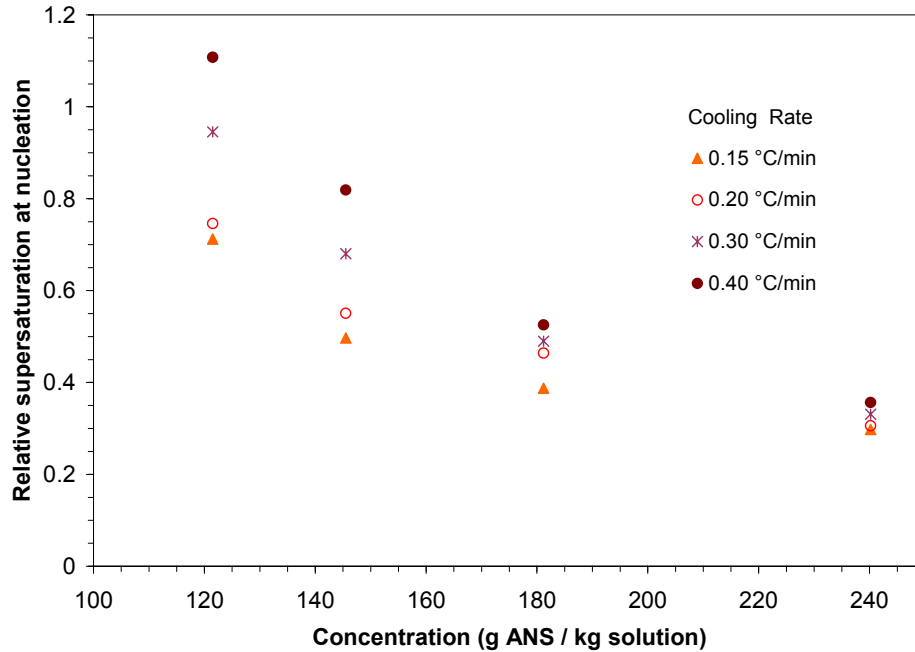


Figure 3-6. Relative supersaturation necessary to induce nucleation for solutions of naproxen sodium in water in cooling batch crystallization. Equilibrium concentration values for 104.3 and 121.5 g ANS / kg solution were estimated from multiple regression of solubility.

Kim estimated that the transition point between DNS and the next lower hydrate in the enantiotropic phase diagram of naproxen sodium was above 27.2°C, which was the upper temperature limit of his work.⁶⁷ A closer look at the data found in the higher temperature range of the present work, as seen in Figure 3-3, reveals a slight difference in solubility behavior at higher temperatures. The van't Hoff plot of the data in Figure 3-7 shows a discontinuity between the dihydrate line at the right and the next form at the left. The linear fits show correlation coefficients of 0.9993 and 0.9991 for the dihydrate and the other pseudopolymorph, respectively. The lines intersect at 29.8 °C indicating the transition point between pseudopolymorphs.

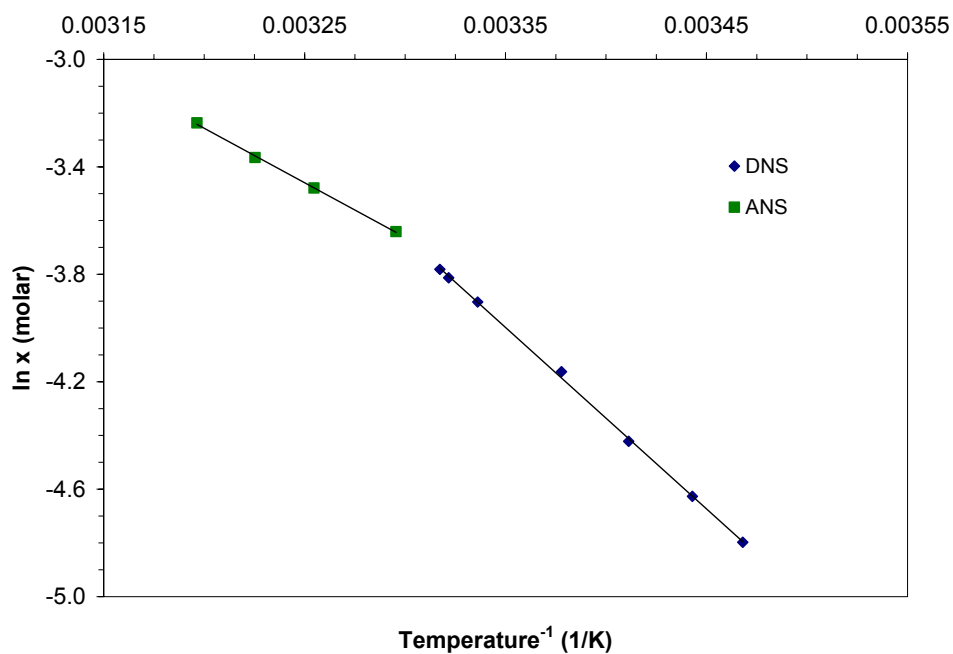


Figure 3-7. Van't Hoff plot for naproxen sodium solubility data.

A separate experiment was conducted at a concentration of 333.7 g ANS / kg solution, with a cooling rate of 0.2 °C/min with the purpose of identifying the stable

pseudopolymorph in the higher temperature range. A sample of the crystallized material was vacuum filtered, washed with cyclohexane to flush water from the crystals, and dried at room conditions for 24 hours. Powder X-ray diffraction (PXRD) was performed on a sample of the dried material with a Phillips PANalytical X'Pert PRO (CuK α radiation, 1.541 Å wavelength). PXRD patterns showed peaks that coincide with DNS and ANS according to findings by Kim, et al.² (Fig. 3-8). Monohydrate naproxen sodium (MNS) peaks were not distinctively identified, but some of these coincide with those of the two other forms at lower intensities.

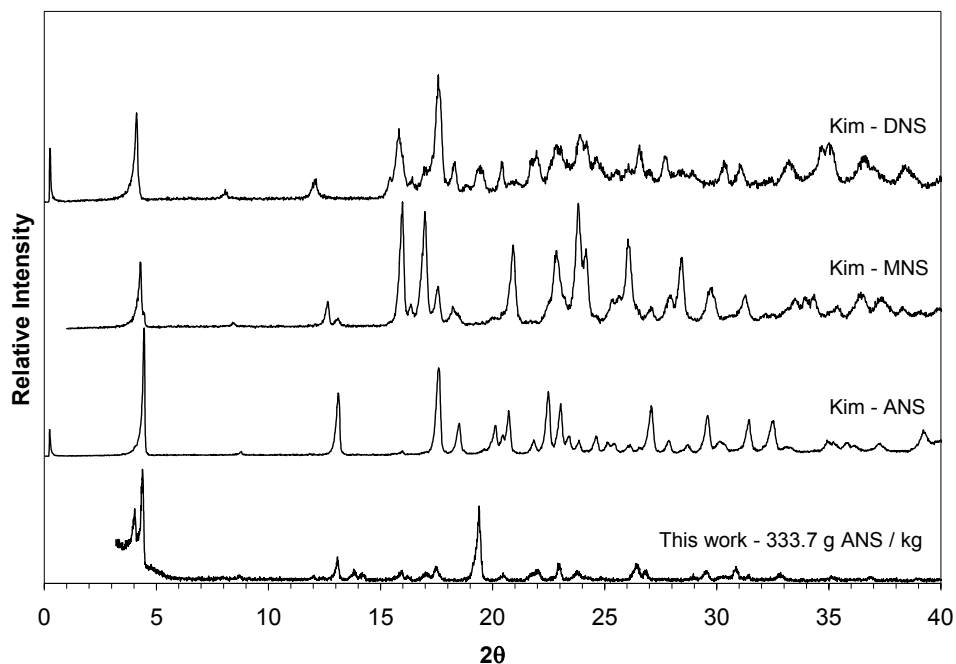


Figure 3-8. PXRD patterns for ANS, MNS and DNS by Kim⁶⁷ and for the experiment performed at a concentration of 333.7 g ANS / kg solution ($T_{\text{sat}} = 36.9\text{ }^{\circ}\text{C}$).

These results can be interpreted in different ways. For example, the metastable limits between ANS and DNS are very close at the supersaturation level and conditions of the experiment, so that cooling produces both forms of crystals. On the other hand, if only ANS had been produced, there are two alternative possibilities: (1) a solvent

mediated transformation had begun at the moment of filtering at room temperature (approx. 24 °C), or (2) the crystals were hydrated from moisture in the air while drying and transformed into the most stable hydrate at ambient conditions, i.e. DNS. Regardless of the transformation or crystallization mechanism, we can conclude that ANS is the stable form at the higher studied temperature range.

In the preceding explanations we neglected to mention MNS. Clearly, it is either unstable at the studied temperature range, or it is stable only over a very small temperature range that was undetected by this study. Results by Kim⁶⁷ suggest that the stability of the monohydrate increases up to a certain extent in solutions of methanol/water. We explore the possibility of MNS being unstable in aqueous solutions at the studied temperature range in the following discussion.

The van't Hoff relationship in Fig. 3-7 is based on the equation

$$\ln x = \frac{\Delta H_{\text{soln}}}{R} \left(\frac{1}{T_m} - \frac{1}{T} \right) \quad (3-1)$$

where x is the solubility in terms of mole fraction, ΔH_{soln} is the apparent enthalpy of solution, R is the ideal gas constant, T_m is the melting point, and T is the saturation temperature corresponding to x , with both temperatures in absolute scale. Therefore, the slope of the plot is $\Delta H_{\text{soln}}/R$, and the apparent enthalpies of solution for both forms of naproxen sodium can easily be calculated as 56,185 J/mol for the dihydrate and 33,773 J/mol for the other form. Kim⁶⁷ determined from his solubility data a heat of solution for the dihydrate of 49,928 J/mol. The differences between DNS enthalpy of solution in these two studies can be attributed to different experimental methods.

Although a fit of the van't Hoff equation to the data seems to be a fine approach to observe changes in solubility behavior, its use should be restricted to ideal systems.⁴ Furthermore, this method assumes the apparent enthalpy of solution as independent of temperature. Grant et al.⁷¹ recommend a multiple regression model to fit solubility data that allows the determination of apparent thermodynamic parameters ΔH_{soln} and change in heat capacity, ΔC_p . The model fits the data to the equation

$$\ln x = -\frac{a}{R} \cdot \frac{1}{T} + \frac{b}{R} \ln T + c \quad (3-2)$$

where a , b and c are coefficients determined from the regression. ΔH_{soln} can then be determined as a linear function of absolute temperature

$$\Delta H_{\text{soln}} = a + bT \quad (3-3)$$

rather than the constant value given by the van't Hoff method, and ΔC_p as the b coefficient, or

$$\Delta C_p = C_{p(\text{solution})} - C_{p(\text{pure solute})} = b \quad (3-4)$$

Figure 3-9 shows the solubility data accompanied by the trends based on multiple regressions. Table 3-1 summarizes the results for both species. The ΔH_{soln} values found with the van't Hoff equation fall within the limits of the studied temperature ranges for both species as determined by Equation 3-3; the 56,185 J/mol determined for the dihydrate is representative of a temperature of 22.0 °C, while the 33,773 J/mol of the anhydrate will be for a temperature of 34.9 °C. These temperature values coincide with the averages of the experimental saturation temperature ranges, namely 21.8 and 35.0 °C. For the studied saturation temperature ranges, 15.2 °C to 28.3 °C for DNS and 30.3 °C to

39.7 °C for ANS, ΔH_{soln} according to equation 3-3 ranges from 58,977 J/mol to 53,582 J/mol for DNS, and 31,208 J/mol to 36,477 J/mol for ANS.

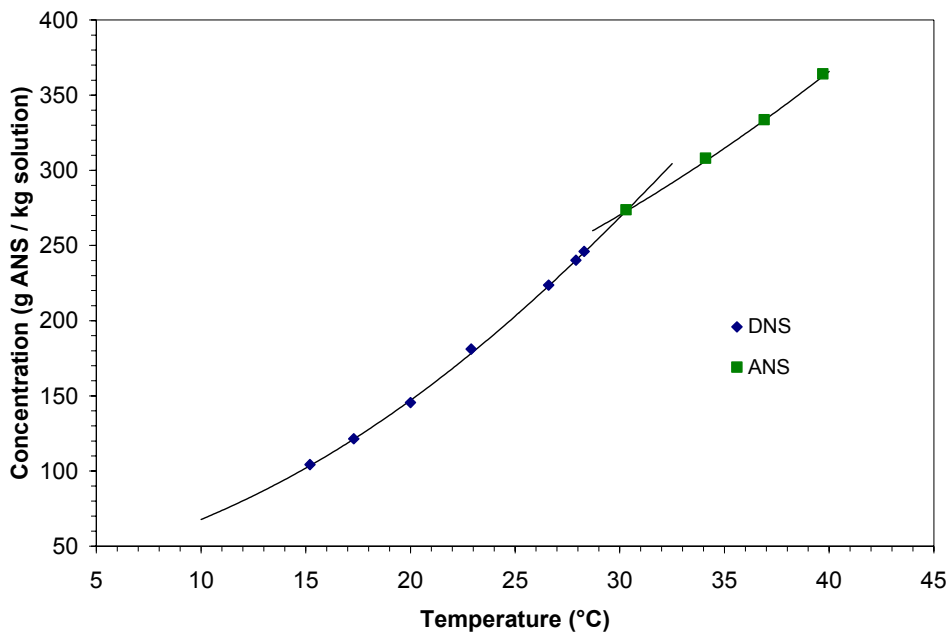


Figure 3-9. Solubility data for the naproxen sodium species and their curves as derived from multiple regression analysis.

Table 3-1. Coefficients found for naproxen sodium through regression analysis.

	Dihydrate	Anhydrate
a [J/mol]	177,731	-138,885
$b = \Delta C_p$ [J/mol K]	-411.84	560.53
c [dimensionless]	349.89	-443.99
% Max error [‡]	0.39	0.11

By finding the point of intersection of the two curves from the multiple regressions, or simply by equating them, we obtain a transition temperature between DNS and ANS at 30.3°C. This value differs from the one found with the van't Hoff method by 0.5°C.

[‡] The percentage of maximum error refers to differences between the data and the regression for the $\ln x$ values.

Figure 3-10 shows the solubility data and multiple regression fittings for the two species accompanied by their respective experimental metastable zone widths. From this we can observe closely the interaction of the metastable zones near the transition point. For example, a saturated solution at 30 °C can be cooled down to 26 °C to obtain crystals of ANS, while cooling to 25 °C or below might render a mixture of both species. The reader is referred to Threlfall's article³³ for further discussion about enantiotropic phase diagrams and their metastable zones. Since the metastable limit can only be extrapolated for DNS at higher saturation temperatures, we cannot precisely determine the proximity of the metastable limits for both forms and only speculate from the results that it is a possibility for them to be very close.

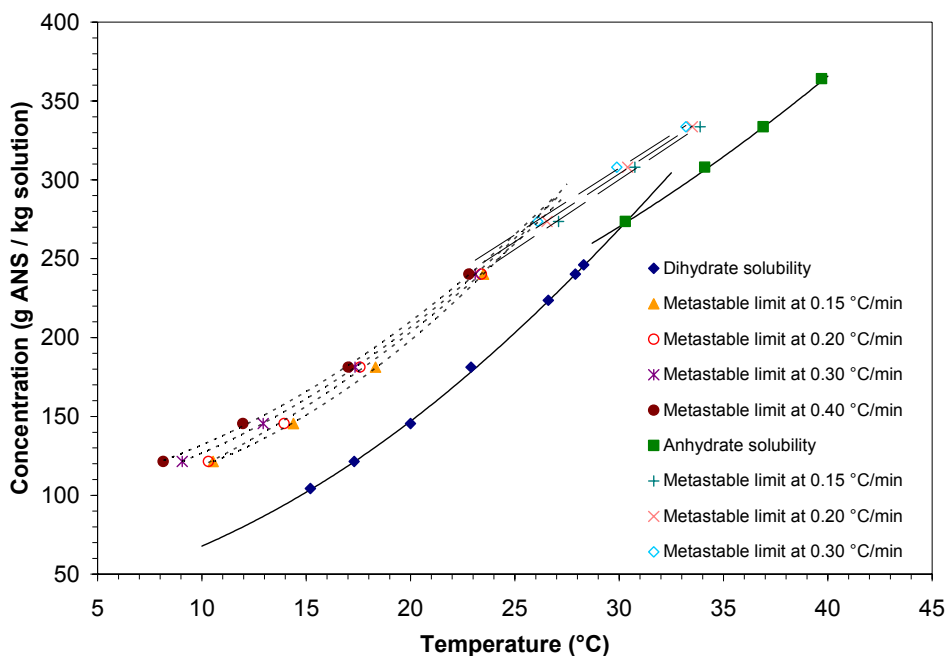


Figure 3-10. Solubility and metastable zones of naproxen sodium.

3.4 Conclusions

The solubility of naproxen sodium in water was determined with a Lasentec FBRM for a range of 15.2 to 39.7°C. The transition point between the DNS and ANS was obtained with the acquired data through two different models, van't Hoff and multiple regression fittings, at 29.8 and 30.3 °C respectively. Metastable zone and relative supersaturation behavior conforms to theory. Enthalpy of solution and change of heat capacity were also estimated.

It is recommended that further experimentation be performed for even a wider range of temperatures than those studied here, with particular focus in saturation concentrations near 30°C. This would help in determining the stability (or lack thereof) of MNS.

CHAPTER 4

**PROCESS MONITORING AND CHARACTERIZATION OF PARACETAMOL
AND D-MANNITOL CRYSTALLIZATIONS: BATCH AND LAMINAR-FLOW
TUBULAR CRYSTALLIZERS**

A Lasentec FBRM probe was used to monitor the formation of paracetamol (acetaminophen) and D-mannitol in two types of crystallizer configurations: (1) a batch system that was cooled at four different rates and (2) a system in which a cooled, laminar-flow tubular unit preceded a batch vessel that was held at the same low temperature as the jacket of the laminar-flow unit. The latter configuration is referred to here as a laminar-flow tubular crystallizer (LFTC) because supersaturation was generated in the tubular unit preceding the batch-operated vessel. Because of the rapid rate at which supersaturation was generated in the LFTC, the resulting crystals were of smaller mean size than those obtained from batch crystallizations. The total time required to relieve all of the generated supersaturation (i.e., produce a fixed mass of crystals) was significantly less with the LFTC than with the batch unit. Additionally, paracetamol was produced as two different polymorphs in the LFTC, Forms I and II. The production of the different forms resulted from the rapid rate at which supersaturation was generated in the LFTC, although the evidence suggests that solvent-mediated transformation of the less stable polymorph, Form II, to the more stable Form I took place in the batch vessel as it approached equilibrium.

4.1 Introduction

4.1.1 Background

Processes involving crystallization are common in pharmaceutical, specialty chemicals and food industries. Many companies have attempted to improve their processes through the design of novel apparatuses and methodologies.⁷²⁻⁷⁴ Crystal size and polymorphism control are often among the objectives of novel process design.

In the pharmaceutical industry, crystal size becomes important in considerations related to drug dissolution rate and tableting properties.^{22, 75-77} When the attained particle size is greater than desired, another downstream process, such as milling, is required to reduce it. Milling processes can also affect unfavorably the properties of the crystals, transforming them in some instances into other polymorphs or amorphous materials.²⁸

Differing physical properties of polymorphs of the same molecular species affect bioavailability, encapsulation, and dissolution rates. In some cases, obtaining an undesired polymorph has proven to be very counterproductive for companies.²⁹ Hence there has been an effort in industry and academia to find methods to control polymorphism by change of solvents, crystallizer design,^{3, 26, 27} seeding,^{23, 78} additives,^{24, 79, 80} and other methods.

Work by Brenek et al.,³ addressed the situation of morphology control, both in terms of crystal size and polymorphism, by the use of a laminar-flow tubular crystallizer (LFTC) for the recrystallization of a pharmaceutical product. The present work revisits the concepts suggested in the work of Brenek et al.³ by comparing the outcomes from crystallizations performed in LFTC and batch units. Several crystalline species were

included in the study. Of these species, the present chapter will focus in paracetamol (acetaminophen) and D-mannitol. Other species studied are mentioned in Appendix B.

4.1.2 Laminar-Flow Tubular Crystallizer

The LFTC resembles a tube-in-tube heat exchanger which transports the solution of interest through the inner tube, while cooling with water flowing countercurrently through the outer tube. The small size of the inner tube (3.175 mm ID) compared to the size of the outer tube (11.11 mm ID), the length of the crystallizer (7.62 m) and the velocity of the fluids (10.8 to 47.2 mL/min inside, 1.27 L/min outside), allow efficient heat transfer between the fluids with minimum temperature change in the cooling fluid. (Heat transfer models of the system are explained in Appendix C).

As discussed in Section 2.2, higher cooling rates in batch systems increase the width of the metastable zone. Furthermore, a fast initial cooling can push the system to cross the metastable limit promoting uncontrolled crystallization and the formation of fines. Often in batch crystallization this is not desired; instead, a constant supersaturation is used to provide a narrow size distribution with a large mean crystal size, sometimes aided by seeding.⁷ One purpose of the LFTC is to produce crystals with a smaller size than typically obtained from well-mixed batch systems. This is possible due to the high supersaturation that the solution reaches shortly after entering the LFTC.[§] High supersaturation levels are maintained during most of the length of the crystallizer and while the solution (or slurry) is contained at a receiving vessel, where the supersaturation is consumed and yield is maximized.

[§] See Appendix C for more details about heat transfer in the LFTC and its relationship to supersaturation.

Because the LFTC experiences laminar-flow, we expect velocity profiles along its length, or a gradient as seen from the axial direction. This means that the material at the center of the tube will spend less time inside the LFTC than that along the walls. For Newtonian fluids traveling along the length z through a circular tube with laminar-flow,

$$\bar{v}_z = \frac{v_{z,\max}}{2} \quad (4.1)$$

$$v_z = v_{z,\max} \left[1 - \left(\frac{r}{R} \right)^2 \right] \quad (4.2)$$

where \bar{v}_z is the average velocity, $v_{z,\max}$ is the maximum velocity, v_z is the velocity at a radius r and R is the radius of the tube. The model assumes no changes in the properties of the fluid along the length of the tube and “no-slip” conditions along the walls. Following these equations, velocity profiles for the different average flow rates can be easily determined for the LFTC. Figure 4-1 shows the velocity profiles for three different flow rates on the LFTC. As is apparent from the figure, flow through the LFTC deviates greatly from plug flow. The non-uniform velocity distribution contributes to the axial dispersion of the solution. If a tracer were to be injected into the LFTC at normal operation, the convection effect due to the velocity variation across the cross section would disperse the tracer axially. Such dispersion can be modeled in terms of the concentration distribution of the tracer. The mathematical model for axial dispersion in laminar tube flow was originally developed and verified experimentally by Taylor⁸¹ in 1953. A recent publication by Ekambara and Joshi⁸² reviews the significant amount of work that has been performed on axial mixing in laminar pipe flow.

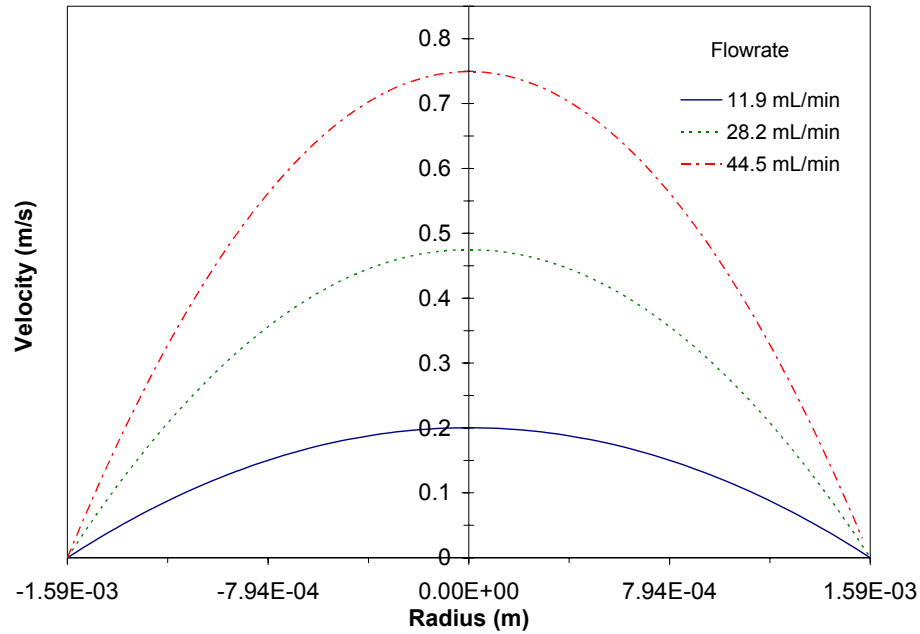


Figure 4-1. Velocity profiles for different flowrates in the LFTC.

In the event of crystal nucleation inside the tube, the axial dispersion resulting from the parabolic velocity profile would result in the production of smaller crystals at the center of the tube, where the solution resides the least amount of time. Crystal size would then increase as the profile approaches the wall of the tube. As we will see, this can also be explained quantitatively with the assistance of residence time distributions (RTD).

For laminar-flow systems, like the LFTC, the age RTD $E(t)$ function is

$$E(t) = \begin{cases} 0 & t < \frac{t_m}{2} \\ \frac{t_m^2}{2t^3} & t \geq \frac{t_m}{2} \end{cases} \quad (4.3)$$

where t is time and t_m is the mean residence time, as defined by the total volume of the LFTC's inner tube over the average flow rate (or length of the LFTC divided by the mean velocity). (A complete derivation of the equation can be found elsewhere).⁸³ Figure 4-2 shows the RTDs for three different flow rates in the LFTC used in the present study. The plot is useful for better understanding of the flow patterns in the crystallizer. For example, for a volumetric flow rate of 44.5 mL/min, we see that the vertical asymptote reaches a value of 10.17 seconds, the time that it takes for a point of solution to go through the LFTC right at the center of the tube, where the velocity is at its maximum. For this flow rate, the mean residence time is 20.34 s. If we integrate the area under the curve between 10.17 s and 20.34 s, we find that 75% of the feed to the system resides in the LFTC between these two times. This type of information can also be acquired through a cumulative RTD $F(t)$ plot, in which,

$$F(t) = \begin{cases} 0 & t < \frac{t_m}{2} \\ 1 - \frac{t_m^2}{4t^2} & t \geq \frac{t_m}{2} \end{cases} \quad (4.4)$$

Figure 4-3 shows this type of plot for three different flow rates through the LFTC. Taking again the 44.5 mL/min example, we can see how $F(t)$ goes from 0 to 0.75 in the period from 10.17 to 20.34 s.

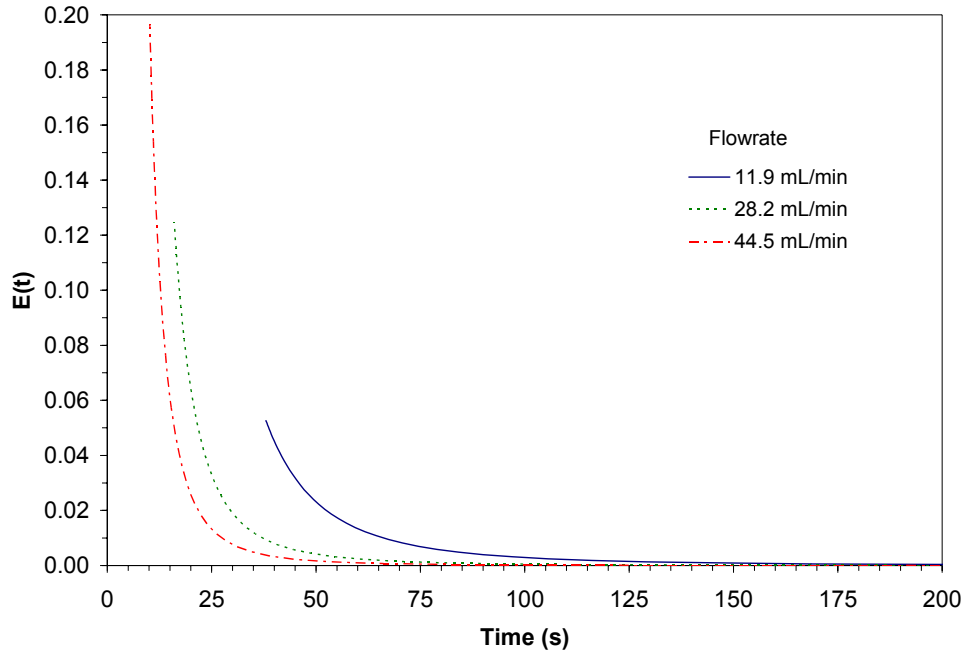


Figure 4-2. Residence time distribution for different flowrates through the LFTC. Mean residence time for 11.9 mL/min was 76.05 s, for 28.2 mL/min was 32.09 s, and 20.34 s for 44.5 mL/min flowrate.

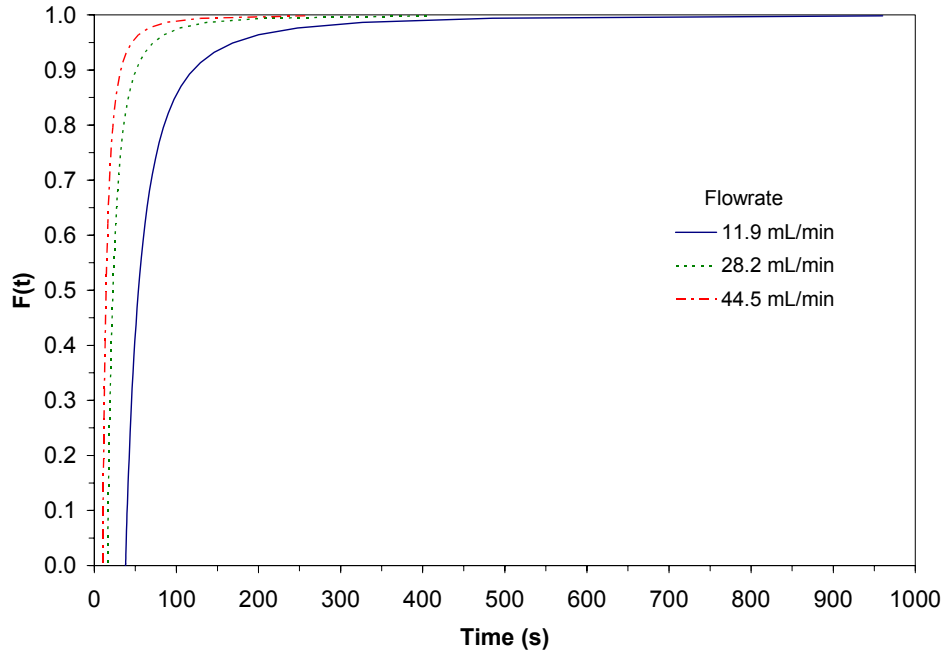


Figure 4-3. Cumulative residence time distribution for different flowrates through the LFTC.

As we see from the RTD, the solution does not spend a uniform amount of time in the LFTC and therefore, we cannot assume that the formed crystals will have a narrow size distribution.

Although experiments with plug flow were not performed, it is significant to bring to the attention of the reader the importance of such flows in terms of size distributions and RTD. In plug flow, turbulent flow inside the tube would result in no axial dispersion effects, translating into a narrow age function $E(t)$. This is generally represented by a spike in the RTD plot. Velocity then is not represented by a parabolic profile like in laminar-flow, but rather by a flat plug. Because plugs of material travel at the same speed and with the same residence time, in the event of nucleation, the formed crystals should have the same size, hence a narrow distribution.

4.1.3 Polymorphism

In 1897 Wilhelm Ostwald published what has been known as the Ostwald rule of stages.³⁵ He explained that in a polymorphic system, the first polymorph to crystallize would be the one that is kinetically stable (or “unstable”), rather than the one that is thermodynamically stable (although there are numerous exceptions to the rule). In other words, in crystallization, a system will go to that state in which the loss of free energy is minimal. When the unstable polymorph is obtained and left in solution for a sufficient amount of time, a solvent-mediated transformation might occur, in which crystals redissolve to crystallize this time as the thermodynamically stable species. Hence, if the unstable polymorph is desired, the crystals must be isolated by filtering and drying.** As

** Some materials might convert to another polymorph in certain temperature and pressure conditions, even when they are not in a solution, through a solid-state transformation.

discussed in Section 2.3, because an unstable polymorph at a certain set of conditions would have a higher solubility than the stable one, a fast cooling with high supersaturation levels would then enable the crystallization of the unstable polymorph at a particular temperature range. Brenek et al.³ were able to produce and isolate an unstable polymorph of a pharmaceutical product utilizing a LFTC without concomitant production of the stable form, while at the same time producing crystals of smaller size than those produced in a batch crystallizer. They did not have to add seed crystals of the metastable material in order to produce it.

4.1.4 Materials used

4.1.4.1 Paracetamol

Paracetamol (acetaminophen) is a widely used antipyretic and analgesic often found in over-the-counter drugs. Three polymorphs of paracetamol have been identified, with the monoclinic crystal (Form I) being stable at room conditions. Much attention has been focused on the production of Form II, an orthorhombic crystal, whose sliding planes allow it to have much better compressibility than Form I.⁷⁷ The monoclinic form used in drug products lacks sliding planes and requires binding agents for the tableting process, which adds cost to its production.^{75, 77} Form II has been obtained by crystallization from melts,⁷⁷ yet this process is disadvantageous for production on large scale. For this reason Nichols and Frampton⁷⁵ focused on the production of Form II from ethanol solutions in laboratory-scale batch crystallizers with the assistance of seeds obtained from melting crystallization. The researchers found that an unseeded batch would yield Form I, and that solvent-mediated transformation from Form II to I can occur easily. They

recommended crystallizing at temperatures below 5 °C to retard the transformation process. Due to these difficulties, the authors noted that there is a need for extensive optimization for process scale-up. Other researchers^{78, 84} have then looked to optimize the parameters to maximize the formation of Form II in batch crystallizers. Form III crystals have been obtained by melting crystallization and have proven to be elusive to isolate and retain for characterization.^{75, 77, 85}

4.1.4.2 D-mannitol

D-mannitol is an acyclic alcohol commonly used as an excipient in tablets by the pharmaceutical industry. Its non-hygroscopic characteristics make it useful as an excipient for moisture sensitive drugs. It is also commonly used in chewable tablets that rapidly dissolve in the oral cavity; its negative heat of solution gives a cooling sensation in the mouth.⁸⁶ Three different polymorphs have been identified for D-mannitol, here referred as α , β and δ , following the nomenclature by Walter-Lévy.⁸⁷ All three forms have been characterized by multiple methods, including powder XRD, DSC, FTIR, and FT Raman among others.^{22, 86, 88-90}

Crystallization protocols can also be found in the literature for all three forms. The β polymorph, which is stable at room conditions, can be easily obtained by cooling batch crystallization, and is the usual commercial product.²² The α form can be obtained by crystallization from 70% ethanol.²² The δ polymorph can be produced by cooling rapidly a hot saturated solution of D-mannitol (for example, in water,²² dilute aqueous acetone solution,⁸⁶ or dilute aqueous ethanol solution⁸⁸) to 0 °C or below, and filtering

rapidly. It also can be obtained by precipitation from an aqueous solution by adding acetone or by freeze-drying.²²

Although it has been reported that moisture can induce transition of the δ form of D-mannitol to the more stable β polymorph,⁸⁶ it has also been shown that it is the form with better tableting behavior of the three.²² Although at room conditions it is thermodynamically unstable, it shows great kinetic stability, by being durable over a period of at least 5 years at 25 °C if kept dry. Also, mechanical stresses, such as grinding and tableting, do not cause a transition of the δ polymorph to either of the other forms.²²

Taking these two examples, paracetamol and D-mannitol, we can see how important it is to find crystallization processes that are able to produce and retain an unstable polymorph.

4.1.5 Process monitoring

As part of the characterization process, a Lasentec FBRM D600 along with online temperature recording were used to acquire chord-length and nucleation-relevant data in both batch and LFTC operations.

For the purpose of relative size comparisons throughout this chapter, we will use the median and mean values of the chord length distribution (CLD) obtained by the FBRM. No weighting was applied to either value, and therefore they represent number average quantities.

A method described by Euhus⁹¹ was used in this work to relate the zeroth moment of the chord-count density function to the nucleation rate of the systems under study. The derivative of the total number of crystals with respect to time is, by definition, the

nucleation rate. The method is hereon briefly described, but the reader is directed to the work of Euhus⁹¹ for further details.

Based on a population density function, a chord-count density function $c(l)$ is defined as,

$$c(l) = \lim_{\Delta l \rightarrow 0} \frac{\Delta C(l)}{\bar{V}_S \Delta l} \quad (4.5)$$

where $\Delta C(l)$ is the number of chord counts with lengths between l and $l + \Delta l$ in the volume of slurry or liquid scanned by the FBRM probe, \bar{V}_S . This volume is defined on estimates of the scanning specifications of the probe. These specifications are: the depth that the laser beam effectively penetrates λ , its width b , and its scan speed along the path \dot{v}_S . Then, the volume scanned over any period of time Δt can be approximated by the equation,

$$\bar{V}_S = \dot{v}_S \lambda b \Delta t \quad (4.6)$$

Values used in this work for the aforementioned variables were, $\lambda = 1.50 \times 10^{-3}$ m, $b = 5.80 \times 10^{-6}$ m, and $\dot{v}_S = 2$ m/s.

Randolph and Larson⁴⁶ have shown that the zeroth moment of the population density function is related to the total number of particles per unit volume. Using a chord-count density function allows us to do the same, since the number of chords registered by the FBRM should be identical to the total number of crystals in a specific scanned volume. The zeroth moment \bar{m}_0 of the chord-count density function is,

$$\bar{m}_0 = \int_0^{\infty} c dl \quad (4.7)$$

which is the total number of particles per unit volume N_{total} . By neglecting crystal attrition and agglomeration, the nucleation rate J_0 in a well-mixed vessel is,

$$J_0 = \frac{dN_{total}}{dt} = \frac{d\bar{m}_0}{dt} \quad (4.8)$$

By considering CLD data from the FBRM, where counts per second are relayed in specific chord lengths, a simple spreadsheet can be developed in which the zeroth moment is calculated based on the effective scanned volume. The derivative of these zeroth moments over time, would then give us the nucleation rate of the system. As seen in Figure 4-4, the derivative of the zeroth moment, increases rapidly, reaches a maximum value, and then decreases rapidly to a near-zero value. In this study the characteristic nucleation rate in a given run was defined as the value at the maximum.

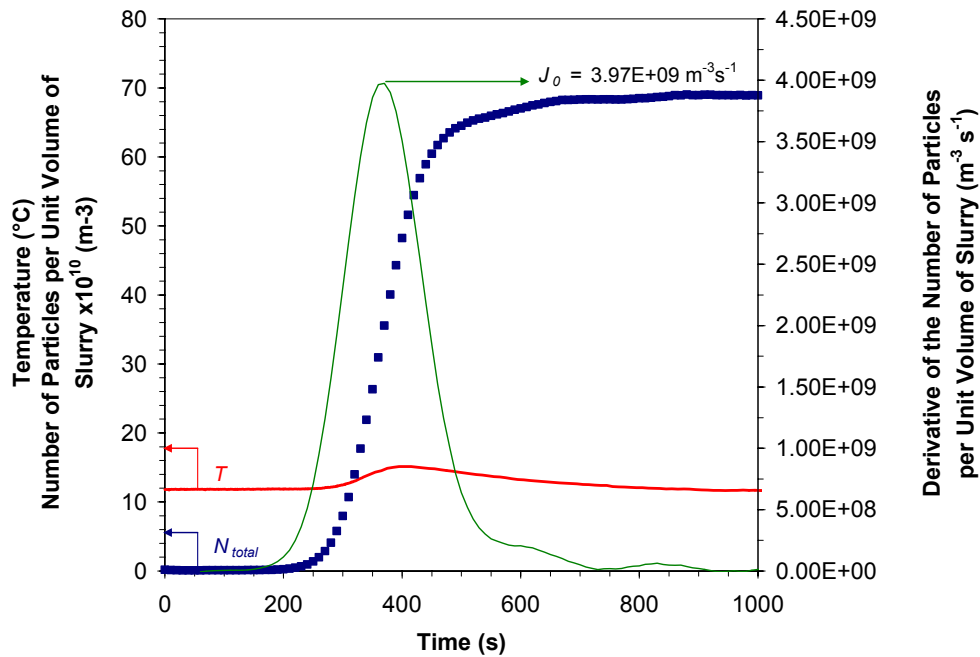


Figure 4-4. Zeroth moment analysis for determination of nucleation rate. This graph pertains to a run of paracetamol in methanol on the LFTC with crystallization occurring in the receiving vessel.

4.2 Materials

Paracetamol (4-acetamidophenol 98%) was purchased from Acros Organics. D-mannitol, ACS, 99.0% minimum was purchased from Alfa Aesar. Ethanol 200° proof was purchased from Equistar Chemicals LP. Methanol USP was purchased from Chemcentral. Mega-pure water from a Barnstead system was also used.

4.3 Experimental

4.3.1 Batch Crystallization

4.3.1.1 Equipment

A jacketed 500-mL glass vessel (9.68 cm ID) with curved bottom was used to carry out the batch crystallizations. A four-port head allowed insertion of a stirrer, FBRM probe, thermocouple and condenser. The solution was stirred by a four-blade 5.1 cm diameter stainless steel propeller with 35° pitch rectangular blades that pumped the contents upward for better contact with the FBRM probe. Stirrer speed was maintained at 400 rpm; this provided good mixing with Reynolds numbers ranging from 10,000 to over 43,000 (depending on temperature and solvent), while avoiding excessive splashing. Three 0.635 cm diameter stainless steel baffles were also used to promote mixing and minimize vortex formation. An FBRM D600 was used to observe nucleation and chord length distributions (CLD) of crystals. The scanning rate was set to 2 m/s, with 10-second measurement duration and a moving average set to 10 measurements. The probe also served as a baffle. A condenser with a cooling fluid at about 10°C was attached to the vessel to return any solvent that evaporated. A thermocouple was submerged in the solution to record temperature, which was acquired through an Omega OMB-DAQ-56

connected to a computer. The desired cooling rates were programmed on a VWR 1157P circulator, which provided the temperature control to the vessel. The upper part of the vessel, between the jacketed area and the condenser, was wrapped with a heating cloth maintained at about 85°C (higher than the highest solution temperature) to avoid condensation of the solvent against the walls and top of the vessel.

4.3.1.2 Procedure

Both solute and solvent under study were introduced into the batch vessel at room temperature, with sufficient amount of material so that the FBRM probe tip was submerged in the solution. Following this, the vessel was heated until full dissolution was achieved, then cooled to allow crystallization, and heated again to the desired temperature set point at which the solution was to remain for 30 minutes prior to cooling at a specific rate for the first experiment in a campaign. Data recording by FBRM and temperature acquisition took place from the constant high temperature period until a time following nucleation at which the system had reached equilibrium; this was determined by FBRM monitoring of chord lengths and their mean and median values. Subsequently, the slurry was heated to the high temperature set point, to remain there for 30 minutes, before cooling to start another experiment. The procedure was repeated for different cooling rates.

4.3.2 Laminar-Flow Tubular Crystallizer System

4.3.2.1 Equipment

Figure 4-5 depicts the design of the tubular crystallizer system. A small vessel (A) of approx. 75 mL, was used to contain the solvent for flushing purposes. A 250-mL baffled glass vessel (B) contains the feed solution. The solution and/or solvent are pumped through the tubular crystallizer (D) with a FMI QG400 positive displacement pump (C) with jacketed head that allows the liquid to remain warm. The tubular crystallizer is made of a 7.62 m long inner PTFE tube (1.5875 mm ID, 3.175 mm OD), which transports the solution, surrounded by a 11.11 mm ID (12.70 mm OD) PTFE tube containing the heat-transfer fluid in counterflow. The LFTC is coiled together in a circular fashion, and covered by two layers of 0.95 cm elastomeric foam wrap to minimize the heat transfer with the surroundings. The receiving vessel (E) is the same one used in the batch experiments, with the same setup, with the exception of not having the heating cloth. Temperature was controlled through the use of thermobath circulators maintained at the desired constant temperatures, following the layout shown in Figure 4-5. Heating tape maintained at the hot temperature was used between the outlet of the solution vessel and the three-way valve to avoid heat losses. Temperature was recorded at the solution vessel, receiving vessel, and inlets and outlets of solution and heat transfer fluid on the LFTC, through an Omega OMB-DAQ-56 connected to a computer.

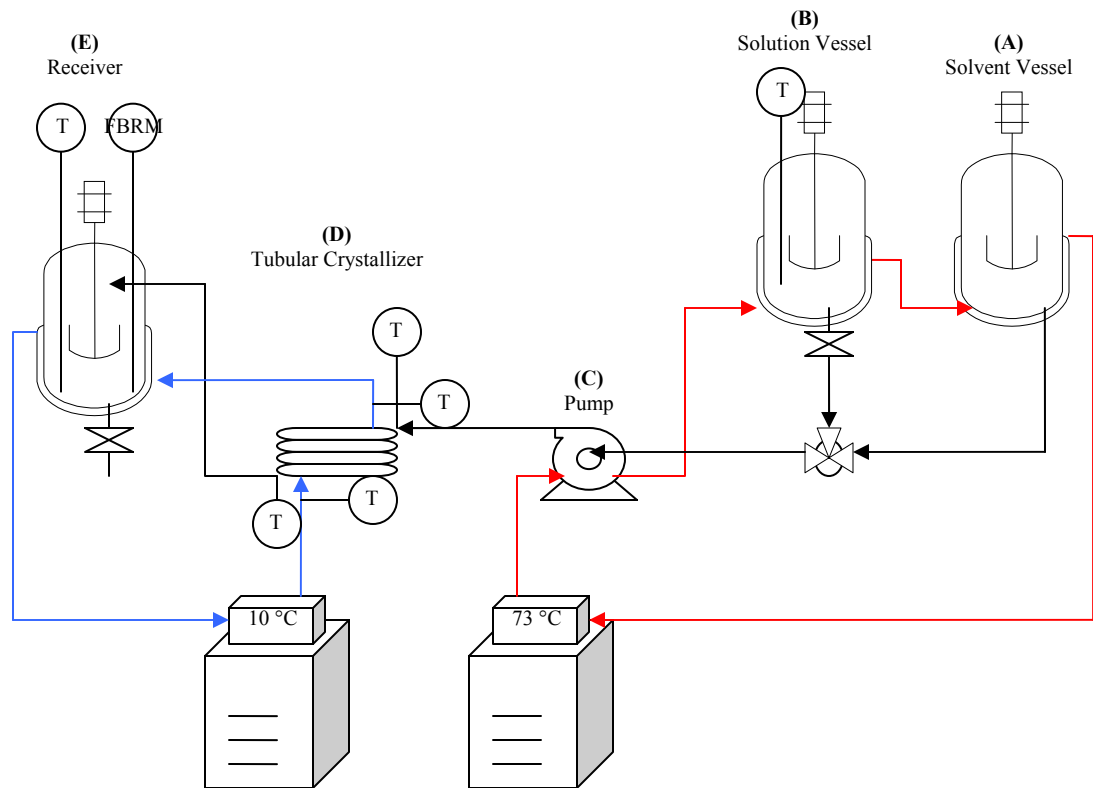


Figure 4-5. Laminar-Flow Tubular Crystallizer System.

4.3.2.2 Procedure

Prior to starting an experiment, the thermostath circulator temperatures were set at a high temperature for the pump head, solution vessel and solvent vessel, and a low temperature for the crystallizer and receiver. Similar amounts of solvent and solute that had been used in batch experiments were added to the solution vessel after the set temperatures were reached. Solvent and solute were stirred for a period of 30 minutes while the solute was dissolved in its entirety. While the solution was stirred the LFTC was flushed with warm solvent from the solvent vessel. This solvent was recovered from the outlet of the LFTC to another vessel, such as a beaker, and discarded. After the solvent was pumped and no more drops were observed coming through the outlet of the

LFTC, the pump was turned off and the outlet tube was introduced into the receiving vessel. When the 30 minutes of stirring the solution had passed, temperature data collection was started. The solution was then pumped through the crystallizer by switching the three-way valve to the solution vessel, opening the lower valve of the vessel and turning on the pump. Typical flow rates ranged from 10.8 to 47.2 mL/min (Table 4-1 shows the Reynolds numbers for flow through the LFTC according to the studied flow rates). To minimize the presence of remaining solvent from the flushing stage, the first drops coming out of the LFTC were discarded through the lower valve of the vessel. Following these drops, no flow of solution was detected for some seconds until the actual solution under study came through. The cold solution was then recovered in the receiver vessel, where data was collected through the FBRM while the supersaturation was consumed and crystallization occurred. A run was considered complete when the system reached equilibrium, which was defined to be when the mean and median chord lengths became constant.

Table 4-1. Reynolds numbers for the LFTC flow based on solvents.

Water		Ethanol		Methanol	
Flow rate (mL/min)	Re	Flow rate (mL/min)	Re	Flow rate (mL/min)	Re
11.9	310	10.8	220	15.6	470
28.2	780	26.7	530	30.4	920
45.5	1260	42.9	850	47.2	1420

4.4 Results and Discussion

A complete summary of data and results used in this section can be found in Appendix D.

4.4.1 Paracetamol

Solutions of paracetamol in ethanol were prepared by dissolving 59.54 g of the solute in 175 g of the solvent (34.02 g / 100 g ethanol). Data from a recent publication⁹² were used to estimate the saturation temperature at this concentration as 50.6 °C. For methanol solutions, 90.44 g of paracetamol were dissolved in 162.5 g of the solvent (55.66 g / 100 g methanol). Since solubility data at this concentration were not found, extrapolation using a van't Hoff fit of data by Granberg and Rasmuson⁹³ resulted in an estimate of the saturation temperature to be 52.6 °C. Solubility data are shown in Figure 4-6 as van't Hoff plots.

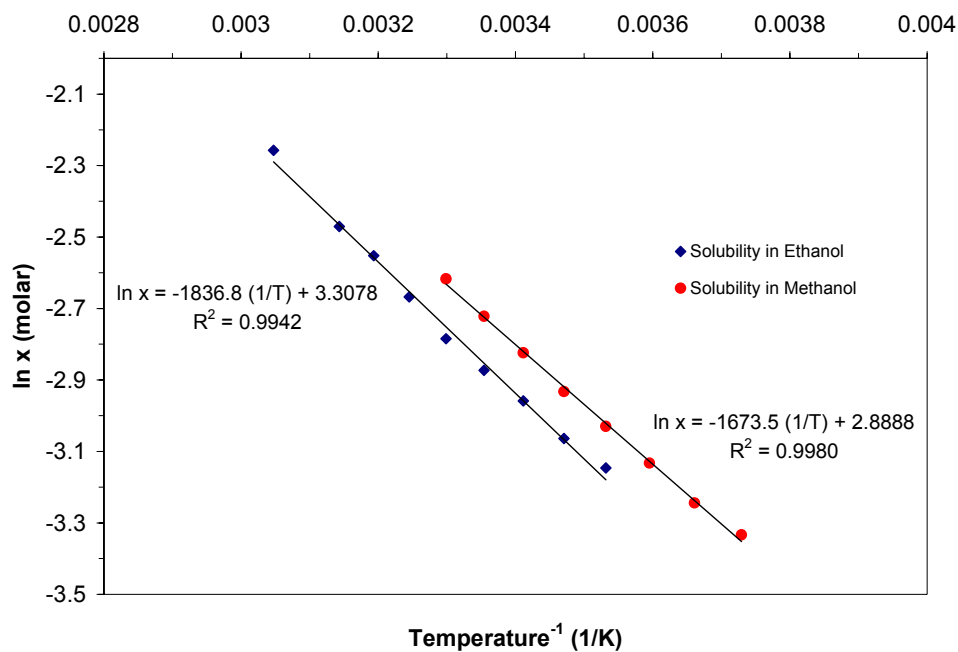


Figure 4-6. Solubility data for paracetamol in ethanol and methanol. Van't Hoff fits are shown with their corresponding regression equations for estimation of solubility. (Solubility data in ethanol from Worlistschek and Mazzotti.⁹² Solubility data in methanol from Granberg and Rasmuson.⁹³)

4.4.1.1 Batch Crystallization

Batch runs were initiated at a high temperature of approximately 69.5 °C and cooled to approximately 11.5 °C at cooling rates of 0.15, 0.20, 0.30 and 0.40 °C/min. These batch experiments focused on studying the effects of solvent and cooling rate on batch crystallization of paracetamol.

Recrystallization of paracetamol (Form I) from ethanol and methanol solutions produced crystals with a prismatic shape, as seen in Figure 4-7. The morphology of these crystals differs from that of Form II which is needle-shaped. The figure, although not entirely representative of the size distribution, shows indications of its broadness as we see from the different sizes.

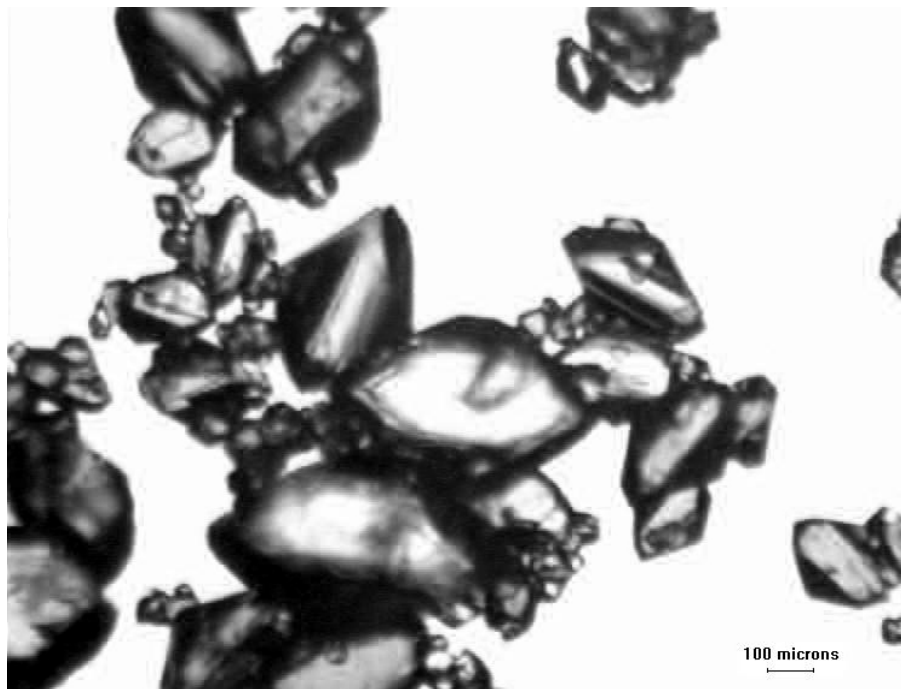


Figure 4-7. Paracetamol crystals obtained from batch crystallization of paracetamol from an ethanol solution cooled at 0.15 °C/min. The sample does not necessarily reflect the actual size distribution of the entire batch. (Image at 4x magnification).

Figures 4-8 and 4-9 show the median and mean chord lengths at equilibrium as recorded by the FBRM for the batch crystallization of paracetamol from ethanol and methanol at the studied cooling rates. Both median and mean chord lengths at equilibrium are reduced with higher cooling rates in batch operation. In other words, faster cooling rates promoted the formation of finer crystals. Comparison of chord length distributions at equilibrium obtained at different batch cooling rates, as seen in Figure 4-10 for the crystallization from ethanol, also show that with higher cooling rates an increment in counts is observed, hence a greater number of crystals. While the number of crystals increases their mean size is also reduced, as can be observed from the shift and broadening towards the left of the chord length axis.

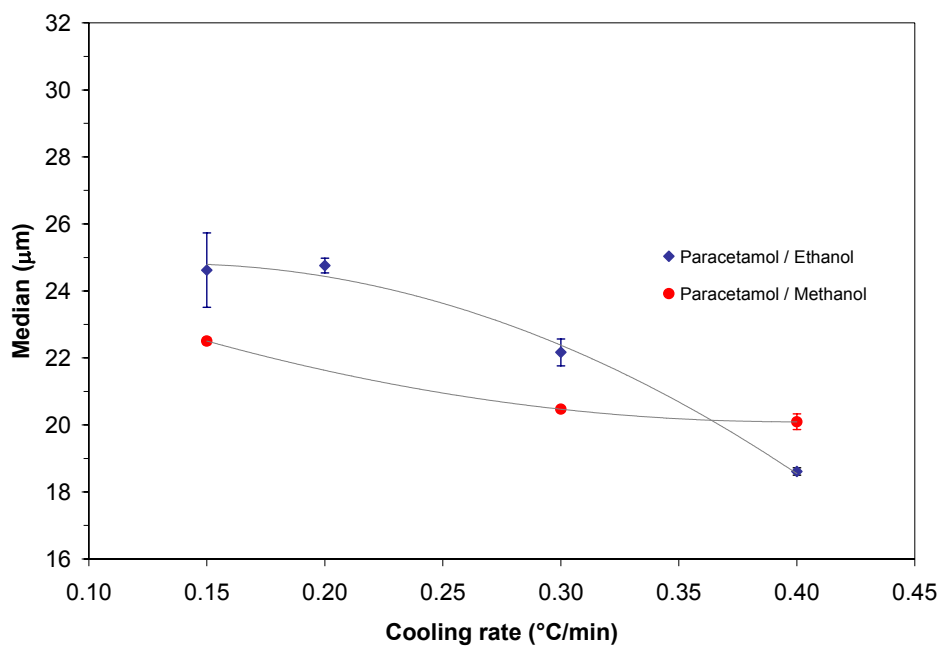


Figure 4-8. Median (no weight) values (at equilibrium) for the CLD of paracetamol crystallized from ethanol and methanol solutions.

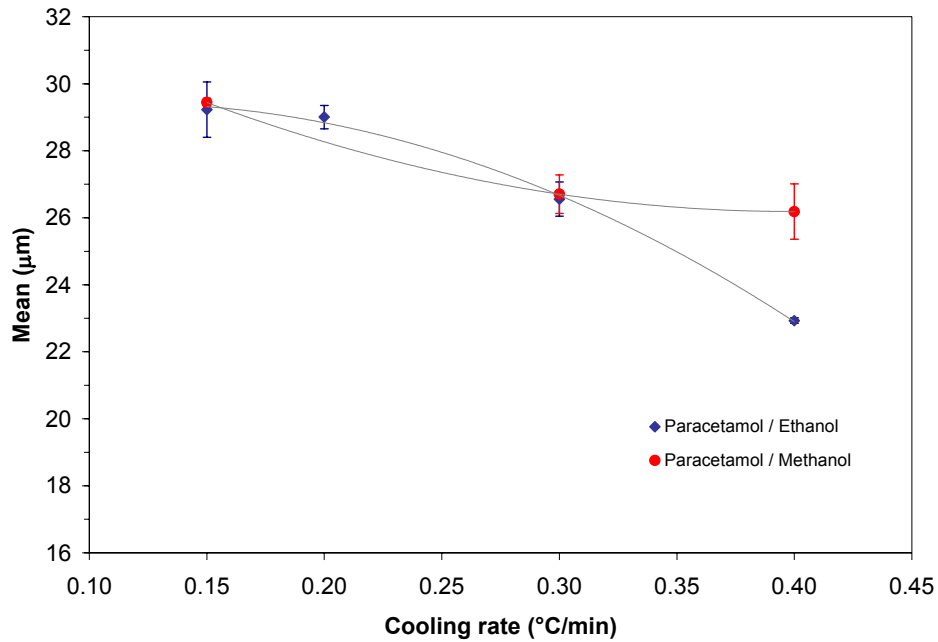


Figure 4-9. Mean (no weight) values (at equilibrium) for the CLD of paracetamol crystallized from ethanol and methanol solutions.

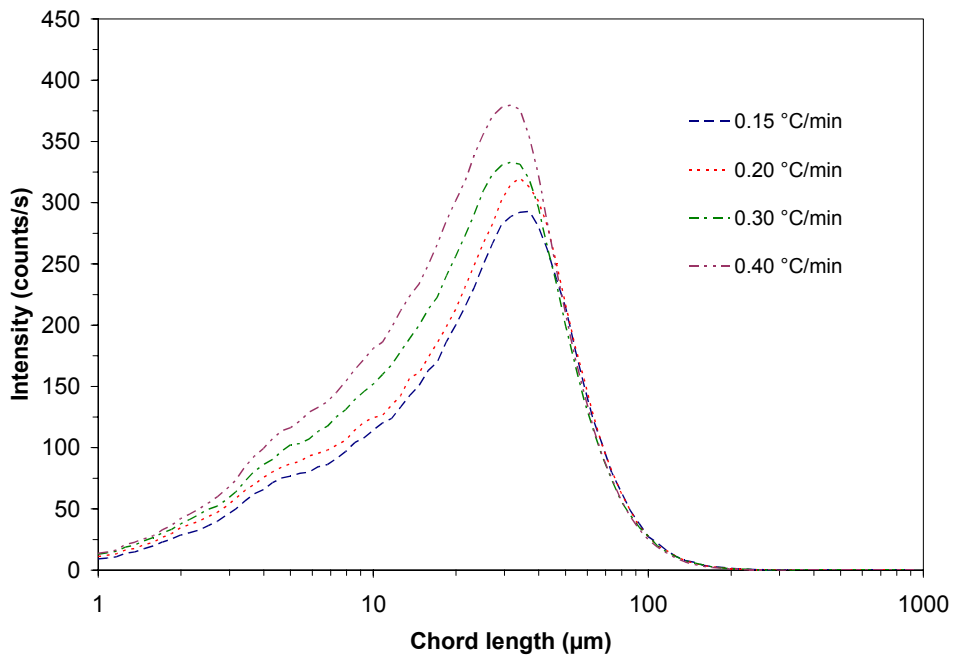


Figure 4-10. Chord length distributions at equilibrium for paracetamol crystallized from ethanol solutions at different batch cooling rates.

Figure 4-11 shows the relationship between cooling rate and nucleation rate. The formation of fines proceeds at a faster rate than the formation of coarse crystals, so it follows that higher cooling rates will translate into higher nucleation rates, as observed in the figure.

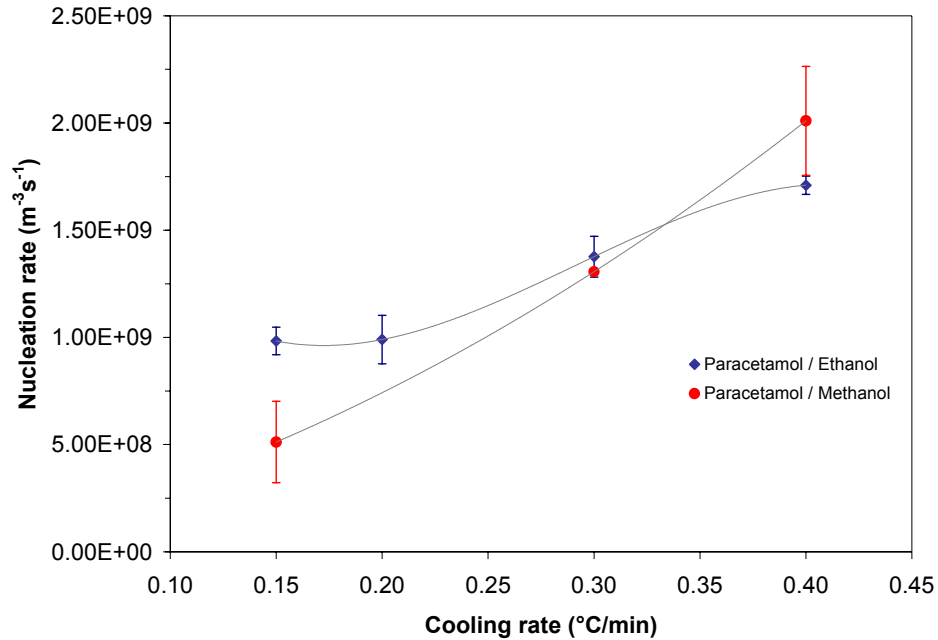


Figure 4-11. Nucleation rates determined by zeroth moment analysis for paracetamol crystallized from ethanol and methanol solutions.

Perhaps the most interesting finding while observing these data (Figures 4-8, 4-9 and 4-11) is the shift in mean crystal size and nucleation rates between ethanol and methanol solutions at cooling rates ranging from 0.30 to 0.36 °C/min. After these cooling rates the curves describing CLD median, mean and nucleation rate intersect to denote a shift between the relationships of the two systems. Figures 4-8 and 4-9 show how the crystal size is smaller for paracetamol crystals obtained from methanol solutions than those from ethanol solutions below these cooling rates, and how there is an inversed

relationship afterwards. This would indicate then that for appropriate fine crystal size control in batch operation, a selection of solvent and cooling rate must be chosen to satisfy the optimal requirements. For example, if it is required to cool at 0.40 °C/min, and slightly smaller crystals are desired, then ethanol should be the solvent of choice. Or if smaller sizes are required, but with the use of methanol as the solvent, then lower cooling rates are recommended.

At a cooling rate of 0.40 °C/min, the nucleation rate determined for paracetamol crystallized from methanol was higher than that from ethanol. Nonetheless, the crystals obtained from methanol were of greater mean size than from ethanol in terms of their CLD. This does not necessarily reflect a contradiction to the general understanding that higher nucleation rates are linked to smaller mean crystal sizes. The reader is reminded about the differences between the two systems, namely in terms of solvent, concentration and solubility, which can affect the dynamics of crystallization. Nevertheless, it is unclear if this behavior is due to measurement inconsistencies.

Figure 4-12 shows the trend of nucleation temperature at different cooling rates for the studied concentrations. We can observe a decrease in nucleation temperature with higher cooling rates. In other words, cooling at a faster rate would promote nucleation at a lower temperature than when cooling at a slower rate. As can be observed from the figure, there is about a 10 °C difference in the nucleation temperature between cooling rates of 0.15 °C/min and 0.40 °C/min for both methanol and ethanol solutions.

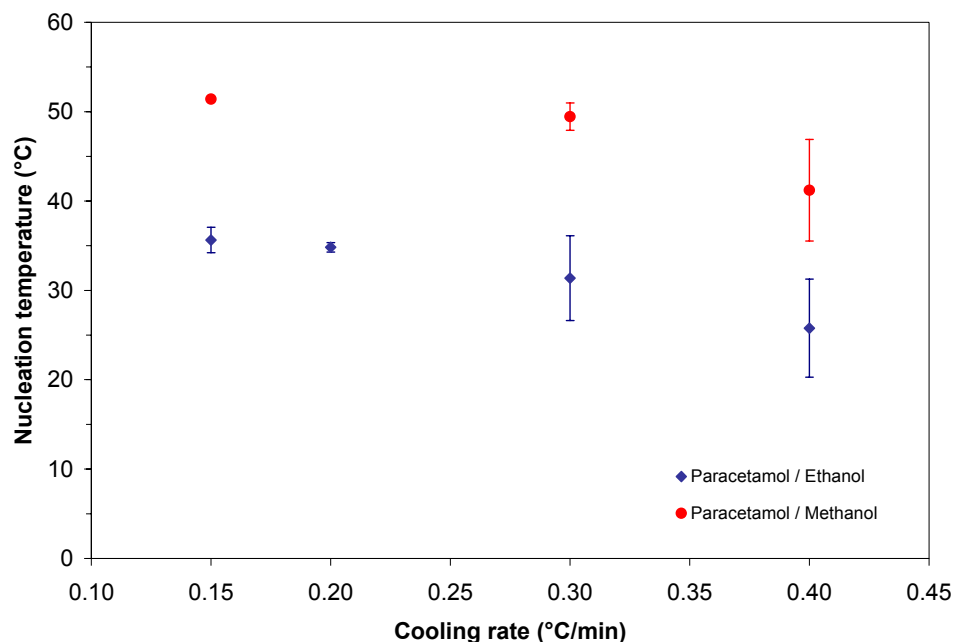


Figure 4-12. Average nucleation temperatures for paracetamol crystallized from ethanol and methanol solutions.

This tendency of lower nucleation temperatures with higher cooling rates can also be appreciated in terms of the metastable zone width. Figure 4-13 shows the temperature at which nucleation occurred for each cooling rate examined; in other words, it shows the width of the metastable zone, for the particular set of conditions experienced in these batch runs. As it can be clearly observed, the metastable zone widens with higher cooling rates. For paracetamol in methanol solutions we can observe, for example, how there is a 1.19 °C metastable limit for a cooling rate of 0.15 °C/min, and how this is expanded to 11.38 °C at a cooling rate of 0.40 °C/min. For ethanol solutions the metastable zone width increases substantially when compared to the methanol solutions. For cooling rates of 0.15 °C/min the width of the metastable zone is 14.96 °C; even higher than the one obtained for 0.40 °C/min cooling rates with the methanol solutions.

This gets even more accentuated when we observe the 24.83 °C metastable zone width for paracetamol in ethanol cooled at 0.40 °C/min.

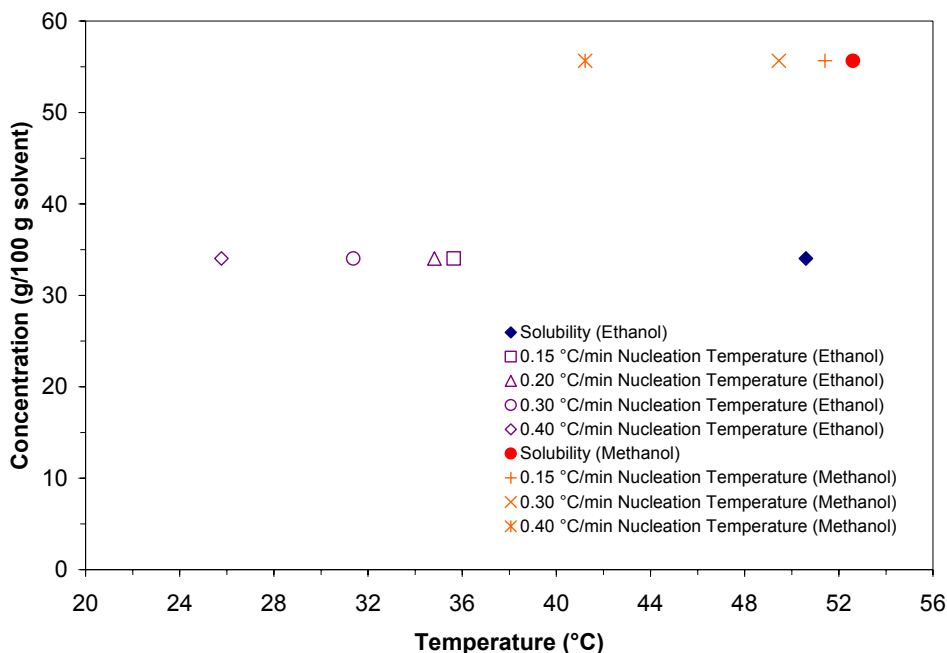


Figure 4-13. Solubility and metastable limits at different cooling rates for paracetamol crystallized from ethanol and methanol solutions.

It is also appropriate to discuss this behavior in terms of supersaturation. Departing from nucleation temperature data, Figure 4-14 depicts the relative supersaturation of the systems at nucleation. (Results are also summarized in Table 4-2). The required supersaturation for nucleation of paracetamol in methanol is significantly lower than that of the solute in ethanol. As can be deduced from the nucleation temperature data, the relative supersaturation required for nucleation to occur is higher at higher cooling rates. For an infinitesimal cooling rate, the relative supersaturation necessary for nucleation can be estimated as 0.23 for the ethanol solution and 0.005 for the methanol solution, based on extrapolation of exponential fits of the data shown in Figure 4-14.

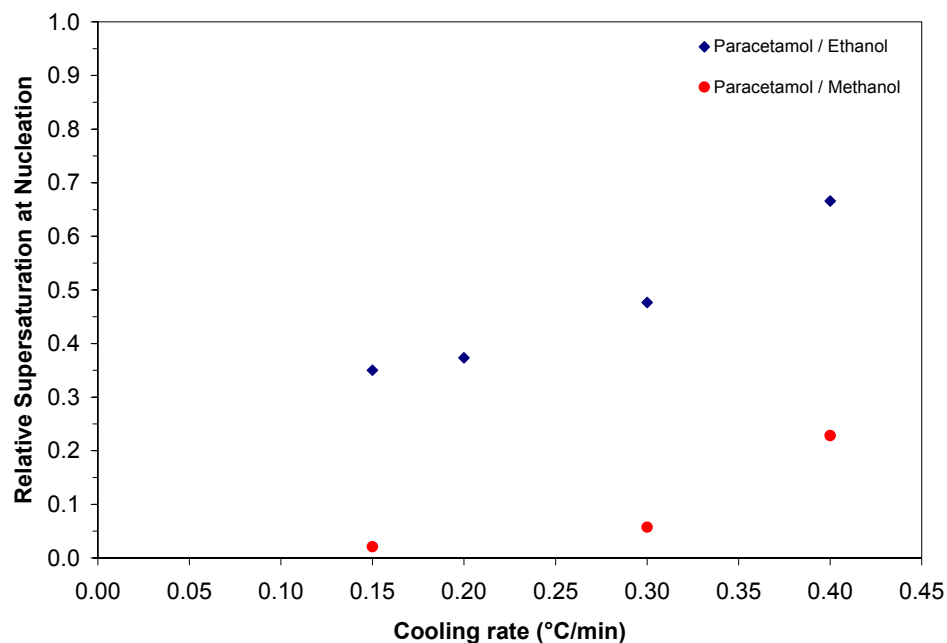


Figure 4-14. Relative supersaturation at nucleation for the crystallization of paracetamol from ethanol and methanol solutions. Relative supersaturations were calculated from nucleation temperature data and solubility calculations from van't Hoff fits of published data.^{92, 93}

Table 4-2. Summary of averaged data of nucleation temperature, metastable zone width and relative supersaturation at nucleation for paracetamol, 34.02 g / 100 g ethanol and 55.66 g / 100 g methanol, for the studied batch cooling rates.

	Cooling rate (°C/min)	Nucleation Temperature (°C)	Metastable Zone Width (°C)	Relative Supersaturation at Nucleation
Paracetamol / Ethanol	0.15	35.64	14.96	0.35
	0.20	34.82	15.78	0.37
	0.30	31.37	19.23	0.48
	0.40	25.77	24.83	0.67
Paracetamol / Methanol	0.15	51.41	1.19	0.02
	0.30	49.45	3.15	0.06
	0.40	41.22	11.38	0.23

Figure 4-15 shows how relative supersaturation of paracetamol changed with time in the batch crystallizer. The values of relative supersaturation were determined for the specified cooling rates. Data points on the figure correspond to conditions at which nucleation was observed; for example, the square marker at $t = 120$ min represents the

relative supersaturation at the instant of nucleation of paracetamol from methanol at $\sigma = 0.02$ and nucleation temperature of 51.41 °C. Due to slightly different dependencies of the solubilities on temperatures in the two solvents, saturation is reached more rapidly in the methanol solutions. This can be observed by examination of the x-axis; the relative supersaturation curves of the methanol solutions start at a lower time than those of the ethanol solutions for the same cooling rate. As a parallel to Figure 4-14, Figure 4-15 superimposes the instances of nucleation for both solutions as represented by their supersaturation. The figure, thus, appropriately demonstrates the interdependencies of relative supersaturation to cooling time and rate.

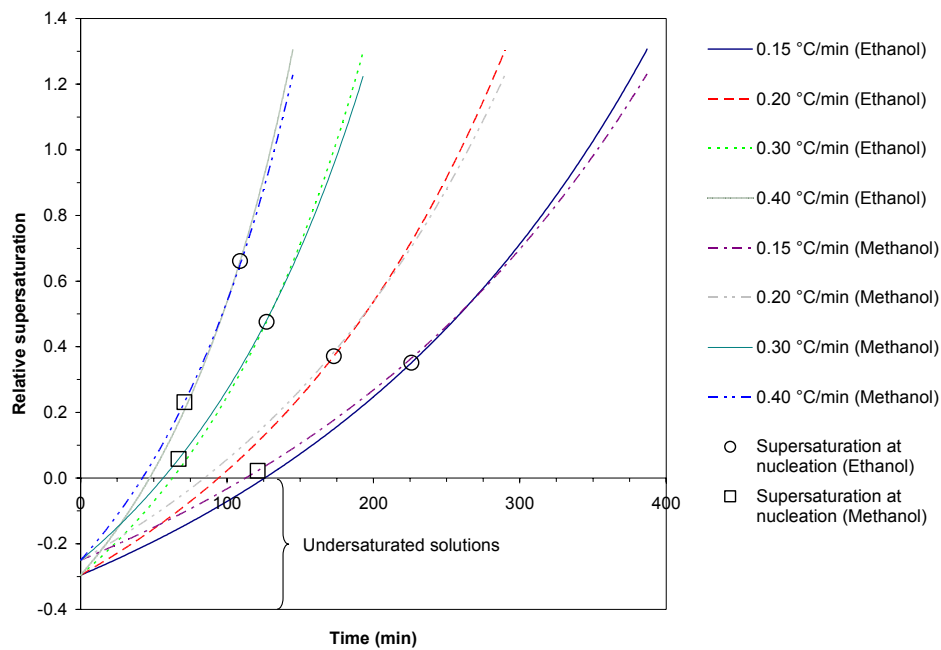


Figure 4-15. Relative supersaturation as a function of time and cooling rate for paracetamol in ethanol and methanol solutions.

As an alternative we can also consider the case in which the batch process is carried out at an initial constant supersaturation for both solutions (Figure 4-16). If we were to start the cooling of the solutions examined in this research at a relative supersaturation of -0.30 (i.e., the solutions are undersaturated), then the paracetamol solutions in ethanol are brought to saturation more quickly than are those in methanol. This is true for all cooling rates. In the experiments conducted, the runs were initiated at a constant temperature, rather than at a constant supersaturation. Accordingly, the relative supersaturation at the initiation of the runs involving ethanol solutions was approximately -0.30, but the initial supersaturation for the methanol solutions was approximately -0.25.

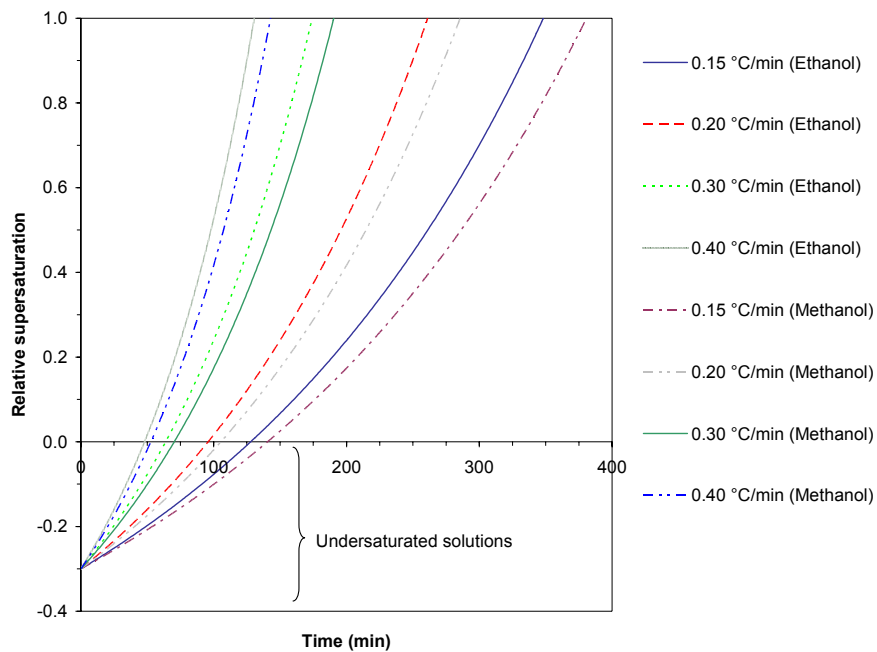


Figure 4-16. Relative supersaturation as a function of time and cooling rate for paracetamol in ethanol and methanol solutions starting at the same supersaturation.

4.4.1.2 Laminar-Flow Tubular Crystallizer System

As with the batch experiments, the initial solution temperature was approximately 69.5 °C. The temperature in the jacket of the LFTC and receiving vessel was approximately 11.5 °C. As mentioned earlier, the feed solutions were of concentrations of 34.02 g paracetamol / 100 g ethanol and 55.66 g paracetamol / 100 g methanol, using the same amounts of materials for batch and LFTC studies. Studied flow rates for the ethanol solution were 10.8, 26.7 and 42.9 mL/min. For the methanol solutions the experimental flow rates were 15.6, 30.4 and 47.2 mL/min.

No crystals were detected, either by visual inspection or FBRM readings, leaving the crystallizer tube, however nucleation events were detected by the FBRM shortly after the cold solutions entered the receiving vessel. For ethanol solutions the median and mean lengths at equilibrium were recorded as $15.02 \pm 0.35 \mu\text{m}$ and $19.30 \pm 0.34 \mu\text{m}$, respectively, while for the methanol solutions these values were $14.71 \pm 0.42 \mu\text{m}$ and $20.31 \pm 0.39 \mu\text{m}$. The CLD median and mean values at equilibrium remained practically the same regardless of the flow rate through the LFTC for the studied ethanol and methanol solutions. These CLD mean and median can then be interpreted as limiting values for laminar-flow in these particular systems.

Figures 4-17 and 4-18 superimpose the CLD obtained at equilibrium in LFTC runs and those of batch experiments. The LFTC curve shows an increase in the counts as well as a shift to the smaller values of chord length, representing the presence of more crystals with smaller mean size. The reported values for median and mean CLD are about 3 μm lower than those registered for ethanol solutions crystallized at 0.40 °C/min, and about 6 μm lower for those of methanol solutions under the same conditions. This

difference is greater when compared to batch crystallizations at 0.15 °C/min cooling rates.

As mentioned previously, due to the velocity profile and RTD of the LFTC we did not expect *a priori* a narrow distribution. Furthermore, since no crystals were observed leaving the LFTC the RTD in the tubular part of the system may play an insignificant role in determining crystal size distribution.

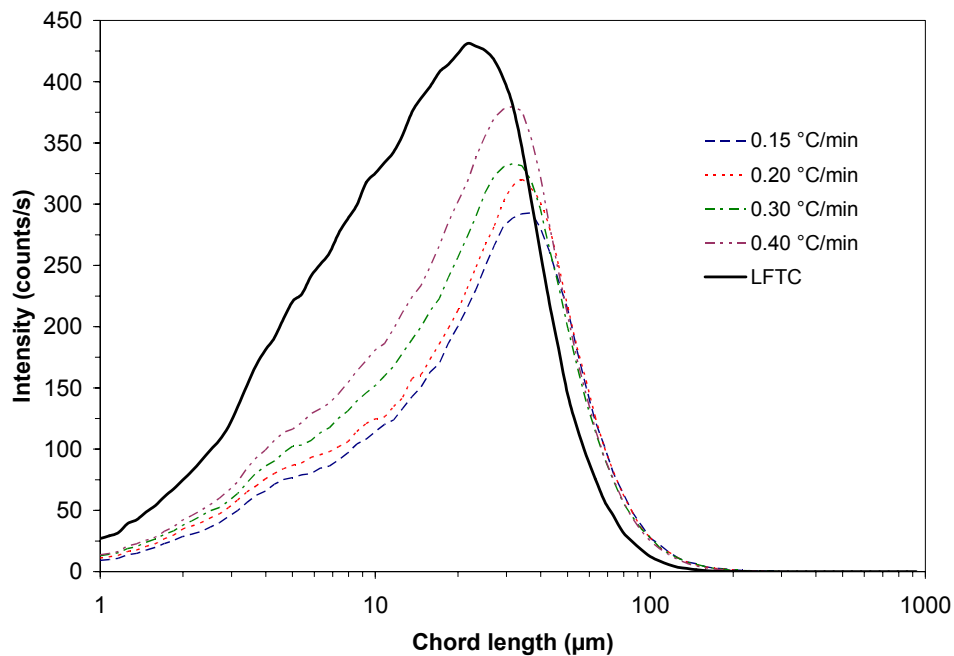


Figure 4-17. Chord length distributions at equilibrium for paracetamol crystallized from ethanol solutions at different batch cooling rates and through the LFTC.

Solutions in the LFTC experience high supersaturations during their flow through the tube. Relative supersaturations were estimated as 1.30 and 1.23 for ethanol and methanol solutions respectively at the outlet of the LFTC. These values are significantly higher than those required for nucleation in batch operation (Fig. 4-14, Table 4-2). The fact that nucleation was not observed in the LFTC can result from expansion of the metastable zone width or an inability to detect nuclei formed. As higher cooling rates

increase the width of the metastable zone, the faster removal of heat performed by the LFTC due to its large surface area and low temperatures, promotes even wider metastable zones. This in essence could have made the system incapable of producing crystals throughout its length for these particular conditions.

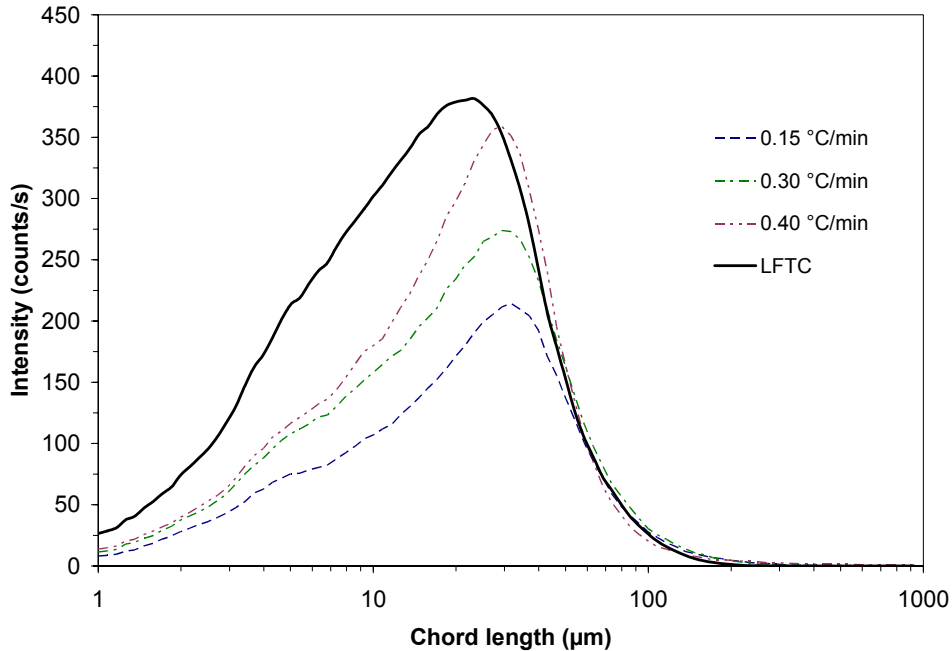


Figure 4-18. Chord length distributions at equilibrium for paracetamol crystallized from methanol solutions at different batch cooling rates and through the LFTC.

By the same token these high supersaturations promoted the formation of smaller crystals, as we have seen, by increasing also the nucleation rate. On average the nucleation rates determined for these two systems at the receiving vessel were $1.72 \times 10^9 \text{ m}^{-3} \text{ s}^{-1}$ for the ethanol solutions and $3.91 \times 10^9 \text{ m}^{-3} \text{ s}^{-1}$ for the methanol solutions; values higher than their counterparts in the performed batch crystallization experiments. As a mean for comparison, Figure 4-19 shows the average nucleation rates for batch crystallizations as columns, while comparing them to the ones obtained with the LFTC

system, represented by lines. Notice that the difference in nucleation rates is more accentuated for the paracetamol / methanol solutions.

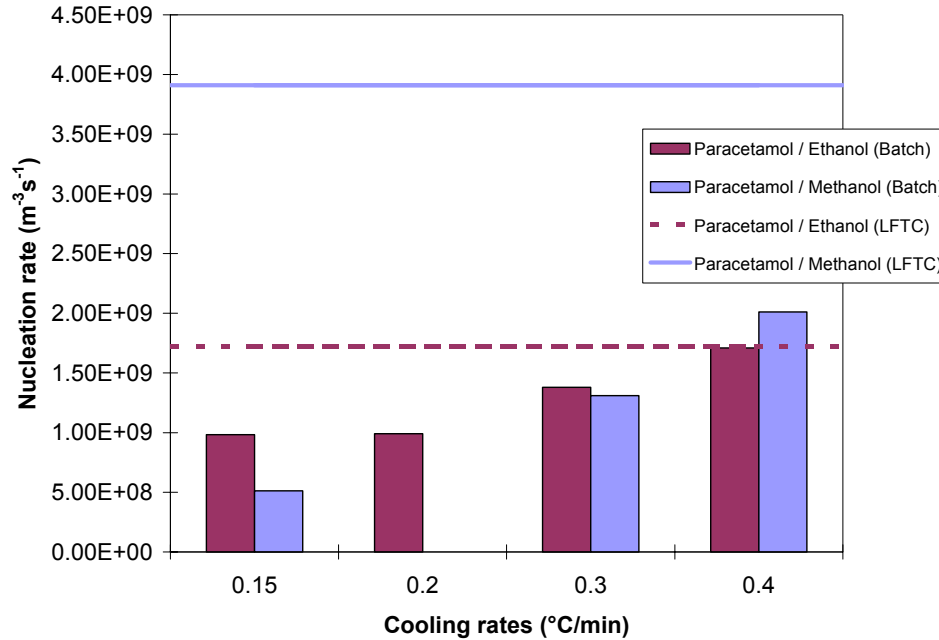


Figure 4-19. Comparison of nucleation rates for batch and LFTC system with paracetamol in ethanol and methanol solutions.

The LFTC also serves as a means of accelerating the crystallization process; while batch crystallizations can take hours according to the desired cooling rate, crystallization from warm solutions in the LFTC system can be performed in a matter of minutes, substantially reducing run time at a larger scale. For examples of this we can refer to Table 4-3. Using the described experimental setup, a batch crystallization process of paracetamol / ethanol solutions would take 4.6 to 9.0 hours to reach equilibrium in the slurry (taking into account cooling time prior to nucleation). Crystallization of paracetamol from ethanol via LFTC can crystallize and reach equilibrium in the slurry in a period of 30 to 40 minutes after being deposited in the receiving vessel. Since paracetamol in methanol requires less supersaturation to nucleate, less amount of time is

required for it to crystallize and reach equilibrium than with ethanol solutions. Depending on the conditions, equilibrium was reached in the slurry between 2.2 and 7.4 hours during batch operation. It only took about 8 to 12 minutes for the solution to crystallize and reach equilibrium in the receiving vessel after flowing through the LFTC.

Table 4-3. Average time for paracetamol solutions to crystallize and reach equilibrium in the slurry.

	Ethanol solutions	Methanol solutions
Batch Crystallization		
Cooling rate (°C/min)		
0.15	9.0 h	7.4 h
0.20	6.8 h	
0.30	5.8 h	4.7 h
0.40	4.6 h	2.2 h
LFTC Crystallization	30 - 40 min	8 - 12 min

4.4.1.3 Paracetamol Polymorphism

Figure 4-20 shows a photomicrograph of crystals obtained from a methanol LFTC run at a flow rate of 30.4 mL/min and 11.5 °C jacket temperature. The sample was obtained about 15 minutes after nucleation was detected by the FBRM. The arrows on the figure point out a few of the needle-shaped (Form II) crystals that were found in this run.

Powder XRD patterns (Phillips PANalytical X'Pert PRO, CuK α radiation, 1.541 Å wavelength, see Fig. 4-21) from the product of the same run coincide with those of Form I.⁷⁵ The sample for this pattern was vacuum-filtered and left to dry at room conditions for 24 hours prior to grinding and XRD analysis. It is likely that Form II peaks were not detected in the powder XRD pattern in Fig. 4-21 because of the great difference in mass fraction of the two polymorphs.

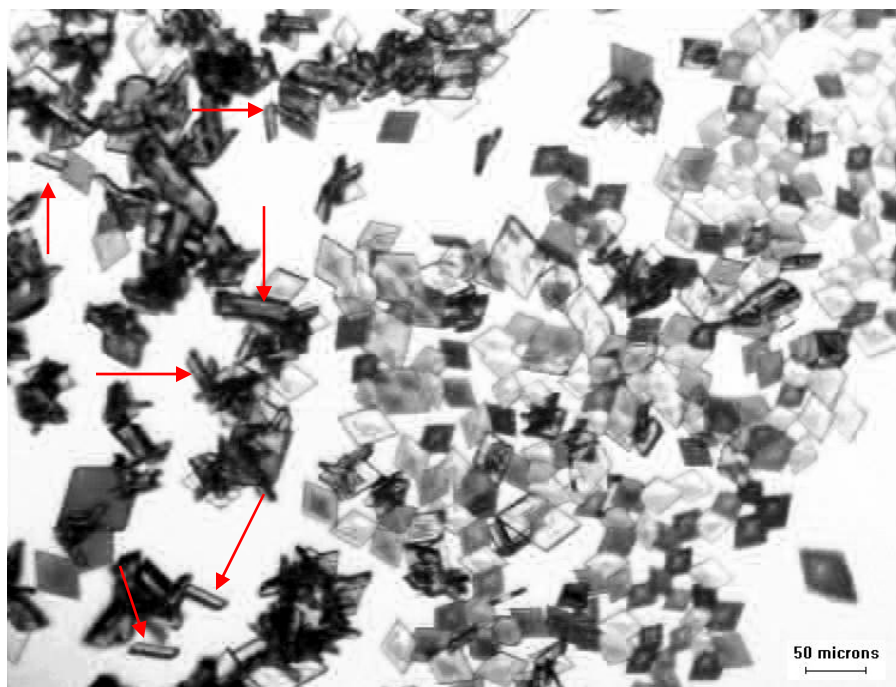


Figure 4-20. Paracetamol crystals obtained from a methanol solution through the LFTC at a 30.4 mL/min flow rate with 11.5 °C cooling temperature. Arrows indicate needle-shaped (Form II) crystals. The sample does not necessarily reflect the actual size distribution of the entire batch. (Image at 10x magnification).

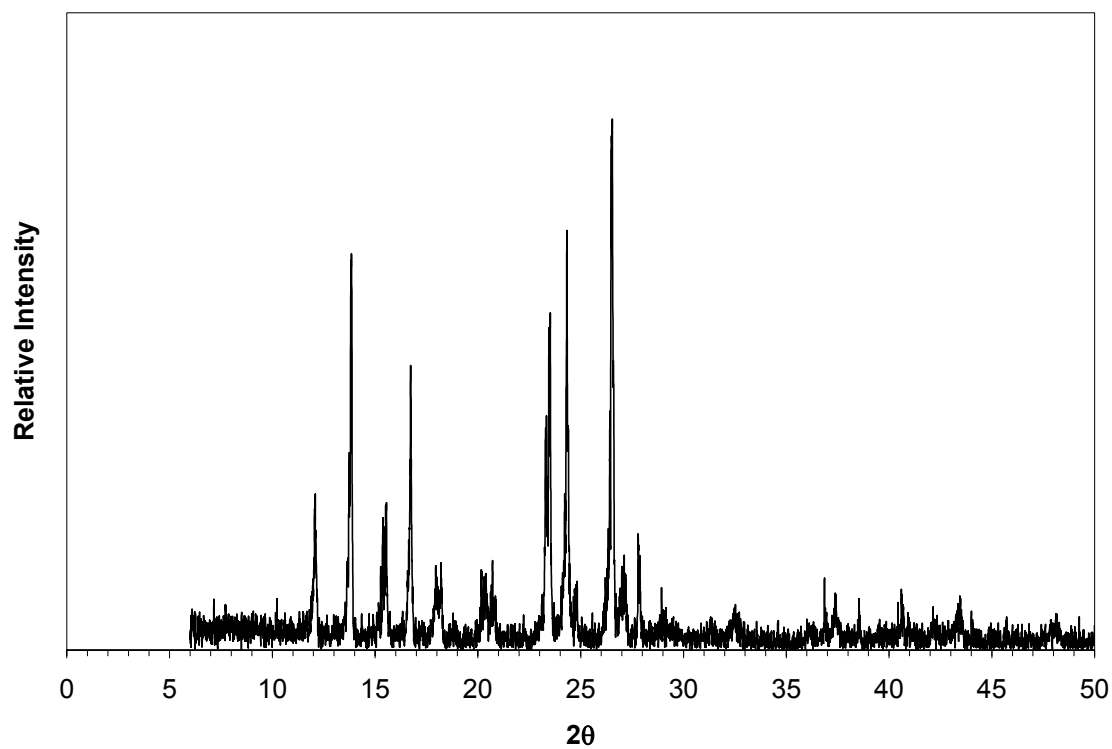


Figure 4-21. PXRD pattern of paracetamol crystallized from a methanol solution via LFTC at 30.4 mL/min and a cooling temperature of 11.5 °C.

Clearly, there was simultaneous production of the two polymorphs, with Form I being favored. Because the sample was obtained about 15 minutes after the instant of nucleation, solvent-mediated transformation of the Form II crystals might have taken place.

Motivated by the presence of Form II crystals in the aforementioned LFTC experiments at 11.5 °C, an attempt was made to maximize the formation of these crystals by maintaining the LFTC at a temperature of 3 °C for a warm paracetamol / methanol solution to flow through. A sample obtained shortly after crystallization, before reaching equilibrium, and observed through a microscope (Figure 4-22) shows the presence of both Forms I and II of paracetamol. Form II crystals are small when compared to some of the prismatic Form I crystals present in the slurry. This suggests that Form II crystals nucleated and grew to the extent that they are capable before dissolving via a solvent-mediated transformation mechanism. Through this mechanism, Form I crystals grow at the expense of the needle-shaped crystals. Nichols and Frampton⁷⁵ observed this phase transition in solution and studied it at different experimental conditions.

Figure 4-23 shows another sample of material from the same 3 °C run obtained 15 minutes after equilibrium was reached. Although there might have been a very small amount of Form II crystals present, none were observed. This verifies the presence of a solvent-mediated transformation mechanism.

As suggested by Nichols and Frampton⁷⁵, in order to retain the Form II polymorph, it is necessary to harvest the crystals shortly after the nucleation event. The LFTC has shown that is capable of producing this polymorph without addition of seeds,

although concomitantly with Form I. Lower operation temperatures for this crystallizer are suggested to further explore the possibility of nucleation of pure Form II.

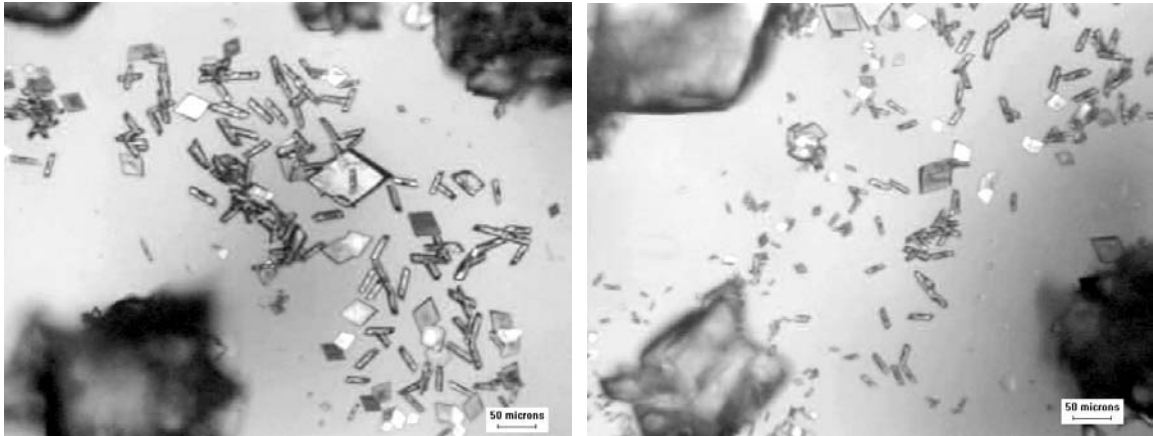


Figure 4-22. Paracetamol crystals obtained from a methanol solution through the LFTC at a 30.4 mL/min flow rate with a cooling temperature of 3 °C, before reaching equilibrium. Notice the presence of both polymorphic forms and the greater size of some Form I crystals at the corners of the pictures. (Image at 10x magnification).

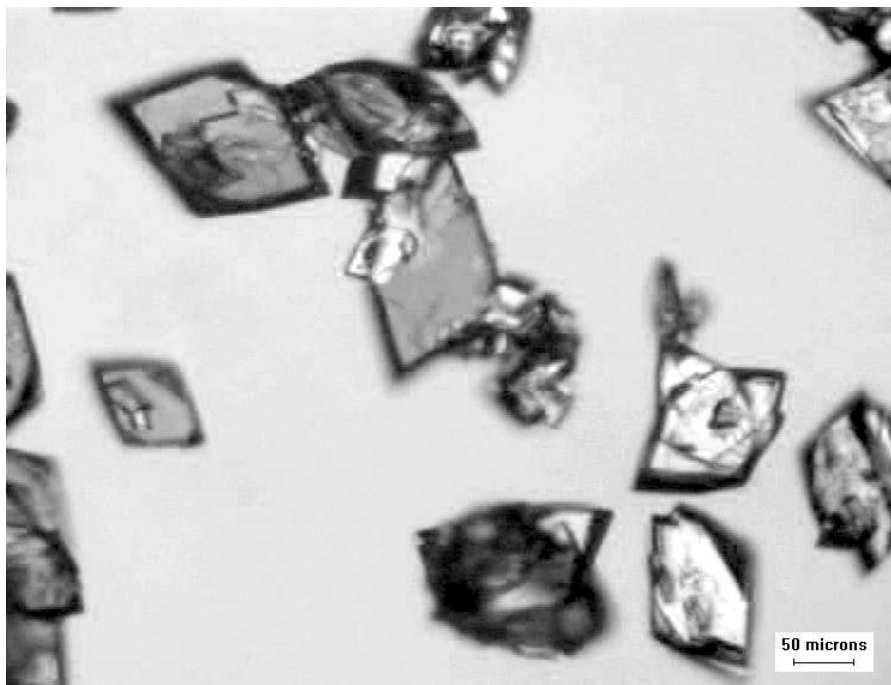


Figure 4-23. Paracetamol crystals obtained from a methanol solution through the LFTC at 30.4 mL/min flow rate with a cooling temperature of 3 °C, 15 minutes after reaching equilibrium. The sample does not necessarily reflect the actual size distribution of the entire batch. (Image at 10x magnification).

It should be pointed out that Nichols and Frampton⁷⁵ were able to obtain Form II from an unseeded batch experiment in an ethanol/methanol (96% / 4% vol.) solvent carried out at -75 °C. In this experiment, crystallization began after 7 days. After 21 days at constant temperature, the researchers were able to identify the crystals as Form II. Conversion to Form I was verified after 43 days. The focus of their research though was on seeded crystallizations, so an optimal temperature for unseeded production of Form II in batch crystallization was not studied by the authors.

The presence of Form II crystals at the 3 °C LFTC experiment, suggest that such an extreme low temperature is not necessary to produce these crystals through the use of a LFTC. An optimal temperature in which only Form II is produced still needs to be researched.

4.4.2 D-mannitol

Experiments were performed at two different concentrations; (1) 50.4 g of D-mannitol dissolved in 200 g of water (25.2 g / 100 g water), for a saturation temperature of 30 °C,⁴ and (2) 82.8 g of D-mannitol dissolved in 175 g of water (47.3 g / 100 g water) with a saturation temperature estimated to be 48.4 °C by van't Hoff interpolation of available data.⁴ Solubility data is shown in Figure 4-24.

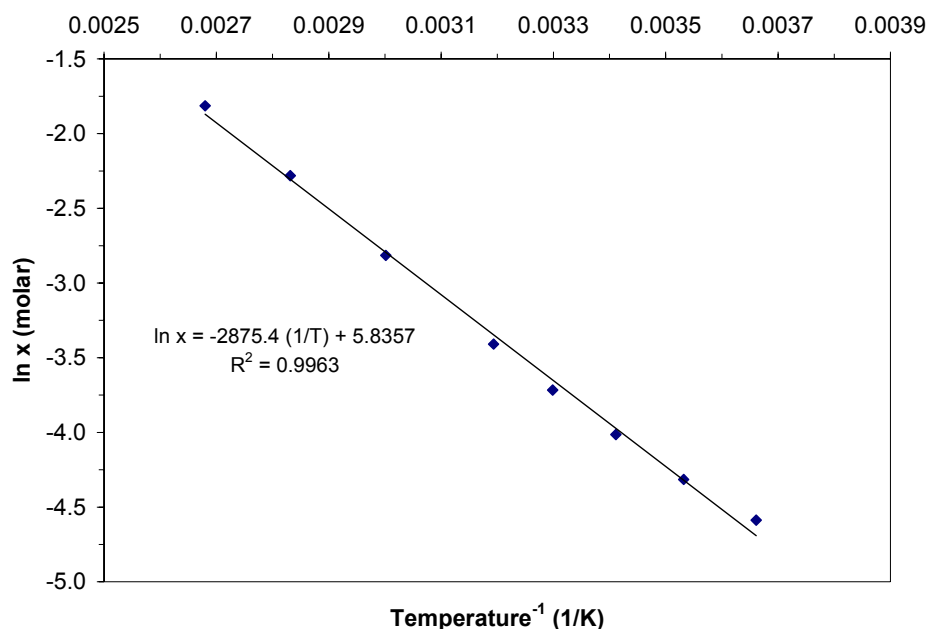


Figure 4-24. Solubility data for D-mannitol in water. Van't Hoff fit is shown with its regression equation for estimation of solubility. (Solubility data from Mullin).⁴

4.4.2.1 Batch Crystallization

Batch experiments with D-mannitol were performed at four different cooling rates, namely 0.15, 0.20, 0.30, and 0.40 °C/min. Initial and final temperatures for these two sets of runs were approximately 39 °C and 11.5 °C for those using a solution at low concentration and approximately 69.5 °C and 11.5 °C for those using solution at high concentration.

For the low concentration batch experiments, regardless of the cooling rate, nucleation occurred well after the final temperature of 11.5 °C ($\sigma = 0.75$) was achieved. Average value of median CLD at equilibrium was $10.31 \pm 0.25 \mu\text{m}$, while the mean was $16.27 \pm 0.07 \mu\text{m}$, regardless of cooling rate. The paracetamol experiments discussed in the previous section showed a decreasing trend in size with higher cooling rates; this was not the case for the D-mannitol experiments where variations in mean and median CLD

at equilibrium were minimal. This can be attributed mainly to the crystallization of D-mannitol as needle-shaped crystals as seen in Figure 4-25.



Figure 4-25. D-mannitol crystals obtained from aqueous solution (47.3 g / 100 g water) through batch cooling crystallization at 0.20 °C/min. The sample does not necessarily reflect the actual size distribution of the entire batch. (Image at 10x magnification).

The formation of crystals proceeded slowly, well after the final temperature was reached. Due to this slow production of crystals, the counts detected by the FBRM experienced fluctuations during the period in which nucleation took place. Consequently, the derivative of the zeroth moment showed significant noise during this time, making it impossible to identify a single peak that could be taken as representative of nucleation rate. Instead, the linear portion of the zeroth moment plot was fitted to a linear equation, whose derivative (i.e. slope) represented the nucleation rate. The estimated nucleation rate values from single runs performed at the specified cooling rates are summarized in

Table 4-4. As shown previously, higher nucleation rates correspond to higher batch cooling rates.

Table 4-4. Nucleation rates for batch crystallization of D-mannitol solutions (25.2 g / 100 g water) at different cooling rates.

Cooling rate (°C/min)	Nucleation rate (m ⁻³ s ⁻¹)
0.15	4.05×10 ⁸
0.30	4.45×10 ⁸
0.40	6.10×10 ⁸

Batch experiments performed with the higher concentration solutions experienced nucleation while being cooled at the specific cooling rates, contrasting with those of lower concentration that crystallized well after the 11.5°C temperature was reached. Figure 4-26 shows the nucleation temperatures at the different cooling rates. Nucleation started at lower temperatures with higher cooling rates, as has been shown also for the case of paracetamol and naproxen sodium in Chapter 3.

Nucleation temperature can also be expressed in terms of the metastable zone width for the particular conditions, as seen in Table 4-5. Higher cooling rates can be translated into wider metastable zones.

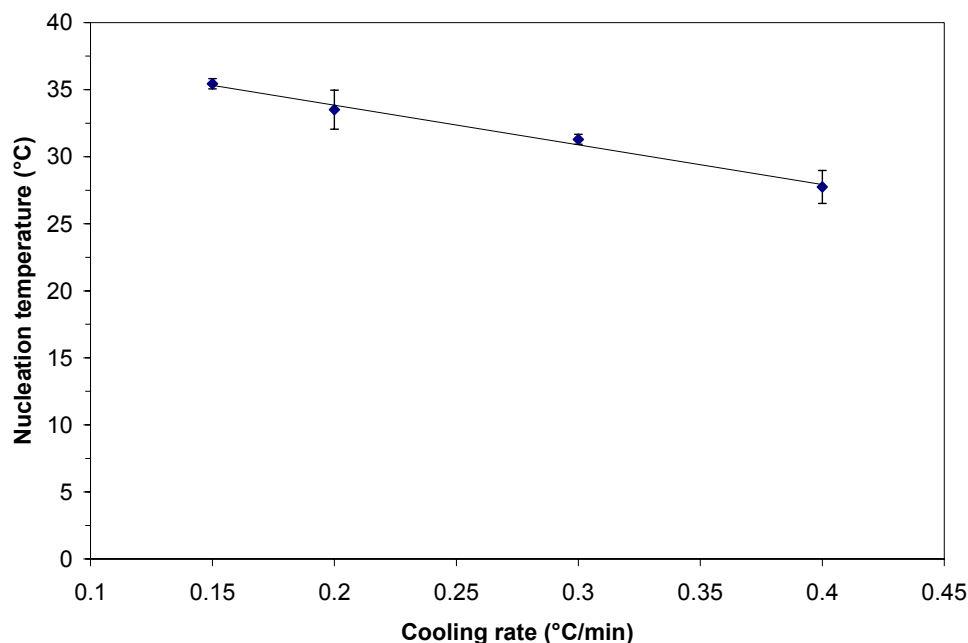


Figure 4-26. Average nucleation temperatures for D-mannitol crystallized from aqueous solutions (47.3 g / 100 g water) in batch operation.

Table 4-5. Average values of nucleation temperature, metastable zone width and relative supersaturation at nucleation according to cooling rate for the cooling batch crystallization of D-mannitol from aqueous solutions (47.3 g / 100 g water).

Cooling rate (°C/min)	Nucleation Temperature (°C)	Metastable Zone Width (°C)	Relative Supersaturation at Nucleation
0.15	35.44	12.92	0.47
0.20	33.51	14.85	0.57
0.30	31.30	17.06	0.68
0.40	27.75	20.61	0.88

Based on nucleation temperature and solubility data, relative supersaturation at nucleation was calculated for the different cooling rates, as shown in Figure 4-27 and Table 4-5. The figure describes the trend that we have already observed; higher nucleation temperatures would reflect into higher equilibrium concentrations, henceforth smaller differences between actual concentration and equilibrium concentrations, rendering smaller values of relative supersaturation. For this reason we see how the

relative supersaturation required for nucleation is directly proportional to the cooling rate. Choosing a linear fit for the data shown in Figure 4-28 shows us that the relative supersaturation required to achieve nucleation at an infinitesimal cooling rate is close to 0.23.

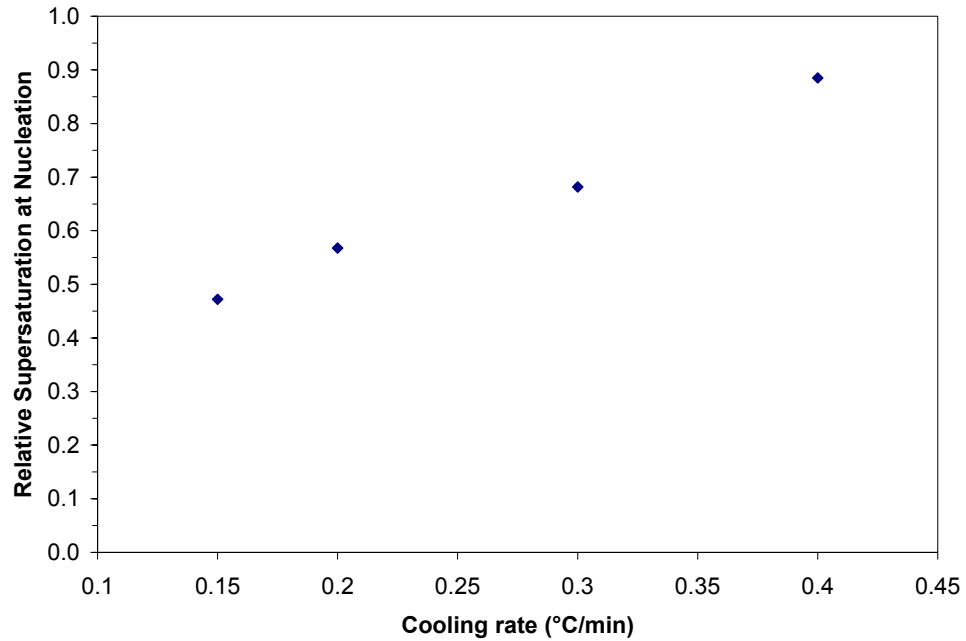


Figure 4-27. Relative supersaturation at nucleation for the crystallization of D-mannitol from aqueous solutions (47.3 g / 100 g water).

Figure 4-28 give us an idea of the relative supersaturation that the solutions experience through time at the different cooling rates. Supersaturation is achieved in less amount of time at higher cooling rates. As with paracetamol, higher cooling rates would promote nucleation earlier (in terms of process duration), albeit at a higher supersaturation, as denoted by the superimposed circles in the graph.

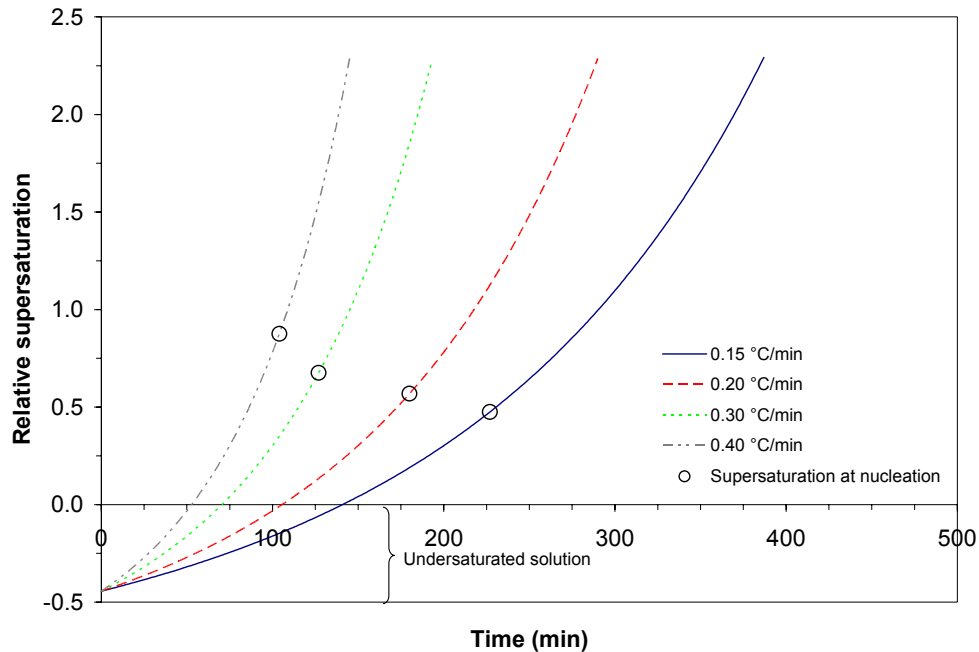


Figure 4-28. Relative supersaturation as a function of time and cooling rate for D-mannitol aqueous solutions (47.3 g / 100 g water).

Figure 4-29 shows the determined nucleation rates for D-mannitol for the high concentration batch experiments. As expected, higher cooling rates promoted higher rates of nucleation. The effect of higher concentrations decreasing the metastable zone width was also reflected on the nucleation rates. The values obtained ranged from 2.09×10^9 to $3.04 \times 10^9 \text{ m}^{-3}\text{s}^{-1}$, almost an order of magnitude higher than the batch experiments at low concentration.

Median and mean values for the CLD suffered from the same effects related to crystal morphology; average values were $8.77 \pm 0.27 \mu\text{m}$ and 15.97 ± 1.10 , respectively, regardless of cooling rate. Due to the morphology of the crystals, a relationship between process parameters and crystal size could not be appropriately drawn.

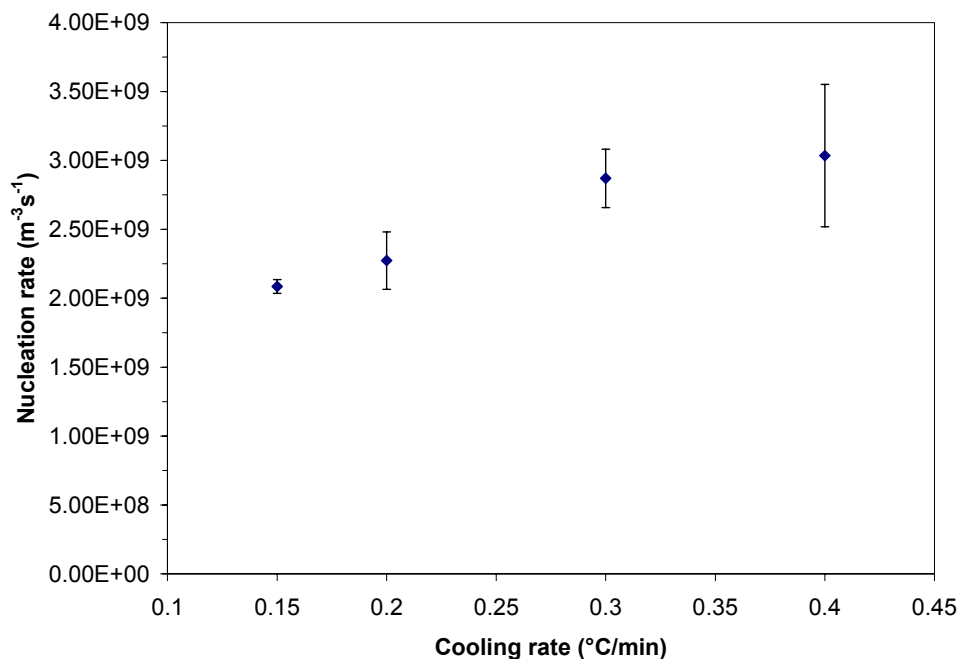


Figure 4-29. Nucleation rates determined by zeroth moment analysis for D-mannitol crystallized from aqueous solutions (47.3 g / 100 g water).

4.4.2.2 Laminar-Flow Tubular Crystallizer System

LFTC experiments were performed with the same amount of materials and at the same concentrations than batch experiments, namely 25.2 g / 100 g water and 47.3 g / 100 g water. Low concentration experiments had a temperature setpoint on the solution vessel of 40 °C, while pumped through the LFTC at a setpoint of 10 °C.^{††} Experiments at the higher concentration had warm solution temperatures of 69.5 °C, and were pumped through the LFTC at temperature setpoints of 10 °C, 20 °C, 30 °C, and 40 °C. Studied volumetric flow rates for all D-mannitol LFTC experiments were 11.9, 28.2 and 45.5 mL/min.

^{††} Throughout this section of the text references will be made about the temperature setpoints in the system. Due to heat interaction with the surroundings, the actual temperatures were slightly different. These can be averaged as follows: for a setpoint of 10°C, the corresponding temperature was 11.5°C; for a setpoint of 20°C, it was 21°C; for 30°C, it remained the same, and for 40°C, it was closer to 39°C. Calculations regarding concentration and supersaturation were performed with the actual temperatures in mind, although reference might be made to the setpoints.

Run times in the low-concentration LFTC experiments with D-mannitol were comparable to those in batch mode; nucleation occurred hours after the solution was transferred into the receiving vessel. The rate of formation of crystals was slow, and the determination of nucleation rates had to be carried out by linear-fit analysis, as was done with the low-concentration batch runs. The nucleation rates were $3.95 \times 10^8 \text{ m}^{-3}\text{s}^{-1}$ for a single run at 11.9 mL/min, $2.88 \times 10^8 \text{ m}^{-3}\text{s}^{-1}$ (average value of three runs) for 28.2 mL/min, and $5.20 \times 10^8 \text{ m}^{-3}\text{s}^{-1}$ for a single run at 45.5 mL/min. Although the nucleation rate varied, it did not do so following any particular trend. This is likely due to the extended period of time (4 to 6.4 hours) that the solution remained in the receiving vessel before nucleation, compared to the time it spent flowing through the LFTC (mean residence time ranging from 20.34 to 76.05 seconds). This prolonged period before the nucleation event is registered by the FBRM is reason to believe that no D-mannitol nuclei formed in the LFTC.

Median and mean values of the CLD were also similar to other experiments, independent of the flow rate, $8.33 \pm 0.40 \text{ }\mu\text{m}$ and $15.00 \pm 1.10 \text{ }\mu\text{m}$, respectively. This similarity in median and mean values with other experiments can be attributed again to the needle morphology of the crystals.

LFTC experiments at the higher concentration focused in studying patterns related to both flow rate and low temperature set point. As with the other cases studied in this chapter, crystallization of D-mannitol in the high concentration LFTC experiments occurred inside the receiving vessel. Crystallization took place in a matter of minutes, with lower temperatures favoring earlier nucleation events. Nucleation started in less than 5 minutes after the solution got transferred into the receiver for the low temperature

setpoint of 10 °C. This increased to about 8 minutes for the 20 °C setpoint, to about 13 minutes for the 30 °C setpoint, and finally to 40 minutes for the 40 °C setpoint. This prolonged time for the 40 °C run again resulted from slow formation of crystals, which is why the nucleation rate was determined by linear-fit analysis for these runs.

Figure 4-30 shows the determined nucleation rates for these runs according to the different temperature set points of the LFTC and receiving vessel jackets. Flow rate, as with the case of paracetamol, did not affect the rate of nucleation. Lower cooling temperatures (and hence higher supersaturations) promoted higher nucleation rates. This relationship is summarized in Table 4-6 in terms of relative supersaturation. A significant difference is observed between the relative supersaturation achieved according to cooling temperature.^{‡‡} Also, most significant is the difference observed in nucleation rate at 40 °C, which was an order of magnitude lower than determined at the lower temperatures.

There was no great change detected in terms of CLD size for the runs with the 10 °C, 20 °C, and 30 °C setpoints, or with change in flow rate. In average, the recorded values of the CLD were $8.24 \pm 0.52 \mu\text{m}$ for the median and $18.66 \pm 3.01 \mu\text{m}$ for the mean.

D-mannitol did not prove to be an appropriate crystalline system to study in terms of CLD due to its needle morphology. Nonetheless, the data acquired gave us more insight about the role of supersaturation, metastable zones and nucleation rates. Nucleation rates for the high concentration solution in the LFTC system ranged from 9.36×10^9 to $1.08 \times 10^{10} \text{ m}^{-3}\text{s}^{-1}$ (with the exception of the 40 °C runs) surpassing those of

^{‡‡} The progression of the relative supersaturation through the LFTC can be seen in Appendix C, where D-mannitol solutions are used as model examples.

batch operation for solutions of the same concentration, reaching the value of 3.04×10^9 $\text{m}^{-3}\text{s}^{-1}$ for 0.40 $^{\circ}\text{C}/\text{min}$ cooling rate.

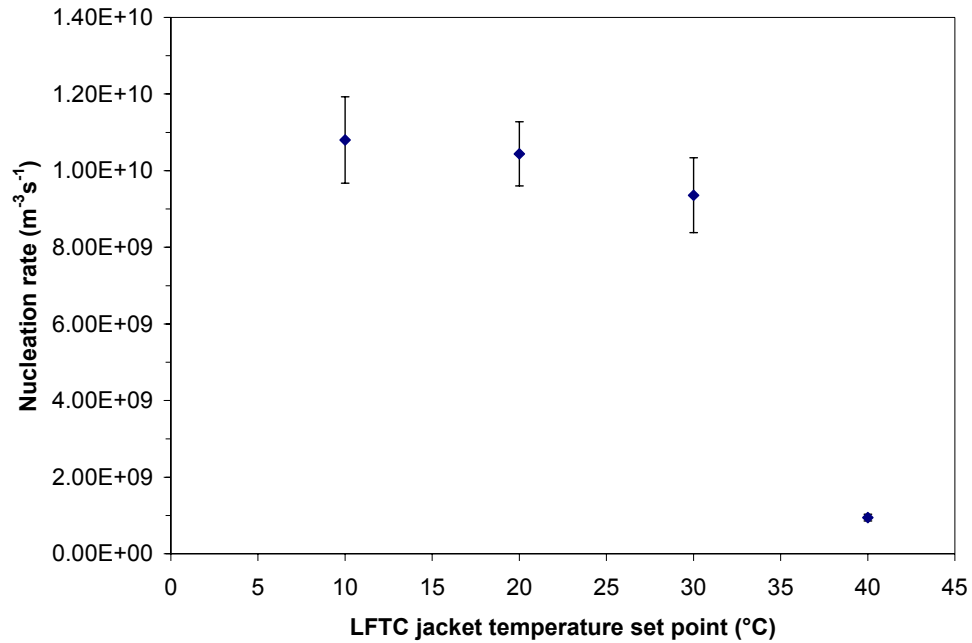


Figure 4-30. Nucleation rates as determined by zeroth moment analysis for crystallization of D-mannitol from aqueous solutions (47.3 g / 100 g water) at different temperatures on the LFTC.

Table 4-6. Approximate relative supersaturation at the outlet of the LFTC and average nucleation rates in the receiving vessel according to average temperatures for D-mannitol solutions (47.3 g / 100 g water).

LFTC Temperature Setpoint ($^{\circ}\text{C}$)	Average Temperature ($^{\circ}\text{C}$)	Relative Supersaturation at Outlet	Nucleation Rate ($\text{m}^{-3}\text{s}^{-1}$)
10	11.5	2.29	1.08×10^{10}
20	21	1.36	1.04×10^{10}
30	30	0.75	9.36×10^9
40	39	0.32	9.45×10^8

Table 4-7 summarizes the time necessary to reach equilibrium of the slurry after nucleation and growth of D-mannitol from the studied 47.3 g / 100 g water solutions. As we emphasized with paracetamol, the time to reach equilibrium is significantly decreased

in LFTC operations than in batch crystallizations. Ultimately this is one of the greatest assets of the LFTC, pending on the desire to obtain crystals of smaller mean size.

Table 4-7. Average time for D-mannitol solutions (47.3 g / 100 g water) to crystallize and reach equilibrium in the slurry. For solutions of 25.2 g / 100 g water, the time to crystallize and reach equilibrium was approximately 8.5 hours, both in batch and LFTC modes.

Batch Crystallization Cooling rate (°C/min)	Time
0.15	6.0 h
0.20	4.7 h
0.30	3.6 h
0.40	2.6 h
LFTC Crystallization Low Temperature Setpoint (°C)	
10	8 min
20	10 min
30	20 min
40	95 min

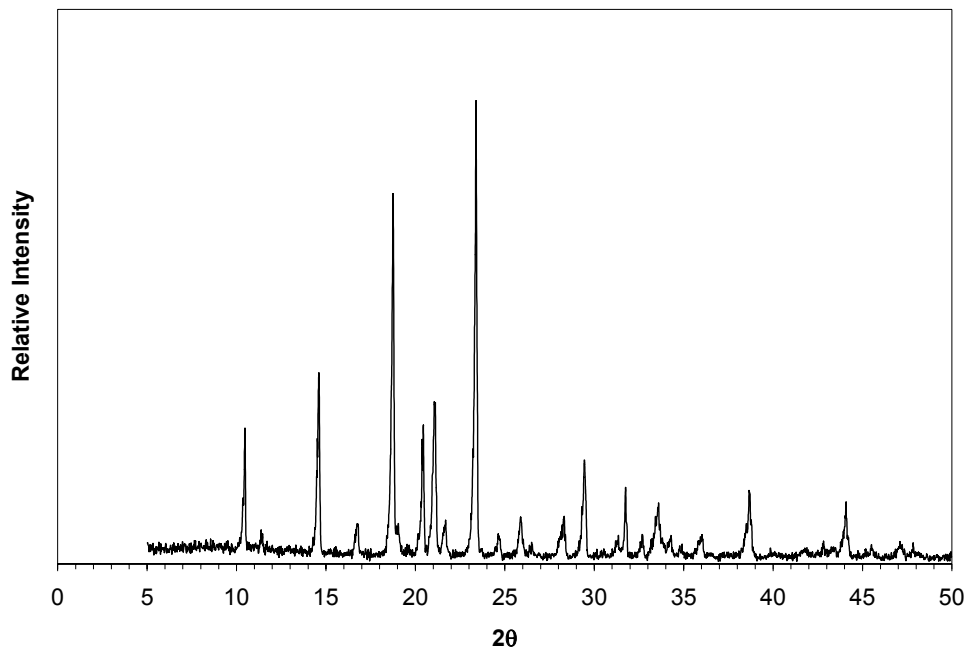


Figure 4-31. PXRD pattern of D-mannitol crystallized from an aqueous solution via LFTC.

Powder XRD spectra of recovered samples showed that the crystallized form obtained was the β polymorph (Fig. 4-31) when compared to published data.^{22, 86, 88} Experiments with other solvents might prove useful in obtaining α and δ forms of D-mannitol, as suggested by the literature.^{22, 86, 88}

4.5 Conclusions

The experiments described in this chapter demonstrated that the LFTC was able to produce crystals with a smaller mean size than could be produced in the corresponding batch cooling crystallization. This conclusion is based on measured chord-length distributions obtained by a focused beam reflectance measurement (FRBM) device positioned to provide such data throughout each experiment. The effect of the two different crystallizer configurations on mean crystal size was especially noticeable when the solute was paracetamol. Precise analyses of the D-mannitol chord-length distributions obtained by the FBRM were made difficult by the needle-like crystal shape produced with this solute.

In addition to comparisons between the two crystallizer configurations, variations with specific process variables within each crystallizer type were also investigated. For example, the mean size of paracetamol crystals produced in batch crystallizations was reduced with increasing cooling rates. Also, higher nucleation rates corresponded to higher supersaturations generated by the LFTC, as seen from D-mannitol experiments.

The batch crystallization system was used to evaluate the metastable limits and the corresponding metastable zones for both paracetamol and D-mannitol. As cooling rates increased, the metastable zone width and nucleation rates increased. The increases in nucleation rates led to reductions in mean crystal size.

The research described in this chapter highlighted two possible advantages of the LFTC, in addition to the production of finer crystals. First, because cooling occurred so rapidly and the resulting crystal mass grew faster because of the greater crystal surface area, the operating time required to go from initial to final conditions could be dramatically reduced. Clearly the higher heat-transfer coefficients associated with forced convection contribute to this advantage. Of course, if large crystals are essential in the product specifications, the advantage of reduced operated time is overwhelmed by the disadvantage of producing smaller crystals.

Second, the data on paracetamol clearly show that it is possible to produce an unstable polymorph because of the exceedingly high rate at which supersaturation is generated. The possibility of extending such behavior to other systems must be evaluated on a case-by-case basis.

APPENDIX A

EXPERIMENTAL SOLUBILITY DATA FOR NAPROXEN SODIUM IN WATER

	Temperature (°C)	Concentration (g anhydrate / kg solution)
Dihydrate	15.2 ± 0.16	104.3
	17.3 ± 0.27	121.5
	20.0 ± 0.11	145.5
	22.9 ± 0.26	181.2
	26.6 ± 0.24	223.7
	27.9 ± 0.13	240.2
	28.3 ± 0.13	246.1
Anhydrate	30.3 ± 0.15	273.7
	34.1 ± 0.23	308.1
	36.9 ± 0.17	333.7
	39.7 ± 0.33	364.1

APPENDIX B

OTHER SYSTEMS STUDIED IN BATCH AND LAMINAR-FLOW TUBULAR CRYSTALLIZERS

The purpose of this appendix is to summarize some of the materials used in experiments that proved to be ineffective for different reasons. In some instances this was due to low FBRM readings attributed to low solids concentration, in others because crystallization occurred inside the laminar-flow tubular crystallizer (LFTC) at a rate that caused clogging of the material inside it. The latter proved to be rather problematic for the unclogging part.

Glycine (98%, Acros Organics)

Most of the experiments with glycine were performed on aqueous solutions with 23.10 g in 100 g of water (saturation temperature of 30 °C) cooled to a 10 °C set point. Crystallization did not occur in the LFTC. Both batch and LFTC experiments experienced low counts in the FBRM (from 15 to 70) which could have been easily affected by background readings. A batch experiment with a concentration of 38.49 g / 100 g water was performed, and although counts reached values up to 210, the data was unreliable due to the multiple peaks in the CLD and the variation of readings in different chord length channels.

L-glutamic acid (99%, Acros Organics)

The low solubility of this material in water, 1.21 g / 100 g water at 30 °C, rendered it inappropriate for CLD characterization via FBRM. The material did not crystallize in the LFTC.

L-serine (Ajinomoto U.S.A., Inc.)

A batch experiment with a concentration of 35.05 g / 100 g water ($T_{\text{sat}} = 50$ °C) was performed having FBRM counts up to 70, clearly influenced by background readings due to multiple peaks detected.

Naproxen sodium (Albermale Corp.)

One experiment was performed on the LFTC with 64.32 g of naproxen sodium dissolved in water ($T_{\text{sat}} = 30$ °C). Temperature was set to 45 °C on the solution vessel, and to 20 °C on the LFTC and receiver vessel. Crystallization did not occur on the LFTC. Another run was then performed with the low temperature set at 10 °C. This promoted the formation of slurry which proceeded to clog the LFTC.

Oxalic acid dihydrate (Certified A.C.S., Fisher Scientific)

Experiments performed with the LFTC with 21.55 g dissolved in 100 mL of water would often clog the crystallizer when cooled from setpoints of 45 °C to 10 °C. For these same concentration and temperature conditions, batch experiments rendered very low FBRM counts (below 30).

Potash alum (Certified A.C.S., Fisher Scientific)

Experiments were performed on the LFTC with 32.80 g of potash alum dissolved in 200 g of water ($T_{\text{sat}} = 30\text{ }^{\circ}\text{C}$) and with 63.04 g dissolved in 175 g of water ($T_{\text{sat}} = 50\text{ }^{\circ}\text{C}$). The first ones had a 45 °C setpoint on the solution vessel and cooled to 20 °C and 10 °C, while the latter ones had a 73 °C setpoint on the solution vessel and cooled to 10 °C, 20 °C, and 40 °C. None of the experiments experienced crystallization on the LFTC. Crystallization occurred in a matter of minutes on the receiving vessel with low counts (less than 65), multiple peaks in the CLD and variation in the different chord length channels.

Sodium sulfate anhydrate (Certified A.C.S., Fisher Scientific)

Sodium sulfate exhibits inverse solubility over temperatures near 40 °C. For this reason, one experiment was performed on the LFTC with saturation temperature conditions of 30 °C, dissolving 71.4 g in 175 g of water. The setpoint on the circulator for the solution vessel was 41°C, and for the LFTC and receiver 10 °C. Crystals were not observed or detected by the FBRM even after two and a half hours in the receiving vessel. When the lower valve of the receiving vessel was open to remove the solution, a gel-like substance was recovered.

Succinic acid (99%, Acros Organics)

An experiment was performed on the LFTC with 49.20 g dissolved in 200 g of water ($T_{\text{sat}} = 50\text{ }^{\circ}\text{C}$). For this experiment the temperature was set to 73 °C for the solution vessel and to 40 °C on the LFTC and receiver. The material crystallized

clogging the LFTC. Experiments at a lower solubility, dissolving 21.21 g in 200 g of water ($T_{\text{sat}} = 30\text{ }^{\circ}\text{C}$) and with temperature setpoints of $45\text{ }^{\circ}\text{C}$ for the solution vessel and cooling to setpoints of either $20\text{ }^{\circ}\text{C}$ or $15\text{ }^{\circ}\text{C}$, also clogged the LFTC upon crystallization.

APPENDIX C

TEMPERATURE AND SUPERSATURATION PROGRESSIONS IN THE LAMINAR-FLOW TUBULAR CRYSTALLIZER

C.1 Introduction

Characterization of the laminar-flow tubular crystallizer (LFTC) involves, among other things, the fundamental knowledge of heat transport. Temperature distribution along the length of the crystallizer is useful to understand contact time of the solution at a specific temperature. Such information proves useful in determining the supersaturation in which a solution is exposed while being transported throughout the crystallizer.

As described in Chapter 4, the LFTC is composed of a 7.62 m long PTFE tube (1.5875 mm ID, 3.175 mm OD) transporting the solution, surrounded by another PTFE tube (11.11 mm ID, 12.70 mm OD) with water on counterflow as the cooling fluid.

Three different models were used to describe the heat transfer characteristics of the system. Fully developed thermal and hydrodynamic flows were assumed where necessary. The entrance regions for these flows were estimated for the studied flow rates, ranging from 10.8 to 47.2 mL/min, and determined negligible when compared to the entire length of the LFTC.

It was not possible to measure all the required properties of the solutions at different temperatures to do this according to the studied systems. For this reason the analyses focus on the use of a specific solvent to characterize heat transfer. Specifically,

water (the solvent in D-mannitol experiments) is used for these models based on actual experimental conditions.

Since crystallization did not occur inside the LFTC in the cases discussed in chapter 4, heat of crystallization was not brought into the analyses. Heat losses or additions from the environment were neglected throughout the LFTC length. For this purpose, the LFTC was covered by two layers of 0.95 cm thick elastomeric foam wrap. Since the solution is transported for a short distance between the solution vessel, the pump and the LFTC, heat losses were experienced. Due to this, the reader will notice in the analyses that the temperature at the inlet of the tube varies from run to run. Generally, a run at a lower flow rate would lose more heat than one at a higher flow rate due to the increase in residence time and longer exposition to ambient conditions at non-isolated sections of the tubing.

Axial conduction was neglected on the basis of high Péclet numbers $Pe = Re Pr$ ($\gtrsim 100$).⁹⁴ The reader will notice that the LFTC is hereon treated as a concentric double-pipe heat exchanger for the sake of the discussion.

C.2 Number of Transfer Units (NTU) method for heat and outlet temperature determination

For this model, a constant wall temperature along the length of the LFTC was assumed. In reality the difference between the inlet and outlet temperatures of the outer tube was rarely over 1 °C. For the purpose of the method, the wall temperature was estimated as the geometrical average of inlet and outlet temperatures of the outer tube. Water properties, namely heat capacity C_p , thermal conductivity k , density ρ and

viscosity μ , were calculated at the inlet temperature of the solution. The Fanning friction factor f for each flow rate was calculated from:

$$f = \frac{16}{\text{Re}_D} \quad (\text{C.1})$$

The Nusselt Nu_D number was assumed at a constant value of 3.66 for the system, based on constant wall temperature and tube flow. From this, the heat transfer coefficient h was calculated from:

$$Nu_D = \frac{hD}{k} \quad (\text{C.2})$$

The overall NTU's were calculated from:

$$NTU = \frac{hA_s}{\dot{m}C_p} = \frac{h\pi DL}{\dot{m}C_p} \quad (\text{C.3})$$

And the efficiency ε of the “heat exchanger” as:

$$\varepsilon = 1 - \exp(-NTU) \quad (\text{C.4})$$

Due to the large surface area of the entire LFTC, the NTU values were relatively high, rendering an efficiency of 1. This means that the total heat lost by the warm solution will be the same as the maximum heat that it is possible for it to lose ($q = q_{max} \varepsilon$). From the heat equation, the heat transferred was calculated:

$$q = \dot{m}C_p \Delta T \quad (\text{C.5})$$

where, for this case ΔT stands for the difference between wall and inlet temperature of the solution. The model, having a perfect efficiency, estimates the outlet temperature of solution to be that of the wall temperature. Notice that since the model assumes a value for the constant wall temperature, the result of the model will be biased accordingly, i.e. the outlet temperature of the solution will be the same as the average wall temperature

specified for the model. Table C-1 summarizes the results for different flow rates and temperatures.

Table C-1. Data and calculated values for heat transfer on the LFTC by NTU method with constant wall temperature. Inlet and outlet temperatures are experimental data values. Notice that the values on the first column are the setpoints of the thermobath circulators, and not the actual measured values.

Temperature setpoints	Flowrates (mL/min)	Crystallizer inlet temperature (°C)	Crystallizer outlet temperature (°C)	Cooling fluid inlet temperature (°C)	Cooling fluid outlet temperature (°C)	Average wall temperture (°C)	Fanning friction factor	Heat exchanged (W)	Expected crystallizer outlet temperature (°C)
73 - 10°C	11.9	59.85	10.93	10.44	10.81	10.63	0.05	40.13	10.63
	28.2	62.64	10.97	10.40	11.39	10.90	0.02	99.81	10.90
	44.5	65.24	13.04	10.50	12.18	11.34	0.01	163.85	11.34
73 - 20°C	11.9	59.56	20.45	20.28	20.61	20.45	0.05	31.89	20.45
	28.2	63.47	20.83	20.37	21.22	20.80	0.02	82.27	20.80
	44.5	64.36	22.10	20.26	21.53	20.90	0.01	132.17	20.90
73 - 30°C	11.9	60.04	30.10	30.18	30.37	30.28	0.05	24.26	30.28
	28.2	62.80	30.27	30.18	30.69	30.44	0.02	62.42	30.44
	44.5	63.38	31.43	30.19	31.08	30.64	0.01	99.63	30.64
73 - 40°C	11.9	59.00	39.68	40.10	40.11	40.11	0.05	15.41	40.11
	28.2	62.96	39.98	40.09	40.39	40.24	0.02	43.82	40.24
	44.5	63.48	40.71	40.13	40.71	40.42	0.01	70.16	40.42

C.3 NTU method for temperature progression along the inner tube with given inlet and outlet temperatures

Since inlet and outlet temperatures of the solution are known from the data acquisition, they can be utilized along the properties of water to look at the progression of temperature along the length of the inner tube, assuming also constant wall temperature.

Using the local number of transfer units NTU_x ,

$$\frac{T_{bulk} - T_{in}}{T_{out} - T_{in}} = 1 - \exp(-NTU_x) = 1 - \exp\left(-\frac{h\pi Dx}{\dot{m}C_p}\right) \quad (C.6)$$

the bulk temperature T_{bulk} can be solved along the length of the LFTC. Notice that the model does not use wall temperature as a parameter. Figure C-1 shows the progression for different flow rates and temperatures.

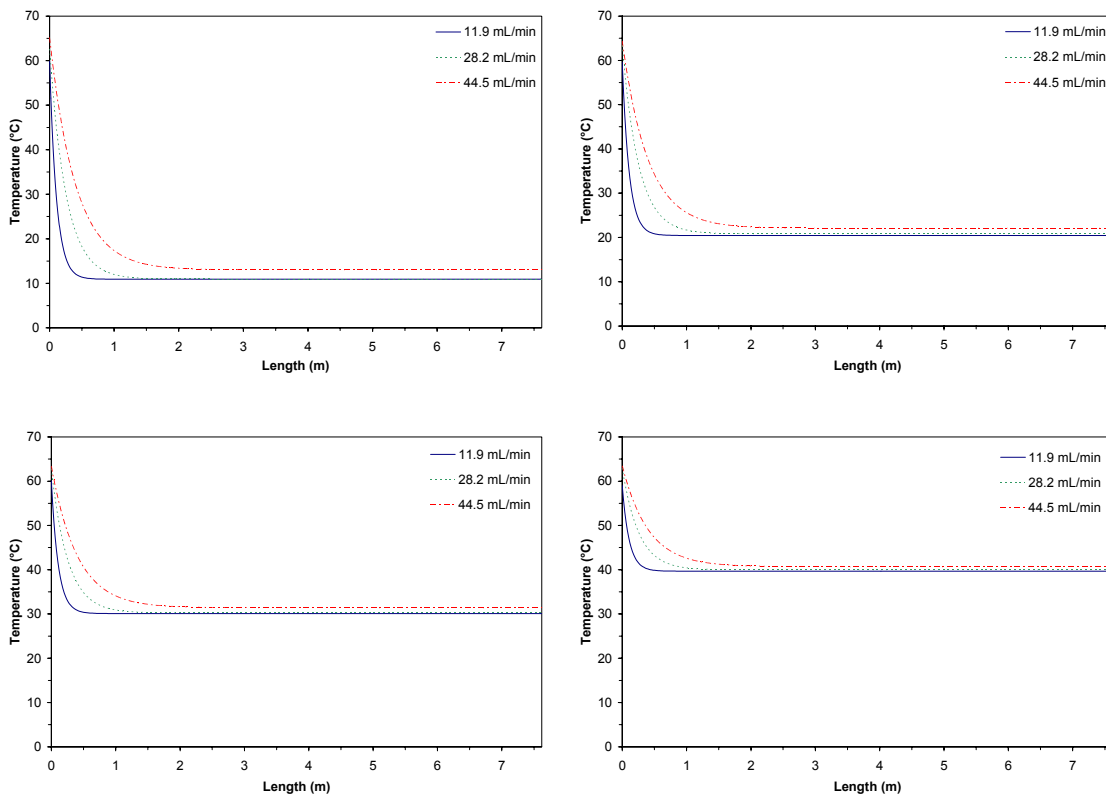


Figure C-1. Temperature progression of the solution along the length of the LFTC assuming constant wall temperature for different temperature setpoints.

C.4 Finite differences analysis for temperature progression

A method based on that explained by Holman⁹⁵ was developed. The method takes small finite elements of the LFTC for analysis based on temperature conditions at one end of the node to then determine the temperatures at the other end. This permits the estimation of the temperature progressions of both inner and outer tube with better accuracy than the previous models. The model also takes advantage of the temperature dependency of the properties of the solvent. The model was built on a parallel flow presumption and then solved for countercurrent conditions on a spreadsheet. The procedure for it is as follows:

1. A characteristic length of 0.02 m was chosen, and therefore a characteristic surface area of $9.97 \times 10^{-5} \text{ m}^2$.
2. The heat transfer coefficients h for both solution and cooling fluid are determined for the characteristic length according to the temperature conditions. In order to do so, we need:
 - a. Inlet temperature of the solution and outlet temperature of the cooling fluid (since it is countercurrent). Outlet temperature of the cooling fluid can be estimated, since it is going to be determined later on.
 - b. Determine the thermal conductivity of water at the given temperature conditions for both the solution and the cooling fluid.
 - c. Assume constant Nusselt number values; 3.66 for the solution inside the tube (since we are assuming constant wall temperature along the selected characteristic length), and 7.11 for the cooling fluid based on the annular ratio D_i/D_o (as estimated from data by Thomas,⁹⁴ where D_i stands for the outer diameter of the inner tube, and D_o is the inner diameter of the outer tube).
 - d. Calculate h for solution (h_i) and cooling fluid (h_o) from equation C.2. An equivalent diameter D_e of 0.03563 m was calculated for the outer tube as suggested by Kern⁹⁶:

$$D_e = 4r_h = 4 \frac{\text{flow area}}{\text{wetter perimeter}} = \frac{4\pi(D_2^2 - D_1^2)}{4\pi D_1} = \frac{D_2^2 - D_1^2}{D_1} \quad (\text{C.7})$$

where r_h is the hydraulic radius, D_1 is the outer diameter of the inner tube, and D_2 is the inner diameter of the outer tube.

3. The thermal conductivity k (in W/m °C) of PTFE (the tube material) is calculated from the geometrical average of the solution and cooling fluid temperatures (in °C) from⁹⁷:

$$k = 0.000486T + 0.253 \quad (\text{C.8})$$

4. With the h and k values, the overall heat transfer coefficient for the solution U_i is calculated as:

$$U_i = \frac{1}{\frac{1}{h_i} + \frac{A_i \ln(r_o / r_i)}{2\pi k L} + \frac{A_i}{A_o h_o}} \quad (\text{C.9})$$

where the subscripts i and o refer to the inside and outside of the inner tube respectively, and A is the cross-sectional area.

5. The incremental heat transfer Δq_j for the specific incremental area ΔA_j can then be calculated as:

$$\Delta q_j = U_{ij} \Delta A_j (T_i - T_o)_j \quad (\text{C.10})$$

6. With the values of mass flow rate \dot{m} and heat capacity C_p evaluated at the known temperatures for both solution and cooling fluid^{§§}, the temperatures of both flows at the other side of the node can be calculated from:

$$\Delta q_j = -(\dot{m}_i C_{p_i})_j (T_{i,j+1} - T_{i,j}) = (\dot{m}_o C_{p_o})_j (T_{o,j} - T_{o,j+1}) \quad (\text{C.11})$$

7. Using the newly acquired temperatures, the process is repeated for the next increment.
8. Finally, when the spreadsheet has been developed for the entire length of the crystallizer, the temperature at the inlet of the outer tube is set, and the

^{§§} Flow rate for the cooling fluid was measured as 1.27 L/min.

spreadsheet is then set to solve the equations for the given conditions in countercurrent flow.

The above procedure will render the temperature progression for both solution and cooling fluid in the crystallizer given the inlet temperature conditions and flow rates. While it is much more accurate than the previous models, there is a certain level of error, due to idealities in the calculations, such as properties of the solution and the assumption that the flow is fully developed both thermally and hydrodynamically during the entire length of the LFTC. The model predicted outlet temperatures for the crystallizer with an average error of 3%, and outlet temperatures for the cooling fluid with an average error of 1.4%. Figures C-2 to C-5 show the temperature progression for solution and cooling fluid for different flow rates and temperatures. In all events, higher flow rates would not permit the solution to reach the inlet temperature of the outer tube cooling fluid.

Using the differential volume of the nodes chosen, each of a length of 0.02 m, an equivalent cooling rate for the solution was calculated for all cases. Table C-2 summarizes the values of these cooling rates for the inlet and outlet regions of the LFTC at different conditions. Notice that for the flow rate of 11.9 mL/min, the cooling rate reaches zero (in reality, the calculations showed values on the order of 10^{-5} and 10^{-6} °C/min) representing that the solution has already reached constant temperature.

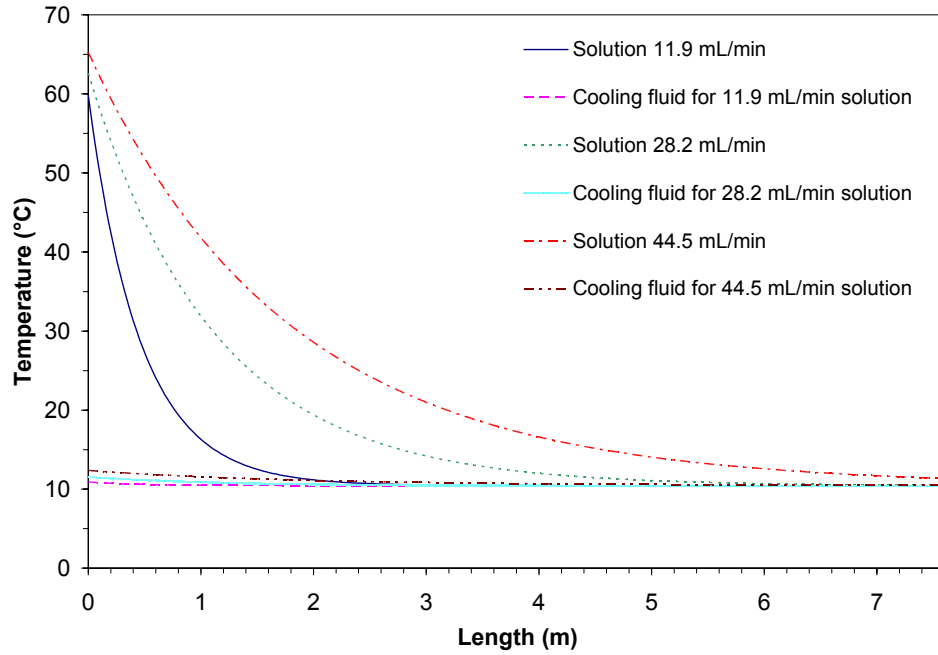


Figure C-2. Temperature progression for solution and cooling fluid in counterflow using finite differences method for 10 °C temperature setpoint.

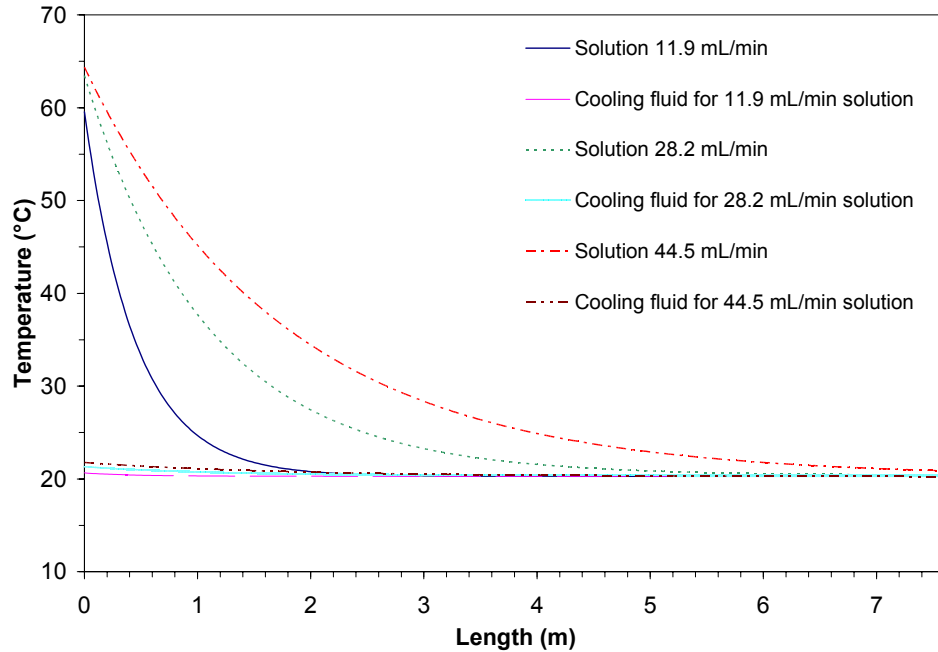


Figure C-3. Temperature progression for solution and cooling fluid in counterflow using finite differences method for 20 °C temperature setpoint.

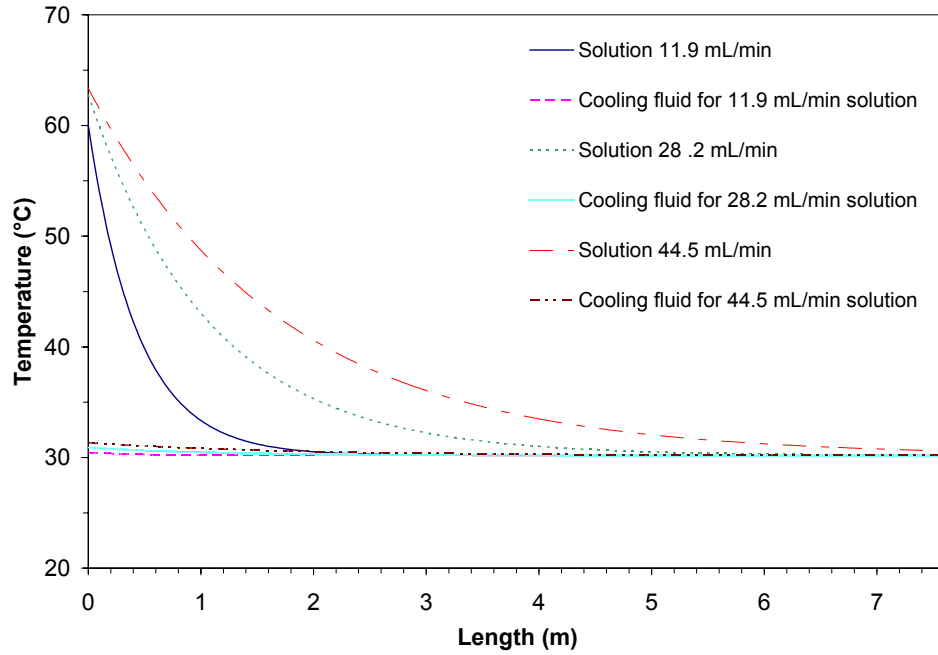


Figure C-4. Temperature progression for solution and cooling fluid in counterflow using finite differences method for 30 °C temperature setpoint.

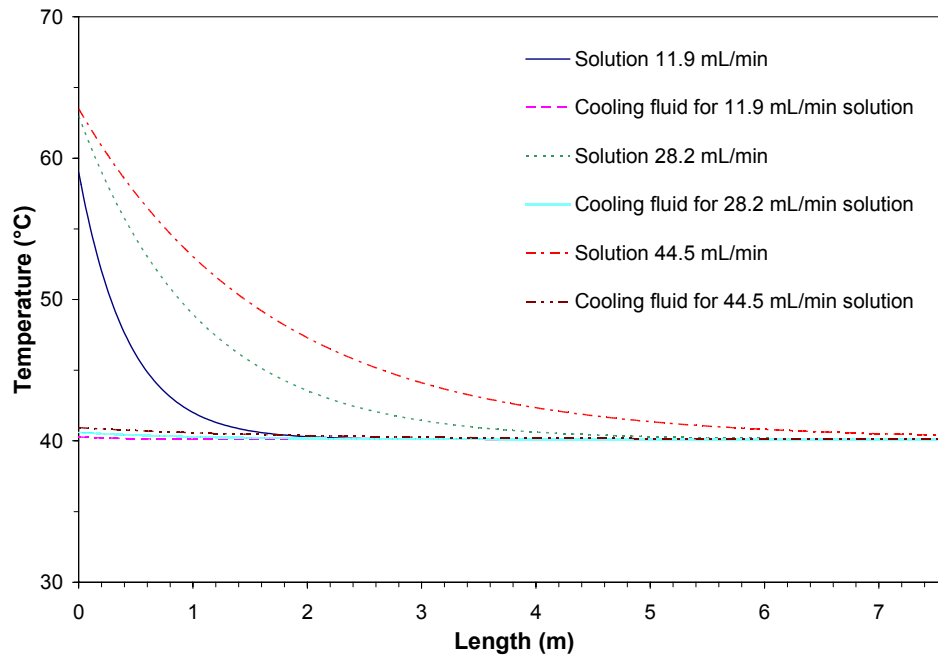


Figure C-5. Temperature progression for solution and cooling fluid in counterflow using finite differences method for 40 °C temperature setpoint.

Table C-2. Equivalent cooling rates for the LFTC on a basis of 0.02 m characteristic lengths.

Temperature setpoints	Flowrates (mL/min)	Initial equivalent cooling rate (°C/min)	Final equivalent cooling rate (°C/min)
73 - 10 °C	11.9	635	0
	28.2	666	0.9
	44.5	691	11
73 - 20 °C	11.9	516	0
	28.2	562	0.6
	44.5	569	8
73 - 30 °C	11.9	400	0
	28.2	433	0.4
	44.5	435	5
73 - 40 °C	11.9	257	0
	28.2	308	0.2
	44.5	311	4

C.5 Overall heat transfer coefficient

Based on the entire length of the LFTC and average temperatures, overall heat transfer coefficients were calculated from equation C.9. Table C-3 summarizes the results.

Table C-3 Overall heat transfer coefficients for the LFTC.

Temperature setpoints	Flowrates (mL/min)	Overall heat transfer coefficient, U (W/m ² °C)
73 - 10 °C	11.9	354
	28.2	354
	44.5	355
73 - 20 °C	11.9	363
	28.2	363
	44.5	364
73 - 30 °C	11.9	371
	28.2	371
	44.5	372
73 - 40 °C	11.9	378
	28.2	378
	44.5	378

C.6 Supersaturation progression in the LFTC

The progression of relative supersaturation throughout the LFTC for a solution can be easily determined once the temperature of the fluid is known. Following the heat transfer model discussed in section C.4, the relative supersaturation of the solution was determined for the entire length of the crystallizer. Figures C-6 through C-9 depict relative supersaturation for D-mannitol aqueous solutions through the LFTC. Lower temperatures allow higher supersaturations. Slower flow rates allow the solution to reach a constant supersaturation at a shorter length than at faster rates. Table C-4 shows the specific distance in which supersaturation is reached. If a specific supersaturation is required for a given process, it is then a matter of determining the flow rate, length or temperature of the LFTC accordingly.

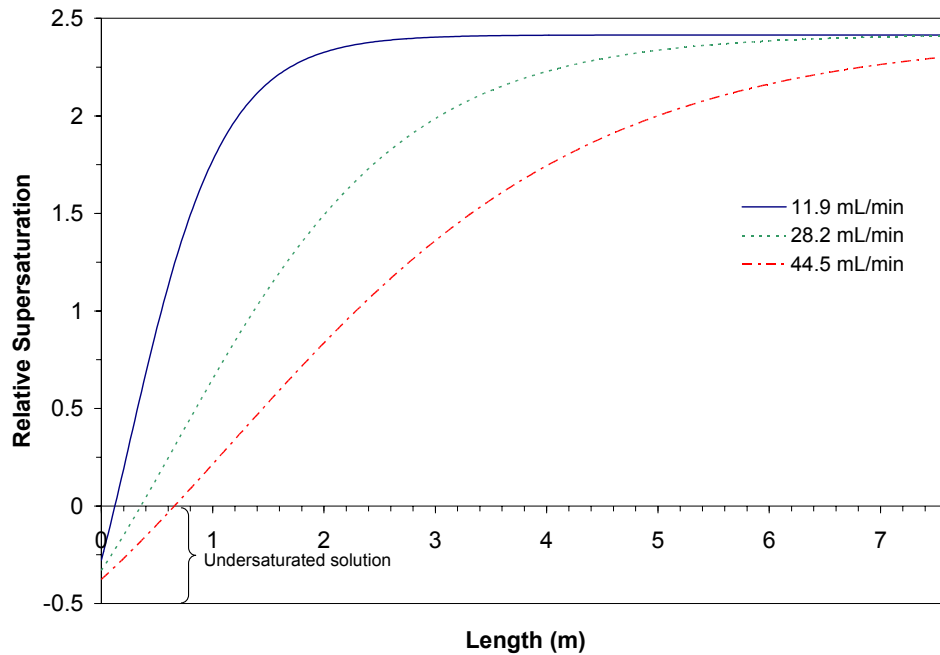


Figure C-6. Relative supersaturation progression for D-mannitol solution in the LFTC for 10 °C setpoint.

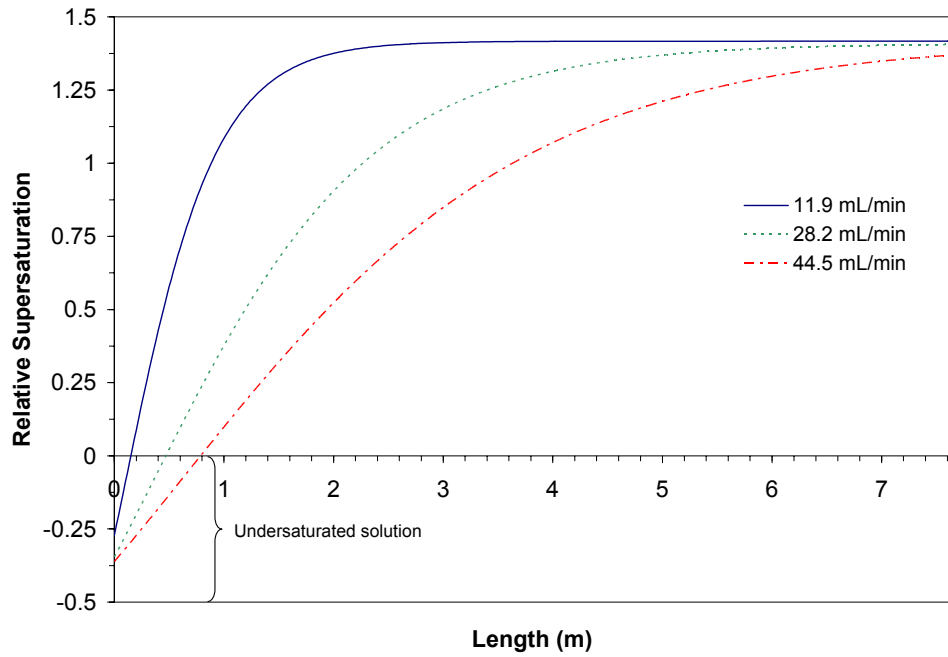


Figure C-7. Relative supersaturation progression for D-mannitol solution in the LFTC for 20 °C setpoint.

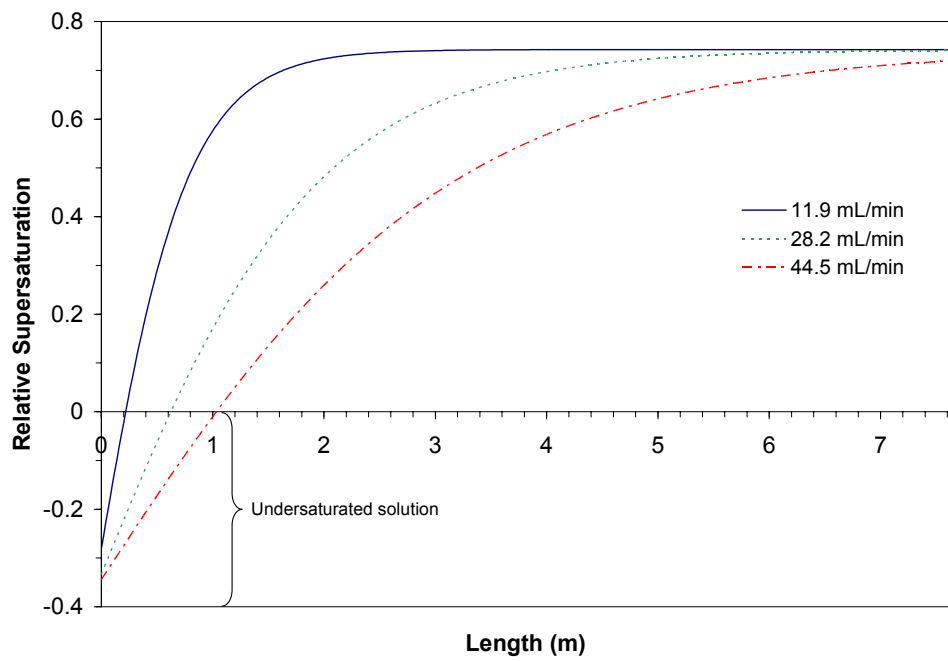


Figure C-8. Relative supersaturation progression for D-mannitol solution in the LFTC for 30 °C setpoint.

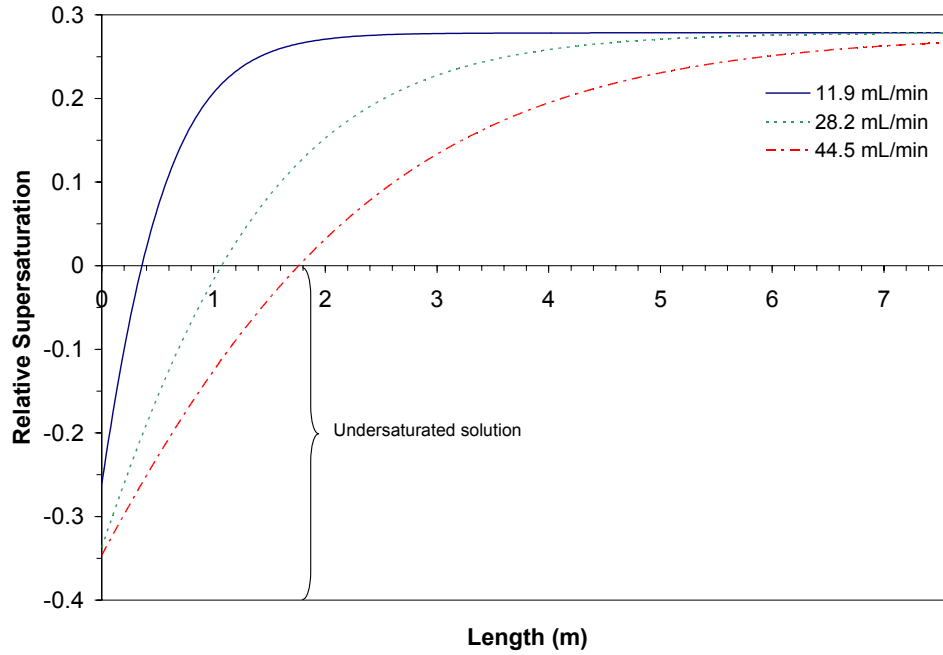


Figure C-9. Relative supersaturation progression for D-mannitol solution in the LFTC for 40 °C setpoint.

Table C-4. Length to reach supersaturation for D-mannitol solutions in the LFTC.

Temperature setpoints	Flowrate (mL/min)	Length (m)
73 °C to 10 °C	11.9	0.14
	28.2	0.36
	44.5	0.65
73 °C to 20 °C	11.9	0.16
	28.2	0.48
	44.5	0.80
73 °C to 30 °C	11.9	0.22
	28.2	0.64
	44.5	1.04
73 °C to 40 °C	11.9	0.36
	28.2	1.08
	44.5	1.78

C.7 Closing remarks

Of the three heat transfer models shown, the finite differences method proves to be the most practical tool for analysis. Indeed, it is worth the effort of developing an accurate spreadsheet to calculate heat transfer parameters. The method though is not flawless. It has been mentioned that water properties were assumed for the development of the model, as well as the assumptions of fully developed thermal and hydrodynamic flows. Calculation of the heat transfer coefficients require great care since their values are directly linked to Nusselt numbers based on correlations. The equivalent diameter chosen for the circular annulus formed by the cooling fluid is also important, as different authors suggest different values, or as it can be easily miscalculated by the person developing the model. The accuracy of the model though is proven when compared to the experimental temperature data. Furthermore, in contrast with the NTU model assuming constant wall temperature, it gives a more realistic progression of temperature, giving the researcher a better idea of the instant in which the solution reaches the desired temperature. Due to the constant wall temperature assumption, the NTU method fails to do this appropriately, by showing how a constant temperature is reached at the early stages of the LFTC, which is inaccurate, especially at higher flow rates.

The finite difference method gives the researcher the advantage of knowing *a priori* an accurate temperature progression, so that the decision of flow rate, crystallizer length, and desired final temperature and supersaturation, can be done relatively easy.

APPENDIX D

TABULATED DATA AND RESULTS FOR THE CRYSTALLIZATION OF PARACETAMOL AND D-MANNITOL IN BATCH AND LAMINAR- FLOW TUBULAR CRYSTALLIZERS

D.1 Paracetamol data

Solution: Paracetamol / Ethanol (34.02 g / 100 g solvent)

Crystallizer: Batch

Experimental values

Cooling rate (°C/min)	Nucleation temperature (°C)	Nucleation rate (m ⁻³ s ⁻¹)	Median (µm)	Mean (µm)
0.15	33.65	9.91E+08	25.34	29.59
0.15	36.51	9.28E+08	25.7	30.14
0.15	36.78	1.07E+09	23.27	28.22
0.15	35.61	9.44E+08	24.17	28.96
0.20	34.44	9.10E+08	24.6	28.76
0.20	35.19	1.07E+09	24.91	29.25
0.30	35.01	1.38E+09	22.42	26.92
0.30	33.10	1.47E+09	22.37	26.78
0.30	26.00	1.28E+09	21.71	25.97
0.40	29.65	1.68E+09	18.53	22.87
0.40	21.89	1.74E+09	18.69	22.99

Average values

Cooling rate (°C/min)	Nucleation temperature (°C)	Standard deviation (°C)	Nucleation rate (m ⁻³ s ⁻¹)	Standard deviation (m ⁻³ s ⁻¹)	Median (µm)	Standard deviation (µm)	Mean (µm)	Standard deviation (µm)
0.15	35.64	1.42	9.83E+08	6.37E+07	24.62	1.11	29.23	0.83
0.20	34.82	0.53	9.90E+08	1.13E+08	24.76	0.22	29.01	0.35
0.30	31.37	4.75	1.38E+09	9.50E+07	22.17	0.40	26.56	0.51
0.40	25.77	5.49	1.71E+09	4.24E+07	18.61	0.11	22.93	0.08

Solution: Paracetamol / Methanol (55.66 g / 100 g solvent)

Crystallizer: Batch

Experimental values

Cooling rate (°C/min)	Nucleation temperature (°C)	Nucleation rate (m ⁻³ s ⁻¹)	Median (µm)	Mean (µm)
0.15	51.41	3.78E+08	22.43	29.35
0.15	51.41	6.46E+08	22.58	29.53
0.30	50.53	8.83E+08	20.42	27.11
0.30	48.36	1.73E+09	20.52	26.3
0.40	37.2	2.19E+09	19.93	25.6
0.40	45.23	1.83E+09	20.26	26.77

Average values

Cooling rate (°C/min)	Nucleation temperature (°C)	Standard deviation (°C)	Nucleation rate (m ⁻³ s ⁻¹)	Standard deviation (m ⁻³ s ⁻¹)	Median (µm)	Standard deviation (µm)	Mean (µm)	Standard deviation (µm)
0.15	51.41	0.00	5.12E+08	1.90E+08	22.51	0.11	29.44	0.13
0.30	49.45	1.53	1.31E+09	5.99E+08	20.47	0.07	26.71	0.57
0.40	41.22	5.68	2.01E+09	2.55E+08	20.10	0.23	26.19	0.83

Solution: Paracetamol / Ethanol (34.02 g / 100 g solvent)

Crystallizer: LFTC

Experimental values

Flow rate (mL/min)	Nucleation rate (m ⁻³ s ⁻¹)	Median (µm)	Mean (µm)
10.8	1.72E+09	15.15	19.47
26.7	1.62E+09	14.61	18.86
26.7	1.61E+09	15.44	19.61
42.9	1.83E+09	14.71	19.00
42.9	1.82E+09	15.17	19.55

Average values

Flow rate (mL/min)	Nucleation rate (m ⁻³ s ⁻¹)	Standard deviation (m ⁻³ s ⁻¹)	Median (µm)	Standard deviation (µm)	Mean (µm)	Standard deviation (µm)
All	1.72E+09	1.05E+08	15.02	0.35	19.30	0.34

Solution: Paracetamol / Methanol (55.66 g / 100 g solvent)

Crystallizer: LFTC

Experimental values

Flow rate (mL/min)	Nucleation rate (m ⁻³ s ⁻¹)	Median (µm)	Mean (µm)
15.6	3.96E+09	15.13	20.70
30.4	3.97E+09	14.30	19.92
47.2	3.80E+09	14.70	20.30

Average values

Flow rate (mL/min)	Nucleation rate ($\text{m}^{-3}\text{s}^{-1}$)	Standard deviation ($\text{m}^{-3}\text{s}^{-1}$)	Median (μm)	Standard deviation (μm)	Mean (μm)	Standard deviation (μm)
All	3.91E+09	9.54E+07	14.71	0.42	20.31	0.39

D.2 D-mannitol data

Solution: D-mannitol / Water (25.2 g / 100 g solvent)

Crystallizer: Batch

Experimental values

Cooling rate ($^{\circ}\text{C}/\text{min}$)	Nucleation temperature ($^{\circ}\text{C}$)	Nucleation rate ($\text{m}^{-3}\text{s}^{-1}$)	Median (μm)	Mean (μm)
0.15	At final temperature, approx. 11.5 $^{\circ}\text{C}$	4.05E+08	10.02	16.26
0.30	At final temperature, approx. 11.5 $^{\circ}\text{C}$	4.45E+08	10.43	16.34
0.40	At final temperature, approx. 11.5 $^{\circ}\text{C}$	6.10E+08	10.47	16.21

Average values

Cooling rate ($^{\circ}\text{C}/\text{min}$)	Median (μm)	Standard deviation (μm)	Mean (μm)	Standard deviation (μm)
All	10.31	0.25	16.27	0.07

Solution: D-mannitol / Water (47.3 g / 100 g solvent)

Crystallizer: Batch

Experimental values

Cooling rate ($^{\circ}\text{C}/\text{min}$)	Nucleation temperature ($^{\circ}\text{C}$)	Nucleation rate ($\text{m}^{-3}\text{s}^{-1}$)	Median (μm)	Mean (μm)
0.15	35.71	2.12E+09	8.82	16.19
0.15	35.17	2.05E+09	8.95	17.14
0.20	33.00	2.50E+09	8.98	16.11
0.20	35.14	2.09E+09	8.77	15.16
0.20	32.38	2.23E+09	9.20	17.45
0.30	31.56	3.02E+09	8.34	17.00
0.30	31.03	2.72E+09	8.56	15.15
0.40	26.88	3.40E+09	8.46	14.19
0.40	28.62	2.67E+09	8.87	15.37

Average values

Cooling rate (°C/min)	Nucleation temperature (°C)	Standard deviation (°C)	Nucleation rate (m ⁻³ s ⁻¹)	Standard deviation (m ⁻³ s ⁻¹)
0.15	35.44	0.38	2.09E+09	4.95E+07
0.20	33.51	1.45	2.27E+09	2.08E+08
0.30	31.30	0.37	2.87E+09	2.12E+08
0.40	27.75	1.23	3.04E+09	5.16E+08

Cooling rate (°C/min)	Median (µm)	Standard deviation (µm)	Mean (µm)	Standard deviation (µm)
All	8.77	0.27	15.97	1.09

Solution: D-mannitol / Water (25.2 g / 100 g solvent)

Crystallizer: LFTC

Experimental values

Flow rate (mL/min)	Nucleation rate (m ⁻³ s ⁻¹)	Median (µm)	Mean (µm)
11.9	3.95E+08	8.21	14.02
28.2	3.19E+08	8.35	15.52
28.2	3.00E+08	8.81	16.55
28.2	2.44E+08	8.55	14.97
45.5	5.20E+08	7.74	13.92

Average values

Flow rate (mL/min)	Nucleation rate (m ⁻³ s ⁻¹)	Standard deviation (m ⁻³ s ⁻¹)
11.9	3.95E+08	
28.2	2.88E+08	3.90E+07
45.5	5.20E+08	

Flow rate (mL/min)	Median (µm)	Standard deviation (µm)	Mean (µm)	Standard deviation (µm)
All	8.33	0.40	15.00	1.10

Solution: D-mannitol / Water (47.3 g / 100 g solvent)

Crystallizer: LFTC

Experimental values (73 °C – 10 °C)

Flow rate (mL/min)	Nucleation rate ($\text{m}^{-3}\text{s}^{-1}$)	Median (μm)	Mean (μm)
11.9	1.21E+10	8.09	21.04
28.2	1.02E+10	8.51	21.87
28.2	1.01E+10	8.00	24.09

Average values (73 °C – 10 °C)

Flow rate (mL/min)	Nucleation rate ($\text{m}^{-3}\text{s}^{-1}$)	Standard deviation ($\text{m}^{-3}\text{s}^{-1}$)	Median (μm)	Standard deviation (μm)	Mean (μm)	Standard deviation (μm)
All	1.08E+10	1.13E+09	8.20	0.27	22.33	1.58

Experimental values (73 °C – 20 °C)

Flow rate (mL/min)	Nucleation rate ($\text{m}^{-3}\text{s}^{-1}$)	Median (μm)	Mean (μm)
11.9	1.10E+10	7.5	18.22
28.2	9.57E+09	8.19	19.77
28.2	1.13E+10	7.92	19.21
45.5	9.89E+09	7.62	18.98

Average values (73 °C – 20 °C)

Flow rate (mL/min)	Nucleation rate ($\text{m}^{-3}\text{s}^{-1}$)	Standard deviation ($\text{m}^{-3}\text{s}^{-1}$)	Median (μm)	Standard deviation (μm)	Mean (μm)	Standard deviation (μm)
All	1.04E+10	8.39E+08	7.81	0.31	19.05	0.64

Experimental values (73 °C – 30 °C)

Flow rate (mL/min)	Nucleation rate ($\text{m}^{-3}\text{s}^{-1}$)	Median (μm)	Mean (μm)
11.9	8.55E+09	8.56	14.31
28.2	8.72E+09	8.98	16.7
28.2	1.07E+10	8.11	14.88
45.5	9.47E+09	9.14	16.18

Average values (73 °C – 30 °C)

Flow rate (mL/min)	Nucleation rate ($\text{m}^{-3}\text{s}^{-1}$)	Standard deviation ($\text{m}^{-3}\text{s}^{-1}$)	Median (μm)	Standard deviation (μm)	Mean (μm)	Standard deviation (μm)
All	9.36E+09	9.79E+08	8.70	0.46	15.52	1.11

Experimental values (73 °C – 40 °C)

Flow rate (mL/min)	Nucleation rate ($\text{m}^{-3}\text{s}^{-1}$)	Median (μm)	Mean (μm)
11.9	9.51E+08	12.49	20.68
28.2	8.23E+08	11.71	19.51
28.2	1.02E+09	10.62	19.37
45.5	9.86E+08	10.97	18.81

Average values (73 °C – 40 °C)

Flow rate (mL/min)	Nucleation rate ($\text{m}^{-3}\text{s}^{-1}$)	Standard deviation ($\text{m}^{-3}\text{s}^{-1}$)	Median (μm)	Standard deviation (μm)	Mean (μm)	Standard deviation (μm)
All	9.45E+08	8.61E+07	11.45	0.83	19.59	0.79

REFERENCES

- (1) Kim, Y.; VanDerveer, D.; Rousseau, R. W.; Wilkinson, A. P., Anhydrous sodium naproxen. *Acta Crystallographica Section E-Structure Reports Online* **2004**, 60, M419-M420.
- (2) Kim, Y.; Rousseau, R. W., Characterization and Solid-State Transformations of the Pseudopolymorphic Forms of Sodium Naproxen. *Crystal Growth & Design* **2004**, 4, (6), 1211-1216.
- (3) Brenek, S.; am Ende, D. J.; Schofield, R.; Jerdonek, C. In *Delivering the desired particle*, Lasentec Users Forum, Charleston, SC, 2002.
- (4) Mullin, J. W., *Crystallization*. 4th ed.; Butterworth-Heinemann: Oxford ; Boston, 2001.
- (5) Nývlt, J.; Söhnel, O.; Matuchová, M.; Broul, M., *The Kinetics of industrial crystallization*. Elsevier Science: Amsterdam ; New York, 1985.
- (6) Kashchiev, D., *Nucleation : basic theory with applications*. Butterworth Heinemann: Oxford ; Boston, 2000.
- (7) Davey, R.; Garside, J., *From molecules to crystallizers*. Oxford University Press: Oxford, 2000.
- (8) Schwartz, A. M.; Myerson, A. S., Solutions and solution properties. In *Handbook of Industrial Crystallization*. Myerson, A. S., Ed. Butterworth-Heinemann: Boston, 2002.
- (9) Beckmann, W., Seeding the desired polymorph: Background, possibilities, limitations, and case studies. *Organic Process Research & Development* **2000**, 4, (5), 372-383.
- (10) Nývlt, J., *Industrial crystallisation from solutions*. Butterworths: London, 1971.
- (11) Fujiwara, M.; Chow, P. S.; Ma, D. L.; Braatz, R. D., Paracetamol crystallization using laser backscattering and ATR-FTIR spectroscopy: Metastability, agglomeration, and control. *Crystal Growth & Design* **2002**, 2, (5), 363-370.
- (12) Liotta, V. In *Automated Metastable Zones*, Lasentec Users Forum, Barcelona, Spain, 2001.
- (13) Barrett, P.; Glennon, B.; O'Sullivan, B. In *Solubility Curve and Metastable Zone Width using Lasentec FBRM & PVM*, Lasentec Users Forum, Charleston, SC, 2002.

- (14) Barrett, P.; Glennon, B., Characterizing the metastable zone width and solubility curve using lasentec FBRM and PVM. *Chemical Engineering Research & Design* **2002**, 80, (A7), 799-805.
- (15) Beckmann, W., Crystallization of pharmaceutical compounds - Polymorphs, pseudo-polymorphs and particle formation. *Engineering Life Science* **2003**, 3, (3), 113-120.
- (16) McCrone, W. C., Polymorphism. In *Physics and chemistry of the organic solid state*. Fox, D., Labes, M.M., Weissberger, A., Eds. Interscience Publishers: New York, 1965.
- (17) Bechtloff, B.; Nordhoff, S.; Ulrich, J., Pseudopolymorphs in industrial use. *Crystal Research and Technology* **2001**, 36, (12), 1315-1328.
- (18) Morris, K. R., Structural aspects of hydrates and solvates. In *Polymorphism in pharmaceutical solids*. Brittain, H. G., Ed. Marcel Dekker, Inc.: New York, 1999.
- (19) Guillory, J. K., Generation of polymorphs, hydrates, solvates, and amorphous solids. In *Polymorphism in pharmaceutical solids*. Brittain, H. G., Eds. Marcel Dekker, Inc.: New York, 1999.
- (20) Boldyreva, E. V.; Drebuschak, V. A.; Drebuschak, T. N.; Paukov, I. E.; Kovalevskaya, Y. A.; Shutova, E. S., Polymorphism of glycine - Thermodynamic aspects. Part I. Relative stability of the polymorphs. *Journal of Thermal Analysis and Calorimetry* **2003**, 73, (2), 409-418.
- (21) Zhang, G. G. Z.; Gu, C. H.; Zell, M. T.; Burkhardt, R. T.; Munson, E. J.; Grant, D. J. W., Crystallization and transitions of sulfamerazine polymorphs. *Journal of Pharmaceutical Sciences* **2002**, 91, (4), 1089-1100.
- (22) Bürger, A.; Henck, J. O.; Hetz, S.; Rollinger, J. M.; Weissnicht, A. A.; Stottner, H., Energy/temperature diagram and compression behavior of the polymorphs of D-mannitol. *Journal of Pharmaceutical Sciences* **2000**, 89, (4), 457-468.
- (23) Doki, N.; Yokota, M.; Kido, K.; Sasaki, S.; Kubota, N., Reliable and selective crystallization of the metastable alpha-form glycine by seeding. *Crystal Growth & Design* **2004**, 4, (1), 103-107.
- (24) Davey, R. J.; Blagden, N.; Potts, G. D.; Docherty, R., Polymorphism in molecular crystals: Stabilization of a metastable form by conformational mimicry. *Journal of the American Chemical Society* **1997**, 119, (7), 1767-1772.
- (25) Garetz, B. A.; Matic, J.; Myerson, A. S., Polarization switching of crystal structure in the nonphotochemical light-induced nucleation of supersaturated aqueous glycine solutions. *Physical Review Letters* **2002**, 89, (17), 175501/1-175501/4.

- (26) Shan, G.; Igarashi, K.; Noda, H.; Ooshima, H., Control of solvent-mediated transformation of crystal polymorphs using a newly developed batch crystallizer (WWDJ-crystallizer). *Chemical Engineering Journal* **2002**, 85, (2-3), 169-176.
- (27) Igarashi, K.; Sasaki, Y.; Azuma, M.; Noda, H.; Ooshima, H., Control of polymorphs on the crystallization of glycine using a WWDJ batch crystallizer. *Engineering Life Science* **2003**, 3, 159-63.
- (28) Brittain, H. G.; Fiese, E. F., Effects of pharmaceutical processing on drug polymorphs and solvates. In *Polymorphism in pharmaceutical solids*. Brittain, H. G., Ed. Marcel Dekker, Inc.: New York, 1999.
- (29) Chemburkar, S. R.; Bauer, J.; Deming, K.; Spiwek, H.; Patel, K.; Morris, J.; Henry, R.; Spanton, S.; Dziki, W.; Porter, W.; Quick, J.; Bauer, P.; Donaubauer, J.; Narayanan, B. A.; Soldani, M.; Riley, D.; McFarland, K., Dealing with the impact of ritonavir polymorphs on the late stages of bulk drug process development. *Organic Process Research & Development* **2000**, 4, (5), 413-417.
- (30) Davey, R. J., Pizzas, polymorphs and pills. *Chemical Communications* **2003**, (13), 1463-1467.
- (31) Bernstein, J., *Polymorphism in molecular crystals*. Oxford University Press: Oxford/Clarendon Press ; New York, 2002.
- (32) Bernstein, J., Crystal-Growth, Polymorphism and Structure-Property Relationships in Organic-Crystals. *Journal of Physics D-Applied Physics* **1993**, 26, (8B), B66-B76.
- (33) Threlfall, T., Crystallisation of polymorphs: Thermodynamic insight into the role of solvent. *Organic Process Research & Development* **2000**, 4, (5), 384-390.
- (34) Blagden, N.; Davey, R. J., Polymorph selection: Challenges for the future? *Crystal Growth & Design* **2003**, 3, (6), 873-885.
- (35) Ostwald, W., Studien über die bildung und umwandlung fester körper. *Zeitschrift für Physikalische Chemie* **1897**, 22, 289-330.
- (36) Greenberg, E. F., FDA wants more 'current' good manufacturing practices. *Packaging Digest* **2002**, 39, (10), 28-29.
- (37) Guidance for industry PAT - A framework for innovative pharmaceutical manufacturing and quality assurance. <http://www.fda.gov/cder/guidance/5815dft.pdf>
- (38) Ruf, A.; Worlitschek, J.; Mazzotti, M., Modeling and experimental analysis of PSD measurements through FBRM. *Particle & Particle Systems Characterization* **2000**, 17, (4), 167-179.

- (39) Abbas, A.; Nobbs, D.; Romagnoli, J. A., Investigation of on-line optical particle characterization in reaction, and cooling crystallization systems. Current state of the art. *Measurement Science & Technology* **2002**, 13, (3), 349-356.
- (40) Wynn, E. J. W., Relationship between particle-size and chord-length distributions in focused beam reflectance measurement: stability of direct inversion and weighting. *Powder Technology* **2003**, 133, (1-3), 125-133.
- (41) Tadayyon, A.; Rohani, S., Determination of particle size distribution by Par-Tec (R) 100: Modeling and experimental results. *Particle & Particle Systems Characterization* **1998**, 15, (3), 127-135.
- (42) Simmons, M. J. H.; Langston, P. A.; Burbidge, A. S., Particle and droplet size analysis from chord distributions. *Powder Technology* **1999**, 102, (1), 75-83.
- (43) Shi, B. Crystallization of solutes that lead to scale formation in black liquor evaporation. Doctoral Thesis, Georgia Institute of Technology, Atlanta, GA, 2002.
- (44) Bennett, R. C., Crystallizer selection and design. In *Handbook of Industrial Crystallization*. Myerson, A. S., Ed. Butterworth-Heinemann: Boston, 2002.
- (45) Tavaré, N. S., *Industrial crystallization : process simulation analysis and design*. Plenum Press: New York, 1995.
- (46) Randolph, A. D.; Larson, M. A., *Theory of particulate processes : analysis and techniques of continuous crystallization*. 2nd ed.; Academic Press: San Diego, 1988.
- (47) Jancic, S. J.; Grootsholten, P. A. M., *Industrial crystallization*. Delft University Press; Reidel Pub. Co.; Delft, Boston, MA, 1984.
- (48) Gros, H.; Kilpio, T.; Nurmi, J., Continuous cooling crystallization from solution. *Powder Technology* **2001**, 121, (1), 106-115.
- (49) Taran, A. L.; Taran, A. V.; Kang, L. C., Gradual Crystallization of Monocomponent Fusions on Cylinder Cooled Surfaces. *Izvestiya Vysshikh Uchebnykh Zavedenii Khimiya I Khimicheskaya Tekhnologiya* **1987**, 30, (12), 130-133.
- (50) Ponomarenko, V. G.; Lisichenko, S. B.; Bei, V. I.; Marchenko, M. A., Crystallization of a Melt on a Cooled Cylindrical Surface. *Journal of Applied Chemistry of the Ussr* **1987**, 60, (8), 1760-1762.
- (51) Gelperin, N. I.; Nosov, G. A.; Sukonkin, V. P., Tube Crystallizer Design. *Khimicheskaya Promyshlennost* **1983**, (1), 53-54.

- (52) Ponomarenko, V. G.; Lisichenko, S. B.; Bei, V. I.; Belomyttsev, S. N., Crystallization in a tubular crystallizer. *Khimicheskoe Mashinostroenie* **1982**, 36, 68-72.
- (53) Saxer, K., A large-scale industrial process for fractional crystallization. *Chemische Produktion* **1980**, 9, (11), 38-9.
- (54) Koeppen, H. G., Thoughts on continuous sugar crystallization. *Zucker* **1976**, 29, (4), 173-8.
- (55) Izukawa, T.; Saeki, T. Crystallization of aromatic polyisocyanates from their isomer mixtures in a short time. JP 2004035429, 2004.
- (56) Belomyttsev, S. N.; Bej, V. I.; Sverdlin, Y. G.; Seballo, V. A.; Zelmanov, G. Z. Method for crystallization of mirabilite. SU 1806815, 1993.
- (57) Bialek, J.; Nowicki, B.; Tecza, W.; Zieborak, K.; Lesniewska, E. Method of purifying naphtalene. PL 163228, 1994.
- (58) Pei, K. Process for producing refined liquid paraffins by cooling, pressure filtration, and aluminum salt. CN 86102601, 1987.
- (59) Korovin, Y. P.; Gertsberg, L. Y.; Krasnov, G. K.; Kos'yanchuk, K. R.; Plotnikova, N. P.; Fomin, V. V.; Goncharova, L. I. Separation of p-nitrotoluene from mixture of nitrotoluene isomers. SU 326175, 1972.
- (60) Gamst, O. N.; Vesje, A. K.; Aarbakke, J., Bioavailability of Naproxen Sodium Suppositories. *International Journal of Clinical Pharmacology and Therapeutics* **1984**, 22, (2), 99-103.
- (61) Runkel, R. A.; Szakacs, J. B.; Segre, E.; Sevelius, H.; Hill, R.; Magoun, R.; Forchiel, E.; Boost, G.; Kraft, K. S., Naproxen Oral Absorption Characteristics. *Chemical & Pharmaceutical Bulletin* **1972**, 20, (7), 1457-66.
- (62) Moyer, S., Pharmacokinetics of Naproxen Sodium. *Cephalalgia* **1986**, 6, 77-80.
- (63) Ravikumar, K.; Rajan, S. S.; Pattabhi, V., Structure of Naproxen, C₁₄H₁₄O₃. *Acta Crystallographica Section C-Crystal Structure Communications* **1985**, 41, (FEB), 280-282.
- (64) Kim, Y. B.; Park, I. Y.; Lah, W. R., The crystal structure of naproxen sodium, (C₁₄H₁₃O₃Na), a nonsteroidal antiinflammatory agent. *Archives of Pharmacal Research* **1990**, 13, (2), 166-73.
- (65) Di Martino, P.; Barthélémy, C.; Palmieri, G. F.; Martelli, S., Physical characterization of naproxen sodium hydrate and anhydrate forms. *European Journal of Pharmaceutical Sciences* **2001**, 14, (4), 293-300.

- (66) Khankari, R. K.; Grant, D. J. W., Pharmaceutical Hydrates. *Thermochimica Acta* **1995**, 248, 61-79.
- (67) Kim, Y., Unpublished data.
- (68) Mullin, J. W.; Garside, J.; Unahabhokha, R., Diffusivities of Ammonium and Potassium Alums in Aqueous Solutions. *Journal of Applied Chemistry of the Ussr* **1965**, 15, (11), 502-5.
- (69) Packer, J. L.; Werner, J. J.; Latch, D. E.; McNeill, K.; Arnold, W. A., Photochemical fate of pharmaceuticals in the environment: Naproxen, diclofenac, clofibrac acid, and ibuprofen. *Aquatic Sciences* **2003**, 65, (4), 342-351.
- (70) Valero, M.; Carrillo, C., Effect of binary and ternary polyethyleneglycol and/or beta-cyclodextrin complexes on the photochemical and photosensitizing properties of Naproxen. *Journal of Photochemistry and Photobiology B: Biology* **2004**, 74, 151-160.
- (71) Grant, D. J. W.; Mehdizadeh, M.; Chow, A. H. L.; Fairbrother, J. E., Non-Linear Van't Hoff Solubility Temperature Plots and Their Pharmaceutical Interpretation. *International Journal of Pharmaceutics* **1984**, 18, (1-2), 25-38.
- (72) Midler, J., M.; Paul, E. L.; Whittington, E. F.; Futran, M.; Liu, P. D.; Hsu, J.; Pan, S.-H. Crystallization method to improve crystal structure and size. 5,314,506, 1994.
- (73) Dauer, R.; Mokrauer, J. E.; McKeel, W. J. Dual Jet Crystallizer Apparatus. 5,578,279, 1996.
- (74) am Ende, D. J.; Crawford, T. C.; Weston, N. P. Reactive Crystallization Method to Improve Particle Size. 6,558,435, 2003.
- (75) Nichols, G.; Frampton, C. S., Physicochemical characterization of the orthorhombic polymorph of paracetamol crystallized from solution. *Journal of Pharmaceutical Sciences* **1998**, 87, (6), 684-693.
- (76) Beyer, T.; Day, G. M.; Price, S. L., The prediction, morphology, and mechanical properties of the polymorphs of paracetamol. *Journal of the American Chemical Society* **2001**, 123, (21), 5086-5094.
- (77) DiMartino, P.; Guyot-Hermann, A. M.; Conflant, P.; Drache, M.; Guyot, J. C., A new pure paracetamol for direct compression: The orthorhombic form. *International Journal of Pharmaceutics* **1996**, 128, (1-2), 1-8.
- (78) Al-Zoubi, N.; Malamataris, S., Effects of initial concentration and seeding procedure on crystallisation of orthorhombic paracetamol from ethanolic solution. *International Journal of Pharmaceutics* **2003**, 260, (1), 123-135.

- (79) Kitamura, M., Controlling factor of polymorphism in crystallization process. *Journal of Crystal Growth* **2002**, 237, 2205-2214.
- (80) Trovao, M. C. N.; Cavaleiro, A. M. V.; de Jesus, J. D. P., Preparation of polymorphic crystalline phases of D-mannitol: influence of keggin heteropolyanions. *Carbohydrate Research* **1998**, 309, (4), 363-366.
- (81) Taylor, G., Dispersion of Soluble Matter in Solvent Flowing Slowly through a Tube. *Proceedings of the Royal Society of London Series a-Mathematical and Physical Sciences* **1953**, 219, (1137), 186-203.
- (82) Ekambara, K.; Joshi, J. B., Axial mixing in laminar pipe flows. *Chemical Engineering Science* **2004**, 59, 3929-3944.
- (83) Fogler, H. S., *Elements of chemical reaction engineering*. 3rd ed.; Prentice Hall PTR: Upper Saddle River, N.J., 1999.
- (84) Al-Zoubi, N.; Kachrimanis, K.; Malamataris, S., Effects of harvesting and cooling on crystallization and transformation of orthorhombic paracetamol in ethanolic solution. *European Journal of Pharmaceutical Sciences* **2002**, 17, (1-2), 13-21.
- (85) Bürger, A., Zur Interpretation von Polymorphie-Untersuchungen. *Acta Pharm. Technol.* **1982**, 28, (1), 1-20.
- (86) Yoshinari, T.; Forbes, R. T.; York, P.; Kawashima, Y., Moisture induced polymorphic transition of mannitol and its morphological transformation. *International Journal of Pharmaceutics* **2002**, 247, (1-2), 69-77.
- (87) Walter-Lévy, L., Cristallochimie-Sur les variétés cristallines du D-mannitol. *C. R. Acad. Sc. Paris Ser. C* **1968**, 267, 1779-1782.
- (88) O'Sullivan, B.; Barrett, P.; Hsiao, G.; Carr, A.; Glennon, B., In situ monitoring of polymorphic transitions. *Organic Process Research & Development* **2003**, 7, (6), 977-982.
- (89) Roberts, S. N. C.; Williams, A. C.; Grimsey, I. M.; Booth, S. W., Quantitative analysis of mannitol polymorphs. FT-Raman spectroscopy. *Journal of Pharmaceutical and Biomedical Analysis* **2002**, 28, (6), 1135-1147.
- (90) Roberts, S. N. C.; Williams, A. C.; Grimsey, I. M.; Booth, S. W., Quantitative analysis of mannitol polymorphs. X-ray powder diffractometry - exploring preferred orientation effects. *Journal of Pharmaceutical and Biomedical Analysis* **2002**, 28, (6), 1149-1159.

- (91) Euhus, D. Nucleation in bulk solutions and crystal growth on heat-transfer surfaces during evaporative crystallization of salts composed of Na₂CO₃ and Na₂SO₄. Doctoral dissertation, Georgia Institute of Technology, Atlanta, 2003.
- (92) Worlitschek, J.; Mazzotti, M., Model-based optimization of particle size distribution in batch-cooling crystallization of paracetamol. *Crystal Growth & Design* **2004**, 4, (5), 891-903.
- (93) Granberg, R. A.; Rasmuson, A. C., Solubility of paracetamol in pure solvents. *Journal of Chemical and Engineering Data* **1999**, 44, (6), 1391-1395.
- (94) Thomas, L. C., *Heat Transfer*. ed.; Prentice-Hall, Inc.: Englewood Cliffs, New Jersey, 1992.
- (95) Holman, J. P., *Heat transfer*. 8th ed.; McGraw-Hill: New York, 1997.
- (96) Kern, D. Q., *Process heat transfer*. 1st ed.; McGraw-Hill: New York, 1950.
- (97) Mark, J. E., *Polymer data handbook*. ed.; Oxford University Press: New York, 1999.